A Study of Bio-Inspired Canopies for the Reduction of Roughness Noise

Ian Andrew Clark

Thesis submitted to the faculty of the Virginia Polytechnic Institute and State University in partial fulfillment of the requirements for the degree of

Master of Science

In

Aerospace Engineering

William J. Devenport, Chair
Eric G. Paterson
W. Nathan Alexander

December 5, 2014

Blacksburg, Virginia

Keywords: Roughness Noise, Bio-Inspired, Noise Reduction, Noise Control, Canopies

A Study of Bio-Inspired Canopies for the Reduction of Roughness Noise

Ian Andrew Clark

ABSTRACT

The wings of most species of owl have been shown to possess three unique physical attributes which allow them to hunt in effective silence: a comb of evenly-spaced bristles along the wing leading-edge; a compliant and porous fringe of feathers at the trailing-edge; and a velvety down material distributed over the upper wing surface. This investigation focuses on the last of the mechanisms as a means to reduce noise from flow over surface roughness. A microscopic study of several owl feathers revealed the structure of the velvety down to be very similar to that of a forest or a field of crops. Analogous surface treatments (suspended canopies) were designed which simulated the most essential geometric features of the velvety down material.

The Virginia Tech Anechoic Wall-Jet Facility was used to perform far-field noise and surface pressure fluctuation measurements in the presence of various combinations of rough surfaces and suspended canopies. All canopies were demonstrated to have a strong influence on the surface pressure spectra, and attenuations of up to 30 dB were observed. In addition, all canopies were shown to have some positive effects on far-field noise, and optimized canopies yielded far-field noise reductions of up to 8 dB across all frequencies at which roughness noise was observed. This development represents a new passive method for roughness noise control with possibility for future optimization and application to engineering structures.

Acknowledgements

I would first like to thank the Office of Naval Research, in particular Dr. Ki-Han Kim, for funding the present work under grant #N00014-13-1-0244.

My biggest thanks has to go to my advisor, Dr. William Devenport, for teaching me almost everything I know about research and for instilling in me a sense of direction and purpose for my work. He has always supported me while simultaneously challenging me to improve. Working with him has given me opportunities I never thought I would have, such as two research-related trips to the University of Cambridge in England. His insight and knowledge have been invaluable to my research, and I owe much of my success to him.

I would also like to extend my appreciation to the other members of my committee, Dr. Eric Paterson and Dr. Nathan Alexander, for their guidance and support throughout my research. Their knowledge and experience have helped me avoid many costly mistakes, and I knew I could always count on their input.

I would like to thank Dr. Justin Jaworski and Dr. Nigel Peake for hosting me at the University of Cambridge and, with Dr. Stewart Glegg, for helping me with the more theoretical aspects of my work. Their input has supplemented my work with a more rigorous discussion regarding the inner workings of my experiments and has given me an understanding far beyond what I would have otherwise gained.

I owe a huge thanks to everyone I've worked with in Lab7 (and later, CREATe) for the past few years. Ever since I started work as an undergraduate researcher, everyone I've met has been generously helpful and supportive, and I would not have been able to complete my project without their help. In particular, I would like to thank Mr. Manuj Awasthi and Mr. Tim Meyers for their help when I was just getting started in the lab, and for always lending a hand when I needed one.

I would like to thank Mr. Nathaniel Ross, Ms. Katelyn Christein, Mr. Daniel Grohol, and Mr. Jeffrey Gomes for their assistance in manufacturing test materials and aiding in measurements.

Finally, I want to thank my parents for being my biggest supporters and for giving me the opportunity to accomplish so much here at Virginia Tech, and I also want to thank my girlfriend Alexandra for supporting me in everything that I do.

Once again, thank you everyone!

-Ian Clark

Table of Contents

Chapter 1 - Introduction 1
1.1 Motivation 1
1.2 Background 1
1.2.1 Roughness Noise 1
1.2.2 The Structure and Function of Owls' Wings 7
1.2.3 Flow over Plant Canopies 9
1.3 Visual Study of Owls' Feathers 10
1.4 Objectives 15
Chapter 2 - Experimental Setup 16
2.1 Experiment Design 16
2.2 Virginia Tech Anechoic Wall Jet Facility 17
2.3 Boundary Layer Measurements 19
2.4 Microphone Instrumentation 27
2.5 Rough Surfaces 34
2.6 Fabric Canopies 37
2.7 Unidirectional Canopies 43
Chapter 3 – Results and Discussion 48
3.1 Validation of Fabric Canopy Mounts 48
3.2 Effect of Roughness on Surface Pressure Fluctuations 49
3.3 Effect of Roughness on Far-Field Sound 52
3.4 Effect of Optimal Fabric Canopy on Surface Pressure Fluctuations 54
3.5 Effect of Optimal Fabric Canopy on Far-Field Sound 57
3.6 Effect of Fabric Geometry on Surface Pressure Fluctuation Attenuation 60
3.7 Effect of Fabric Geometry on Far-Field Noise Spectra 64
3.8 Directionality of Fabric Canopy Far-Field Noise 68
3.9 Validation of Unidirectional Canopy Mounts 70
3.10 Effect of Unidirectional Canopy on Noise and Surface Pressure Fluctuations 73
3.11 Surface Pressure Attenuation – Comparison with Theory 77
3.12 Surface Pressure Attenuation - Scaling 86
Chapter 4 – Conclusions and Future Work 95
References 97

List of Figures

Figure 1.1 Owl feathers (left) examined using an imaging microscope (right). 10
Figure 1.2 Micrometer used to scale images 11
Figure 1.3 Representative image of great gray owl's feather 12
Figure 1.4 Method for imaging the cross-section of the feathers 12
Figure 1.5 Calibrated focal knob on microscope 13
Figure 1.6 Cross-sectional view of snowy owl feather (a) and great gray owl feather (b) 13
Figure 1.7 Base (a), middle (b), and top (c) layers of great gray owl feather. 14
Figure 1.8 Microscopic images of commercial velvet showing straight, bundled fiber in top down view (a) and side view (b) 14
Figure 2.1. Schematic side-view of Virginia Tech Anechoic Wall-Jet Wind Tunnel 17
Figure 2.2. Photographic view of the test-section of the Wall-Jet Tunnel, as viewed from the downstream end of the test plate 18
Figure 2.3. Photographic view of the boundary layer measurement system mounted on the test plate 19
Figure 2.4. Photographic view of the flattened-head Pitot probe in place above the test plate 20
Figure 2.5. Schematic view of the tip of the flattened-head Pitot probe. The darkest area represents the open port. 20
Figure 2.6. Photograph showing the forward extent of the probe in front of the mounting bracket 21
Figure 2.7. All measured boundary layer profiles normalized on maximum velocity and boundary layer thickness (a) or $y1/2$ (b) 21
Figure 2.8. Reference profile obtained at 1257 mm downstream of the nozzle with a jet speed of 60 m/s 22
Figure 2.9. Comparison of measured values of Um to those calculated using the power-law constants above 25
Figure 2.10. Comparison of measured values of $\delta*$ to those calculated using the power-law constants above 25
Figure 2.11. Comparison of measured values of δ to those calculated using the power-law constants above 26
Figure 2.12. Comparison of measured values of θ to those calculated using the power-law constants above 26
Figure 2.13. Comparison of measured values of $y1/2$ to those calculated using the power-law constants above 27
Figure 2.14. Photographic view of the Sennheiser surface pressure microphones featuring attached brass ½ mm pinhole covers 28
Figure 2.15. Photographic view of the microphone calibration setup in the test section of the Wall-Jet Tunnel 28
Figure 2.16. Photographic view of a Sennheiser microphone held in a bushing mounted in the test section of the Wall-Jet Tunnel, as part of the microphone calibration setup 29
Figure 2.17. Amplitude calibration curves featuring the raw data for the three microphones (see legend) along with the smoothed calibration curves (black lines) 30
Figure 2.18. Phase calibration curves featuring the raw data for the three microphones (see legend) along with the smoothed calibration curves (black lines) 31
Figure 2.19. Schematic view of microphone configuration A. 32

Figure 2.20. Photographic view of microphone configuration A with a fabric canopy installed . 32
Figure 2.21. Schematic view of microphone configuration B. 33
Figure 2.22. Photographic view of microphone configuration B with a clean surface 33
Figure 2.23. Photographic view of the rough surface featuring a grid of evenly spaced 3mm hemispheres 35
Figure 2.24. Photographic view of the sandpaper-type rough surface 35
Figure 2.25. Photographic view of the rough surface featuring a grid of evenly spaced 6.4 mm high needles 36
Figure 2.26. Photographic view of the rough surface featuring a grid of evenly spaced 6.4 mm high needles, mounted such that the tops of the needles were at a height equal to that of the surrounding surface 37
Figure 2.27. Scanned images of samples of each fabric canopy along with a scale applicable to all images 37
Figure 2.28. Photographs depicting the modulus testing of fabric 3. The image on the left shows the fabric with only the dowel placed in the fabric loop, while the image on the right shows the fabric after the weights have been attached to the dowel 38
Figure 2.29. Schematic overhead view of the overall test apparatus featuring fabric, support dowels, and taped edges 39
Figure 2.30. Photographic view of the fabric support dowels mounted on the test plate in the Wall-Jet Tunnel 40
Figure 2.31. Schematic side view of the upstream transition ramp and recessed needle bed featuring quarter-round dowels at the edges of the bed 40
Figure 2.32. Photographic view of the taped quarter-round dowels on the upstream (a) and spanwise (b) edges of the recessed needle bed 41
Figure 2.33. Photographic overall view of fabric 2 in place over 3mm hemispherical roughness 41
Figure 2.34. Photographic close-up views of fabric 2, emphasizing the taped fabric edges and tapered dowels 42
Figure 2.35. Profile of the unidirectional fiber support featured in the computer model used to 3D print the structure 43
Figure 2.36. Photographic views of the fiber supports mounted in the Wall-Jet Tunnel 43
Figure 2.37. Photographic views of the unidirectional canopy setup with sandpaper roughness . 44
Figure 2.38. Photographic view of the sandpaper and fiber supports mounted in the Wall-Jet Tunnel without a canopy 44
Figure 2.39. Photographic view of the fiber supports and canopy mounted in the Wall-Jet Tunnel with a smooth surface beneath the canopy 45
Figure 2.40. Photographic close-up view of the spanwise edge of the unidirectional canopy setup, emphasizing the fairing of the edges of the sandpaper with 0.1 mm thick aluminum tape 46
Figure 2.41. Photographic close-up views of each unidirectional canopy (1 (a), 2 (b), and 3 (c)) with surface pressure microphones for reference of scale 47
Figure 3.1 Comparison of far-field noise spectra for smooth wall (solid lines) and smooth wall with fabric mounts (dotted lines) 48
Figure 3.2 Comparison of surface pressure spectra for smooth wall (solid lines) and smooth wall with fabric mounts (dotted lines) 49
Figure 3.3. Comparison of surface pressure spectra for smooth wall (solid lines) and 3mm hemispheres (dotted lines) 50

Figure 3.4. Comparison of surface pressure spectra for smooth wall (solid lines) and sandpaper (dotted lines) 51
Figure 3.5. Comparison of surface pressure spectra for smooth wall (solid lines) and recessed needle bed (dotted lines) 52
Figure 3.6. Comparison of far-field noise spectra for smooth wall (solid lines) and 3mm hemispheres (dotted lines) 53
Figure 3.7. Comparison of far-field noise spectra for smooth wall (solid lines) and sandpaper (dotted lines) 53
Figure 3.8. Comparison of far-field noise spectra for smooth wall (solid lines) and recessed needle bed (dotted lines) 54
Figure 3.9. Comparison of surface pressure spectra for uncovered smooth wall (solid lines) and smooth wall shrouded by fabric 5 (dotted lines) 55
Figure 3.10. Comparison of surface pressure spectra for uncovered 3mm hemispheres (solid lines) and 3mm hemispheres shrouded by fabric 5 (dotted lines) 56
Figure 3.11. Comparison of surface pressure spectra for uncovered sandpaper (solid lines) and sandpaper shrouded by fabric 5 (dotted lines) 56
Figure 3.12. Comparison of surface pressure spectra for uncovered recessed needle bed (solid lines) and recessed needle bed shrouded by fabric 5 (dotted lines) 57
Figure 3.13. Comparison of far-field noise spectra for uncovered smooth wall (solid lines) and smooth wall shrouded by fabric 5 (dotted lines) 58
Figure 3.14. Comparison of far-field noise spectra for uncovered 3mm hemispheres (solid lines) and 3mm hemispheres shrouded by fabric 5 (dotted lines) 59
Figure 3.15. Comparison of far-field noise spectra for uncovered sandpaper (solid lines) and sandpaper shrouded by fabric 5 (dotted lines) 59
Figure 3.16. Comparison of far-field noise spectra for uncovered recessed needle bed (solid lines) and recessed needle bed shrouded by fabric 5 (dotted lines) 60
Figure 3.17. Comparison of surface pressure spectra for uncovered smooth wall (dotted line) and smooth wall covered by fabrics (solid lines) at a jet speed of 60 m/s. 61
Figure 3.18. Comparison of surface pressure spectra for uncovered 3mm hemispheres (dotted line) and 3mm hemispheres covered by fabrics (solid lines) at a jet speed of 60 m/s. 62
Figure 3.19. Comparison of surface pressure spectra for uncovered sandpaper (dotted line) and sandpaper covered by fabrics (solid lines) at a jet speed of 60 m/s. 62
Figure 3.20. Comparison of surface pressure spectra for uncovered recessed needle bed (dotted line) and recessed needle bed covered by fabrics (solid lines) at a jet speed of 60 m/s. 63
Figure 3.21. Comparison of background-subtracted far-field noise spectra for smooth wall covered by fabrics at a jet speed of 60 m/s. 65
Figure 3.22. Comparison of background-subtracted far-field noise spectra for uncovered 3mm hemispheres (dotted line) and 3mm hemispheres covered by fabrics (solid lines) at a jet speed of 60 m/s. 66
Figure 3.23. Comparison of background-subtracted far-field noise spectra for uncovered sandpaper (dotted line) and sandpaper covered by fabrics (solid lines) at a jet speed of 60 m/s. 66
Figure 3.24. Comparison of background-subtracted far-field noise spectra for recessed needle bed (dotted line) and recessed needle bed covered by fabrics (solid lines) at a jet speed of 60 m/s. 67
Figure 3.25. Comparison of background-subtracted far-field noise spectra for sandpaper roughness for microphones at 55° (a), 85.5° (b), 100° (c), and 129° (d) 69

Figure 3.26. Comparison of background-subtracted far-field noise spectra for sandpaper shrouded by fabric 3 for microphones at 55° (a), 85.5° (b), 100° (c), and 129° (d) 69
Figure 3.27. Comparison of far-field noise for smooth wall with transition (solid lines) and transition with thread supports (dotted lines) 70
Figure 3.28. Comparison of surface pressure spectra for smooth wall and transition (solid lines) to transition with thread supports (dotted lines) for surface mics 1 (a), 2 (b), and 3 (c)..... 71
Figure 3.29. Comparison of far-field noise for thread supports (solid lines) and thread supports with sandpaper (dotted lines)..... 72
Figure 3.30. Comparison of surface pressure spectra for thread supports (solid lines) and thread supports with sandpaper (dotted lines) for surface mics 1 (a), 2 (b), and 3 (c)..... 73
Figure 3.31. Comparison of far-field noise spectra for uncovered sandpaper with mounts (solid lines) and sandpaper covered by canopies 1 (a), 2 (b), and 3 (c) (dotted lines)..... 74
Figure 3.32. Comparison of surface pressure spectra for uncovered sandpaper with mounts (solid lines) and sandpaper covered by canopy 1 (dotted lines) measured by surface mics 1 (a), 2 (b), and 3 (c) 75
Figure 3.33. Comparison of surface pressure spectra for uncovered sandpaper with mounts (solid lines) and sandpaper covered by canopy 2 (dotted lines) measured by surface mics 1 (a), 2 (b), and 3 (c) 75
Figure 3.34. Comparison of surface pressure spectra for uncovered sandpaper with mounts (solid lines) and sandpaper covered by canopy 3 (dotted lines) measured by surface mics 1 (a), 2 (b), and 3 (c) 76
Figure 3.35. Comparison of theoretical (solid lines) and experimental (dotted lines) surface pressure spectra obtained for fabric 1 shrouding 3mm hemispheres 79
Figure 3.36. Comparison of theoretical (solid lines) and experimental (dotted lines) surface pressure spectra obtained for fabric 2 shrouding 3mm hemispheres 79
Figure 3.37. Comparison of theoretical (solid lines) and experimental (dotted lines) surface pressure spectra obtained for fabric 3 shrouding 3mm hemispheres 80
Figure 3.38. Comparison of theoretical (solid lines) and experimental (dotted lines) surface pressure spectra obtained for fabric 4 shrouding 3mm hemispheres 80
Figure 3.39. Comparison of theoretical (solid lines) and experimental (dotted lines) surface pressure spectra obtained for fabric 5 shrouding 3mm hemispheres 81
Figure 3.40. Comparison of theoretical (solid lines) and experimental (dotted lines) surface pressure spectra obtained for fabric 1 shrouding sandpaper 83
Figure 3.41. Comparison of theoretical (solid lines) and experimental (dotted lines) surface pressure spectra obtained for fabric 1 shrouding recessed needle bed 83
Figure 3.42. Comparison of theoretical (solid lines) and experimental (dotted lines) surface pressure spectra measured by microphone 2 under unidirectional canopy 1 (a), 2 (b), and 3 (c) shrouding sandpaper 86
Figure 3.43. Unscaled (a) and scaled (b) surface pressure attenuations resulting from canopy 1 shrouding 3mm roughness..... 87
Figure 3.44. Unscaled (a) and scaled (b) surface pressure attenuations resulting from canopy 2 shrouding 3mm roughness..... 87
Figure 3.45. Unscaled (a) and scaled (b) surface pressure attenuations resulting from canopy 3 shrouding 3mm roughness..... 88
Figure 3.46. Unscaled (a) and scaled (b) surface pressure attenuations resulting from canopy 4 shrouding 3mm roughness..... 88

Figure 3.47. Unscaled (a) and scaled (b) surface pressure attenuations resulting from canopy 5 shrouding 3mm roughness 88
Figure 3.48. Unscaled (a) and scaled (b) surface pressure attenuations resulting from canopy 1 shrouding recessed needle bed 89
Figure 3.49. Unscaled (a) and scaled (b) surface pressure attenuations resulting from canopy 2 shrouding recessed needle bed 90
Figure 3.50. Unscaled (a) and scaled (b) surface pressure attenuations resulting from canopy 3 shrouding recessed needle bed 90
Figure 3.51. Unscaled (a) and scaled (b) surface pressure attenuations resulting from canopy 5 shrouding recessed needle bed 90
Figure 3.52. Unscaled (a) and scaled (b) surface pressure attenuation recorded by surface microphone 1 beneath unidirectional canopy 1. 91
Figure 3.53. Unscaled (a) and scaled (b) surface pressure attenuation recorded by surface microphone 2 beneath unidirectional canopy 1. 92
Figure 3.54. Unscaled (a) and scaled (b) surface pressure attenuation recorded by surface microphone 2 beneath unidirectional canopy 2. 92
Figure 3.55. Unscaled (a) and scaled (b) surface pressure attenuation recorded by surface microphone 2 beneath unidirectional canopy 3. 92
Figure 3.56. Unscaled (a) and scaled (b) surface pressure attenuation recorded by surface microphone 3 beneath unidirectional canopy 1. 93
Figure 3.57. Unscaled (a) and scaled (b) surface pressure attenuation recorded by surface microphone 3 beneath unidirectional canopy 2. 93
Figure 3.58. Unscaled (a) and scaled (b) surface pressure attenuation recorded by surface microphone 3 beneath unidirectional canopy 3. 94

List of Tables

Table 1. All boundary layer parameters obtained from the measured profiles 23
Table 2. Power-law constants which characterize the flow parameters in the Wall-Jet Tunnel ... 24
Table 3. Measured and observable characteristics of all fabric canopies 38
Table 4. Physical characteristics of each unidirectional canopy 46
Table 5. Parameters used to generate exponential curve for each fabric covering 3mm hemispheres 78
Table 6. Velocities, break frequencies, and calculated length scales for fabrics 1, 2, 3, and 5 shrouding 3mm hemispheres 82
Table 7. Velocities, break frequencies, and calculated length scales for fabric 4 shrouding 3mm hemispheres 82
Table 8. Parameters used to generate exponential curve for each fabric covering sandpaper 84
Table 9. Parameters used to generate exponential curve for each fabric covering the recessed needle bed 84
Table 10. Velocities, break frequencies, and calculated length scales for fabric 1 shrouding sandpaper 84
Table 11. Velocities, break frequencies, and calculated length scales for fabric 1 shrouding recessed needle bed 84
Table 12. Parameters used to generate exponential curve for each unidirectional canopy shrouding sandpaper 85

Chapter 1 - Introduction

1.1 Motivation

Noise control mechanisms for flow-induced noise have primarily been directed towards the reduction of noise produced at scattering edges, such as the trailing edges of aircraft wings and wind turbine blades. Some of these mechanisms have resulted in significant reduction of noise produced at these edges. As edge noise is reduced, other noise sources become relevant which were previously dominated or drowned out by the edge noise. One of these is noise produced by flow over rough surfaces. In addition to being a significant noise contributor during the use of edge noise control mechanisms, roughness noise dominates for certain structures, namely those with high surface area to perimeter ratios such as submarines and buildings. As few edges exist on these structures, most of the noise produced by flow past these structures can be attributed largely to roughness noise. Surface roughness on these structures may be present in the form of discrete roughness elements, such as rivets, or in the form of distributed, random roughness, such as surface texturing of the building material, barnacles on submarines or ships, bug splatter on aircraft and wind turbines, or general fouling on any of these structures. The effects of this noise range from minor annoyance, in the case of building noise, to compromised strategic effectiveness, in the case of submarines.

As roughness noise becomes more significant in terms of dominant noise sources, noise control mechanisms to reduce this noise become more desirable. Roughness noise control must now be developed and refined just as edge noise control mechanisms are. However, almost no method currently exists to reduce flow noise produced by rough surfaces, other than simply cleaning the roughness off of the surface. At times, cleaning the surface may not be possible, and another method would be beneficial which could eliminate noise from roughness which may form over time on the surface. Inspiration for such a method could come from the owl's wing. The present study will investigate the velvety coating on the upper surface of the owl's wing and its effect on roughness noise, both in the near- and far-field. It is hypothesized that the velvety coating acts to dampen the near-field pressure fluctuations at the surface, thereby reducing the noise scattered into the far-field. Because no studies have been performed relating the owl down to the attenuation of surface pressure fluctuations, the interpretation of results will be related to flows over vegetation canopies contained in the Earth's boundary layer, which have similar structure to the flow of interest, but at a much larger scale.

1.2 Background

1.2.1 Roughness Noise

The characteristics of roughness noise have been the subject of several studies, and must be examined with regard to the different phenomena which interact to produce the noise itself. Until recently, relatively few studies had been undertaken to understand and analyze noise from surface roughness. The relatively low noise levels produced by roughness have dictated that any experiments on surface roughness must be performed using facilities with very low background noise levels. Because of the lack of experimental data, the theory of flow phenomena at the root of roughness noise was slow to develop. Early work was focused on determining the proper

scaling of roughness noise as well as the source type. Work was also done to investigate the contribution of roughness noise in relation to other sources of noise, such as edge noise. Later work involved the investigation of more detailed flow phenomena and their influence on the production of roughness noise. Throughout the literature, the goal is largely to identify a universal relationship between far-field roughness noise and measured flow parameters.

Several early studies forewent the use of wind tunnels entirely, instead utilizing spinning disks or cylinders featuring applied surface roughness. Skudrzyk and Haddle (1960) present an early overview of the theory and experimental principles necessary for the measurements of roughness noise. They relate the velocity fluctuations in the boundary layer (quoted as 4% of the mean flow velocity) to pressure fluctuations through the use of an analog to Bernoulli's equation. They also relate the associated frequencies of the pressure fluctuations to the size of the turbulent eddies which causes the pressure fluctuations. To test the noise produced by surface roughness, they used a spinning cylinder mounted in a water tank and measured the noise produced with two hydrophones with diameters of 2.5 inches and 5 inches. With a thicker boundary layer, the high-frequency noise of the boundary layer itself is less than that for a traditional water or wind tunnel, which enhances the ability to measure roughness-induced noise at higher frequencies. By comparing the noise produced by a smooth, painted cylinder to that produced by a cylinder covered in 60 grit or 180 grit sandpaper, they found that roughness would not produce noise if the grains were contained in the laminar sublayer of the boundary layer. This conclusion was made by extrapolation of their data at higher speeds, at which the roughness elements extended into the logarithmic region, and this extrapolation introduces serious error into their analysis.

Chanaud (1969) measured the noise produced by a spinning disk of 12 inch radius with two types of roughness added to the disk. The first type was a strip of coarse sandpaper attached to the disk's outer edge, while the second type featured rings of sandpaper attached to the surface of the disk. Analysis of the relationship between disk tip velocity and sound pressure level from the disk featuring the roughened ring showed that the sound pressure level scaled with the sixth power of velocity. This scaling is consistent with a dipole source, and this scaling agrees with current theory. However, some significant noise contamination may have been present due to separated flow at the disk edge, which also scales as a dipole source.

To further investigate the scaling of roughness noise, Cole (1980) examined the noise radiated from a flat plate featuring a fully turbulent conventional boundary layer. The surface of the flat plate was treated with a large fetch of 40- and 80- grit sandpaper, and measurements of the radiated noise were made with a parabolic reflector focused at a ¼" microphone. He attempted to normalize the results using both quadrupole and dipole scalings, and found that the radiated noise appeared to have mixed scaling. He postulated that two competing mechanisms, each with different scalings, were the cause of the roughness noise. Cole suggested that a theoretical study could be undertaken to determine the influence of each mechanism, but did not perform the analysis himself.

In an attempt to settle the question of scaling, Hersh (1983) took a different approach to the measurement of roughness noise by utilizing flow through an initially smooth-walled pipe exhausting into a semi-anechoic room and lining the pipe with progressively coarser sandpaper and wire mesh. Because of the high low-frequency background noise levels present in the facility, his conclusions are based on noise in the frequency range between 10 and 40 kHz. His noise measurements showed that the acoustic source of roughness noise is dipole. He was able to correlate the measured sound pressure spectrum with the wall shear stress friction velocity and the equivalent sandpaper roughness. Finally, he was also able to show that the production of

roughness noise becomes more efficient with increasing speed (decreasing boundary layer thickness). His conclusions were made after eliminating possible noise contamination due to flow past the pipe lip and vibration of the pipe itself.

Following the publication of Hersh's study, Howe (1984) developed a theory relating the turbulent pressure fluctuations directly to the propagation of noise to the far-field. He modelled the surface roughness as a series of hemispherical bosses, and expressed the far-field noise in terms of the wavenumber-frequency spectrum of pressure fluctuations on a plane parallel to the wall at a distance from the wall equal to the height of the roughness elements. He assumed that all significant pressure fluctuations would be present above the roughness elements, which limited his formulation to transitional roughness. He found that the intensity of the sound should vary as the sixth power of velocity (concluding that a dipole source is dominant), which was consistent with the findings of Hersh (1983). Howe went further and used his theory to determine the full spectrum of the noise which would be produced by the experimental setup used by Hersh. He found that the characteristics of the spectrum were consistent with the measured spectrum. In his formulation, he neglected viscous effects, which was thought to invalidate the theory when the roughness elements were contained in the viscous sublayer of the boundary layer. However, Howe (1986) showed that the inclusion of viscous effects would increase the predicted acoustic levels by only 2-3 dB across the entire frequency range, thereby showing that the simpler, inviscid formulation was adequate to approximately predict the acoustic characteristics of a given flow over surface roughness. Howe (1988) updated his model to use the smooth wall pressure field given by Chase (1987).

Smol'yakov (2001) also developed a theory relating the properties of the flow and rough surface to the propagation of roughness noise. In particular, he utilizes the combined probability density for the turbulent velocity fluctuations and the random dimensions of the roughness elements. He modeled the dipole source of roughness noise as vortex shedding from the top of each roughness element. However, by using a distribution of roughness heights, the application of this theory to deterministic roughness, such as the hemispherical bosses of Howe, is somewhat inappropriate as it results in a predicted sound spectrum that is tonal, as opposed to broadband.

Because of the implied link between the nature of the surface pressure fluctuations and the resulting far-field noise, it is useful to also review studies which attempt to measure and characterize the pressure spectra at the surface. One early experiment was performed by Blake (1970), who measured the surface pressure fluctuations over smooth and rough surfaces with much greater accuracy than had been previously achieved. The pinhole microphones used by Blake were three times smaller than microphones used in earlier work when normalized on boundary layer displacement thickness. In this way, he was able to resolve and identify the high-frequency components of the surface pressure fluctuations (which result from the smallest-scale eddies) and characterize their influence on the smooth-wall pressure statistics. In addition, Blake tested three different types of rough surface, featuring different roughness heights and spacings. He found that the separation length between the roughness elements influenced the lower frequency fluctuations (large eddies), while the height of the roughness elements influenced the higher frequency fluctuations (small eddies).

Farabee and Geib (1991) produced an extensive study regarding the wall-pressure fluctuations over smooth and rough surfaces. Three rough surfaces were tested in the range of transitionally to fully rough. They used a six microphone wavenumber filter system mounted flush with the wall. Measurements were made at flow velocities from 9.1 to 48.8 m/s. They identified trends for three different regions of the low-wavenumber spectrum of the surface pressure

fluctuations. In the subsonic region, the increases due to surface roughness could be explained by increases in the Reynolds stress at the surface. In the sonic region, the large increases in pressure fluctuations could not be accounted for solely by the increased turbulence due to the surface roughness. Finally, the supersonic region yielded inconclusive results because of the background noise levels of the facility.

Anderson (2007) used the Anechoic Flow Facility at the Naval Surface Warfare Center, Carderock Division to measure noise due to a gravel fetch 32in (streamwise) by 8in (spanwise) at flow speeds ranging from 92-140ft/s. Three different roughness fetches were tested, and care was taken to show that edge noise did not significantly contribute to the sound measurement results. Low-wavenumber surface pressure fluctuation data were collected with a linear array of four flush-mounted microphones downstream of the roughness fetch, while surface pressure spectra were also measured with 1/16in pinhole microphones at two locations, one near the linear array and one in the roughness fetch itself. Far-field sound measurements were taken with a 63-microphone phased array. The study found that increased surface roughness height resulted in elevated levels of the convective and acoustic wavenumber frequency regimes of the surface pressure spectrum. The beamform maps produced by the phased array showed that the dominant noise source as located at the forward part of the roughness fetch where the boundary layer transitioned from smooth to rough surface flow. In this region, the sound scaled as either U^6 or U^7, consistent with dipole or mixed dipole-quadrupole scaling, respectively.

Liu and Dowling (2007) produced a comprehensive study of roughness noise through both theoretical and experimental approaches. Their theory was developed based on Howe's (1984) theory and featured randomly distributed hemispherical bosses on a rigid surface. They formulated an expression for the rough-wall pressure spectrum by comparing several smooth wall pressure spectrums, and by using the assumption of Howe (1984) that the rough wall spectrum differs from the smooth wall spectrum only through an increase in u_τ and δ. They then numerically integrated this formulation to obtain values for the far-field radiated acoustic spectrum. To verify their results experimentally, they performed measurements of far-field noise generated by a roughened plate mounted in the 0.586x0.35m test section of an open-jet wind tunnel. The roughness fetch itself was a square fetch of 0.64m length. The two roughness types were hemispheres with radii of 3mm and 4mm. They used four 1/2in B&K microphones mounted outside of the flow arranged in a square array. They used the array's cross-spectra to eliminate noise due to the flow source, which was significant as the test section was not in an anechoic chamber. Nonetheless, the results were shown to be significantly contaminated by facility noise. The results were presented for flow speeds of 30 m/s, which was the only speed in which the noise due to the roughened plate could be differentiated from that due to a smooth plate. The results showed good agreement with the theoretical predictions in the frequency range of 1-1.7kHz, but showed lower levels than those predicted above 1.8kHz. They present a possible explanation in that the assumptions used to develop the Green function were not valid above 1.8kHz. Finally, they present a numerical assessment of the noise produced by an aircraft (Boeing 757) wing. They found that the noise due to roughness could dominate the trailing edge noise at higher frequencies which depend upon the particular type of roughness considered (from 1-10 kHz for rivets vs. 3-100 kHz for galvanized metal surfaces). They also show that large roughness elements (rivets, joints, etc.) can increase the trailing edge noise by as much as 10-20 dB across the entire frequency range (20Hz-200kHz) by enhancing the friction velocity and boundary layer thickness.

Glegg *et al.* (2007) considered two mechanisms for the generation of roughness noise. First, they reworked the theory of Howe to accommodate a more realistic distribution of roughness

elements. They also eliminated many of the empirical constants used by Howe by using the Corcos (1964) model for the turbulent boundary layer. The second mechanism investigated by Glegg *et al.* (2007) was based on the assumption that each individual roughness element produced an unsteady drag force in the form of vortex shedding, closely related to the drag produced by bluff bodies. In this way, each roughness element would radiate sound as a dipole source aligned with the surface. They also found that the appropriate frequency scaling was based on the correlation lengthscale of the roughness elements, and not on the height of the roughness elements as assumed by Howe (1984).

In preparation for further studies using a new facility, Grissom *et al.* (2006) present a concise explanation of the convection of turbulent eddies within a boundary layer flow. Within the pressure wavenumber-frequency spectrum, there exists a convective ridge which is the primary contributor to the surface pressure spectra measured at a point. The convective velocity within a flow is considered to be between 55% and 85% of the free-stream velocity (Blake, 1986). Turbulent eddies travel with the flow at this convective velocity (U_c), and these eddies are described by some angular frequency ω. The convective ridge mentioned above is described by the convective wavenumber $k_1 = \omega/U_c$. At this point in the spectrum, the pressure fluctuations are thought to be between 1000 and 10 million times as intense as in the rest of the spectrum, so a single-point measurement, say by a pinhole microphone mounted flush with the surface, will be dominated by the influence of this convective ridge.

Grissom *et al.* (2007) present the first aerodynamic and acoustic results obtained in the Virginia Tech Anechoic Wall-Jet Tunnel, which is used in the present study and described in detail in Section 2.2. The facility was designed specifically to measure roughness noise and features a wide jet exhausting over a flat plate, which leads to boundary layer flow topped by a mixing layer. Boundary layer profiles were measured using a flattened-head pitot probe and show that the profiles at each streamwise location collapse when normalized on U_m (max velocity) and $y_{1/2}$, defined as the vertical distance to the location in the mixing layer where the velocity has decayed to half the maximum velocity. Grissom *et al.* (2007) mounted roughness fetches featuring ten different sizes of sandpaper-type roughness to the wall-jet plate, and obtained both aerodynamic (hot-wire anemometry) and acoustic measurements. The roughness fetches featured grain sizes ranging from hydrodynamically smooth to transitionally rough. They were able to conclusively show evidence of scattering as a source mechanism by obtaining clearly measureable noise levels from hydrodynamically smooth roughness. All measured spectra collapsed well with outer variable scaling. Their measured spectra indicated that low frequency noise was primarily caused by a scattering, dipole type source mechanism, while the high frequency noise was controlled by the increased turbulence in the boundary layer due to the surface roughness.

Devenport *et al.* (2011) considered the roughness cases of Grissom *et al.* (2007) and performed parallel measurements of both the surface pressure fluctuations and the associated far-field sound. Their hypothesis was that the scattered far-field noise spectrum would be directly related to the change in the surface pressure spectrum due to the addition of surface roughness. Indeed, they found that the ratio of the measured far-field spectra to the measured surface pressure spectra collapsed well when normalized on the square of the root-mean-square of the roughness height, with the resulting line having a slope of approximately ω^2.

Whereas the preceding papers have sought to characterize, scale, and predict the noise characteristics of particular types of roughness, Glegg and Devenport (2009) present a new "Unified Theory of Roughness Noise" which encompasses all types of rough surfaces by accounting for the specific geometry of the surface itself. In particular, they start with Lighthill's

equation reformulated by Goldstein (1976) and simplified for flow past a rigid surface in which quadrupole sources can be ignored, an assumption which is valid for low Mach number flows, such as low speed or underwater flows. After applying a Green's function for the non-penetration boundary condition at the wall, and assuming that the surface pressure field is homogenous, the radiated far-field sound can be shown to be the convolution integral of the wavenumber transform of the surface slope and surface pressure wavenumber-frequency spectrum. To further simplify the calculations for moderate rough surfaces, the smooth wall wavenumber-frequency spectrum can be used as an approximation for the true rough-wall surface pressure spectrum. Additionally, they propose a method for using far-field measurements to determine the wavenumber-frequency spectrum of the surface pressure fluctuations through the use of a "wavy-wall" with sinusoidal components, which would simplify the surface slope wavenumber transform.

The convolution integral of Glegg and Devenport (2009) is given as:

$$(\rho'(\boldsymbol{x},\omega)c_\infty^2)_{dipole} \approx \frac{-ik_o e^{ik_o|\boldsymbol{x}|}}{2\pi|\boldsymbol{x}|}\int_\kappa p_s(\kappa_1,\kappa_3,\omega)\left\{\left(\frac{x_1\zeta^{(1)}}{|\boldsymbol{x}|}+\frac{x_3\zeta^{(3)}}{|\boldsymbol{x}|}\right)-ik_o h\zeta^{(2)}\right\}(2\pi)^2 d\kappa_1 d\kappa_3 \quad (1.1)$$

Here, the left hand side of the equation represents the pressure fluctuations due to the dipole source, x is the observer position, ω is angular frequency, c_∞ is the free-stream speed of sound, k_o is the acoustic wavenumber, p_s is the surface pressure wavenumber-frequency spectrum, and κ_1 and κ_3 are wavenumber components in the y_1 (streamwise) and y_3 (spanwise) directions, respectively. $\zeta^{(1)}$ and $\zeta^{(3)}$ are the wavenumber transforms of the rough surface slope, given as,

$$\zeta^{(j)}(k_1,k_3)=\frac{1}{(2\pi)^2}\int_\Sigma \frac{\partial\xi}{\partial y_j}\exp\big(i(k_1y_1+ik_3y_3)\big)\,d\Sigma, \quad j=1,3 \quad (1.2)$$

$\zeta^{(2)}$ is the wavenumber transform of the surface height, given as,

$$\zeta^{(2)}(k_1,k_3)=\frac{1}{(2\pi)^2 h}\int_\Sigma \xi\exp\big(i(k_1y_1+ik_3y_3)\big)\,d\Sigma \quad (1.3)$$

In these equations, h is the r.m.s. roughness height, ξ is the rough surface height in the y_2 direction, and Σ is the area of the rough surface projected onto the $y_1y_3$plane.

Devenport *et al.* (2010) presented the results of the experiment proposed by Glegg and Devenport (2009) to test their Unified Theory of Roughness Noise, and to determine the surface pressure wavenumber-frequency spectrum through far-field measurements. The experiment featured a novel type of rough surface: a lenticular lens featuring elliptical ridges which would be largely contained within the viscous sublayer of the flow in the Virginia Tech Wall-Jet Tunnel. The experiment intended to exploit the characteristic of Glegg and Devenport's theory that the wall-pressure wavenumber frequency spectrum could be effectively measured in the far-field if the surface geometry was deterministic and possessed a simple slope-wavenumber spectrum. Indeed, the lenticular lens fit this requirement, and by measuring the radiated far-field noise at several observer locations, and with the lens rotated at several angles relative to the flow, Devenport *et al.* were able to obtain high-resolution results for the wall pressure wavenumber frequency spectrum which, if determined conventionally by pairs of pressure transducers mounted in the wall, would have required a transducer spacing of no more than 0.63 mm. Their results

qualitatively resembled the models given by Corcos and Chase, with closer agreement to Chase's model.

Alexander *et al.* (2012) used the Unified Theory of Glegg and Devenport (2009) to perform direct predictions of the absolute levels of roughness noise produced by 40 grit sandpaper-type roughness and a fetch of randomly distribute hemispheres of 1mm radius. They then compared these predictions to measurements performed in the Virginia Tech Wall-Jet facility. They found the predictions to be highly accurate and relatively insensitive to the exact form of the surface pressure wavenumber-frequency spectrum.

Considering the contributions from all of the papers described above, a concise summary of the nature of roughness noise can be assembled. Noise is produced by flow over roughness through the interaction of pressure fluctuations present in the turbulent boundary layer with the uneven surface. Turbulence is comprised of eddies which are convected with the flow, and these eddies are the source of the pressure fluctuations in the flow. The eddies' characteristic lengths can be as large as the characteristic length scale of the flow itself (for example, the boundary layer thickness) and smaller eddies are inevitably produced through an energy cascade mechanism. The size of these eddies (L), along with their convection velocity (U_c), directly correlate to the frequency (f) of the pressure fluctuations in the flow through the following formula:

$$f = \frac{U_c}{2L} \tag{1.4}$$

The individual roughness elements scatter the unsteady pressure field present in the flow into the far-field. Directly associated with this scattering is the unsteady drag felt by the individual roughness elements, which will have the same frequency spectrum as the associated pressure field in the flow. This unsteady drag can lead to structural vibration of the underlying surface itself, which can drastically boost the efficiency of the surface as a noise producer. These surface pressure fluctuations, therefore, are a direct cause of large portion of noise produced by flow past ships and submarines. The Unified Theory of Glegg and Devenport (2009) and its validation by subsequent studies is key to the current investigation, as it supports the theory that the radiated far-field noise due to roughness can be directly influenced by changing the surface pressure spectrum. As stated above, inspiration for the suppression of the near-field pressure fluctuations comes from the structure of owls' wings, in particular from the velvety down material which covers the top surface of owls' feathers.

1.2.2 The Structure and Function of Owls' Wings

It has long been known that many species of owl are able to hunt in effective silence. A concise description of the noise and aural characteristics of the owl is given by Lilley (1998). He explains that owls have outstanding hearing in the range of 3-6 kHz, which encompasses the frequencies of noise generated by the squeaks of mice and other prey, as well as the rustling of leaves. The upper limit of the owl's hearing is above 20 kHz. Their prey however, have exceptional hearing throughout the frequency range between 2-20 kHz, presumably to help them detect the approach of predators in time to escape. While hawks or similar birds of prey have adapted to this by utilizing high speed flight to capture prey, owls have evolved such that they are able to fly silently at all frequencies above 2 kHz.

Some of the earliest work done to investigate this phenomena was performed by Graham (1934), who identified three unique features of owls' wings which he believed silenced the owls

in flight: a comb of evenly-spaced bristles along the wing leading edge, a compliant and porous fringe of feathers at the trailing edge, and a velvety down material distributed over the upper wing surface. He observed that other species of birds feature barbs or hooks on the top surface of the wing which interlock the feathers during the down-stroke of flapping flight, but release the feathers during the up-stroke in order to allow airflow through the wing. This action creates a rustling noise when the feathers rub together. The owl's wings, with their velvety down material, feature much longer hairs and barbs, which Graham (1934) hypothesized would muffle any rustling noise associated with the rubbing of feathers. He also supposed that the velvety down on the anterior surface of the wing, which was not involved in interlocking the feathers, either acted as a sound absorber which would dampen out any small reverberations near the wing, or that it worked in conjunction with the leading edge comb to further slow the airflow in the boundary layer of the wing. Graham (1934) also mentions fishing owls which do not hunt small mammals, but rather feed on fish and crustaceans. These owls have lost (or never developed to begin with) the unique feather features of all other owls, and indeed have been shown to produce significant noise in flight similarly to most other birds.

Thorpe and Griffin (1962) measured the ultrasound produced by owls and other similarly sized birds, and found owls to produce no measurable ultrasound, while other comparable birds (pigeons and hawks) produced significant ultrasound during flapping flight. They also made measurements on the fishing owls mentioned by Graham (1934) and found them to also produce ultrasound during flapping flight.

Kroeger, Gruschka, and Helvey (1972) published an extensive biological, aerodynamic, and acoustic study of owl flight as a step towards developing an ultra-quiet aircraft. During a preliminary acoustic measurement, they found that owls produce significant flight noise, but that this noise is strongly shifted to low frequencies. This is consistent with the fact that the owl's prey has poor hearing at lower frequencies. This was investigated further using prepared owls' wings mounted in a wind tunnel. An aeroelastic compliance of the wing was observed at a frequency of around 15 Hz, which corresponded to the peak frequency of the noise produced in flight. The net effect of the compliant wing was to shift the boundary layer turbulence frequency spectrum to very low frequencies. Particular focus was also placed on the leading edge serrations and their effect on the flow over the wing. It was shown that the serrations acted as a vortex sheet generator which, in combination with the leading edge slot and tip feathers, maintained attached laminar flow over the entire wing for angles of attack up to 30 degrees. Kroeger *et al.* (1972) state that no proof could be found as to the purpose of the velvety downy coating on the top surface of the wing, but offered two hypotheses, the first of which stated that the downy coating allows a thin film of air to pass between the wing feathers which thickens the boundary layer and reduces trailing edge noise. The second hypothesis stated that the downy coating acts to lubricate the feathers as they slide over one another such that they are silent when the owl changes wing configuration just before striking its prey, and this hypothesis is consistent with the observations of Graham (1934).

Lilley (1998) offers an explanation for the function of the downy coating that is consistent with the hypothesis of the current study. He first shows the noise-reducing characteristics of the leading and trailing edge features of the owl's wing, but argues that even with these features, significant aerodynamic noise will nonetheless be produced above 2kHz. He dismisses the description of the velvety down as a simple sound absorber, since the majority of sound would be radiated away from the trailing edge. Therefore, he argues that the velvety coating must act to eliminate the radiated sound at the source, specifically by dampening the turbulence within the boundary layer over the wing. He argues that the small diameter and compliant nature of the

individual hairs comprising the coating act to dampen the small scale eddies which cause high-frequency noise, essentially providing a bypass mechanism which dampens the pressure fluctuations at a significantly smaller frequency than the natural viscous damping of small-scale eddies.

Klan *et al.* (2009) developed a detailed experimental model of an artificial owl based wing using 3-dimensional scans of deceased owls' wings, while carefully accounting for the changes that occur (such as drying of muscle tissues) that lead to changes in wing shape. Additionally, the configuration of the wing in flight was taken from photographs and videos so that parameters such as twist could be matched to their natural states. They tested their artificial owl wing in a low-speed wind tunnel with a square cross-section of width 500mm, and with a length of 1.2m. Their measurements were performed at chord Reynolds numbers of 20,000, 40,000, and 60,000, corresponding to flow speeds of 1.8, 3.5, and 5.3 m/s respectively, and at angles of attack of -3^o, 0^o, 3^o, and 6^o. Data was taken of mean pressure measurements on the surface, oil flow visualization, and particle image velocimetry. The main flow feature of the clean wing was a large separation region starting near the leading edge. For a chord Reynolds number of 40,000, at low angles of attack, the flow reattached near the mid-chord, but at 6^o the flow was fully separated. They then attached a velvet coating designed to mimic the structure of the owl's downy coating to the suction side of the wing. The size of the separation bubble was greatly reduced at low angles of attack, but the flow still fully separated at 6^o angle of attack. This could simply be attributed to the velvet tripping the boundary layer, as Klan *et al.* (2009) show that the transition location is moved upstream with the addition of the velvet.

Klan *et al.* (2012) expanded on the work of Klan *et al.* (2009) and tested a new velvet surface which, rather than matching the dimensions of the owls' wing coating, featured longer and more flexible fibers. They tested at identical conditions, and observed that the new velvet surface was able to prevent the 2D airfoil from stalling at 6^o angle of attack and a chord Reynolds number of 60,000. They also showed that, at 0^o angle of attack and a chord Reynolds number of 40,000, the new velvet surface actually delayed the onset of transition, whereas the original velvet surface, designed to match the owl's natural surface, shifted the transition point upstream of the transition location for the clean surface. They describe the development of a Kelvin-Helmholtz instability above the velvet surface due the increased shear stress in this region. This instability leads to a more intense transition which may reduce the size of separation bubbles over the wing or delay stall at higher angles of attack.

As stated above, to relate the flow over owls' wings, specifically over the small fibers comprising the downy coating, to the attenuation of surface pressure fluctuations, the study of flow over plant canopies embedded in the Earth's boundary layer will also be reviewed.

1.2.3 Flow over Plant Canopies

Raupach and Thom (1981) give a review of the investigations into flow through and over plant canopies. Of particular relevance to the problem at hand are the following phenomena. First, momentum within the flow is absorbed by the canopy by form and skin-friction drag on the individual elements. Second, the individual elements of the canopy generate turbulent wakes, the net effect of which are to convert mean kinetic energy stored in the flow to turbulent kinetic energy. The turbulence is biased towards length scales characteristic of the elements of the canopy. The mean wind profile (essentially the boundary layer profile) within the canopy is retarded by the drag of the plant structures. The wind profile can be described by an exponential function:

$$\frac{U(z)}{U(h)} = \exp[\alpha_1 \left(\frac{z}{h} - 1\right)] \tag{1.5}$$

Here, h is the height of the canopy, z is the vertical location, and α_1 is an attenuation coefficient, which for most canopies lies between 2 and 3.

Finnigan (2000) describe the primary characteristics of the turbulence in the boundary layer with the presence of a canopy to be more analogous to those of a mixing layer than to conventional boundary layer flow. These characteristics are the result of the inflectional boundary layer profile (similar to the exponential profile described by Raupach and Thom (1981)) which is unstable. This sets up a system of Kelvin-Helmholtz instability waves above the canopy which dominate the flow above the canopy and have significant effect on the turbulent length scales within the flow. He also describes a spectral short cut mechanism which results in energy transfer from large scale turbulent eddies to much smaller scales through the production of wakes by the individual canopy elements. This spectral short cut is very similar to that described by Lilley (1998) for flow over owls' wings.

1.3 Visual Study of Owls' Feathers

As discussed above, the velvety down coating has long been identified as a unique feature of the owl's wing which assists in the elimination of flight noise. However, the precise function of the velvety down, and the mechanism which it exploits in order to reduce noise, is not well understood. Numerous hypotheses and conjectures have been offered, but solid proof as to its function is notably absent. As such, the first step to developing a true understanding of the velvety downy coating was direct observation of the structure of the coating itself. To this end, several feathers were gathered which were molted from several species of silently-flying owls and photographed using a microscope. In addition, before any experimental analog could be developed which would mimic the owl's feathers, it was necessary to understand the structure of the fibers and to determine their average length and open area percentage.

Figure 1.1 Owl feathers (left) examined using an imaging microscope (right).

Four feathers from some of the world's largest owls were examined in depth (Figure 1.1): two feathers from an eagle owl (bubo bubo), one feather from a great grey owl (strix nebulosa), and one feather from a snowy owl (bubo scandiacus). All of these owls are known to fly silently. The feathers were molted naturally and were determined to be coverlet feathers (either primary or

secondary). As such, they were assumed to be representative of the majority of the feathers insofar as the downy coating was concerned. As would be expected from all owl's feathers, the top surface of the feathers featured the velvety downy coating, whereas the bottom surface of the feather was smooth and exposed only the structural elements of the feathers. This was observed simply by touch and observations by the unaided eye.

The feathers were imaged using a Nikon D300S digital camera attached to a Nikon SMZ1500 microscope (Figure 1.1). The camera shutter was fired through an external computer program to eliminate movement of the apparatus during imaging. The fine focal adjustment of the microscope along with an extremely shallow depth of field were used to image different layers of the downy coating and to estimate the thickness of the coating. This process is described in more detail below. In order to calibrate the microscope images to obtain length measurements, an Edmund 53713 micrometer (Figure 1.2) was imaged at the same magnification levels used for the feather images. A 1mm scale was taken from these images.

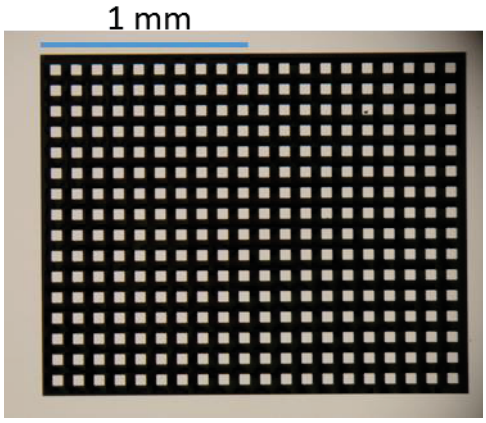

Figure 1.2 Micrometer used to scale images

Figure 1.3 shows a representative photo taken of the great gray owl feather along with a 1mm scale taken from the micrometer described above, and the inset shows the location on the feather from which this image was taken. The picture shows the basic structure of the velvety, downy coating, which appears to be comprised of very fine hairs rising from the surface with numerous small barbs protruding from each hair. The average length of the hairs is on the order of 1-2 mm, and the average length of each barb is 0.05-0.1 mm. The diameter of the hairs is extremely small, on the order of 0.01-0.02 mm. Using image processing, it can be estimated that the open area percentage of the downy coating is roughly 70%, which means the downy coating only truly covers 30% of the surface area of the feather.

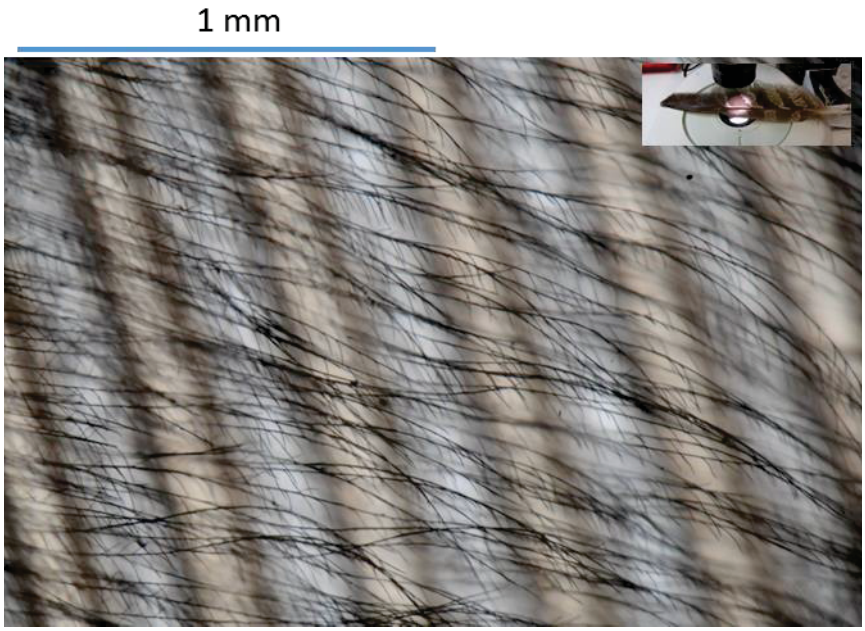

Figure 1.3 Representative image of great gray owl's feather

At this point, the only unknown parameter was how far the downy coating extends above the surface of the owl's feather. Two methods were derived to measure this dimension using a microscope, which is only capable of 2D imaging. First, a thin strip of feather was separated from the main feather and taped to the side of a structure which would hold the strip in place. It was taped in such a way as to face the side of the feather towards the microscope such that a representative cross-section of the feather would be imaged. This method can be seen in Figure 1.4.

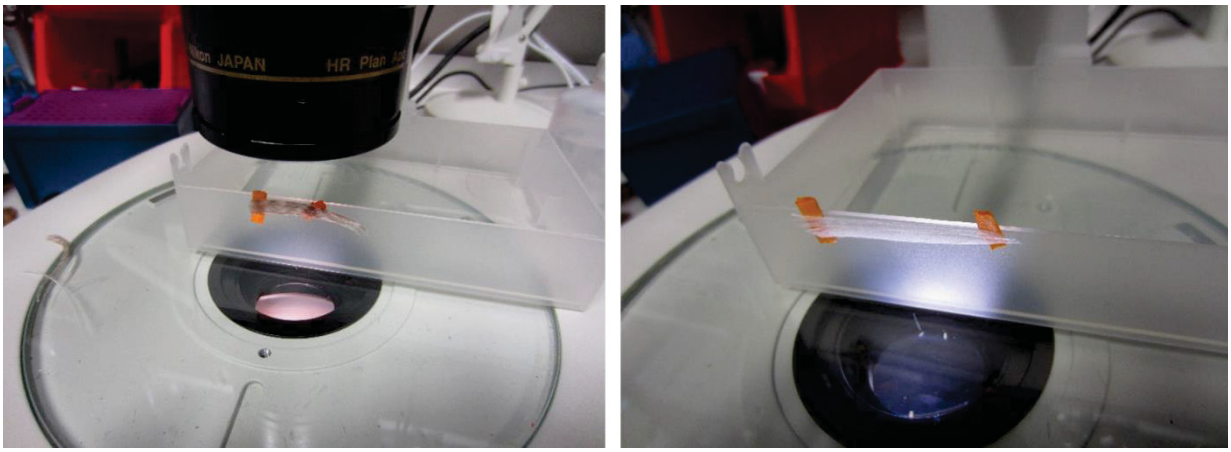

Figure 1.4 Method for imaging the cross-section of the feathers

The uncertainty of this method is in the fact that a strip of feather must be chosen that does indeed represent the rest of the feather, as well as in the possibility of damaging the downy coating when the strip is removed. Thus, a second method was derived which involved calibrating the focal adjustment of the microscope itself. The microscope featured a notched knob, seen in Figure 1.5, which gave very fine focal adjustments by moving the entire microscope apparatus up and down. By counting the number of knob notches which moved past a fixed point on the microscope

base, the focal plane could be moved by a precise, consistent amount. The total focal plane adjustment allowed by the knob was 6mm, which corresponded to 57 knob notches moving past a fixed point on the microscope. Therefore, each knob notch corresponded to a change of 0.105 mm in the focal plane location. Finally, by counting the number of notches necessary to bring different features of the feather and downy coating into focus, measurements could be made in the height dimension of the feather with reasonable accuracy.

Figure 1.5 Calibrated focal knob on microscope

Figure 1.6a shows the cross-sectional image of the snowy owl feather, while Figure 1.6b shows the cross-section of the great grey owl feather. From these images, we can see that the downy coating is roughly 1-1.5 mm thick, and the barbs protruding from the hairs are even more apparent in this orientation.

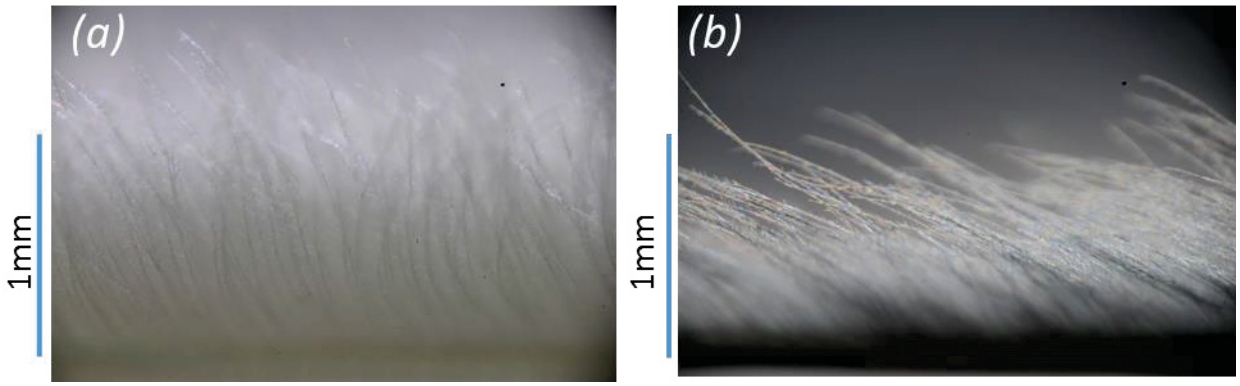

Figure 1.6 Cross-sectional view of snowy owl feather (a) and great gray owl feather (b)

Figure 1.7 shows different layers of the downy coating on the great gray owl feather. Using the calibration of the focal plane described above, it was estimated that the coating is roughly 0.5-1 mm thick. As such, this method yielded slightly lower estimates for the thickness of the coating compared to the cross-sectional imaging. However, this method does give a better idea of the vertical structure of the downy coating. It can be seen from the different layer images that there are very few hairs near the surface of the feather. The hairs clearly grow out of the feather and then bend over to form a sort of canopy suspended above the surface of the feather. This explanation is supported by the cross-sectional view in Figure 1.6.

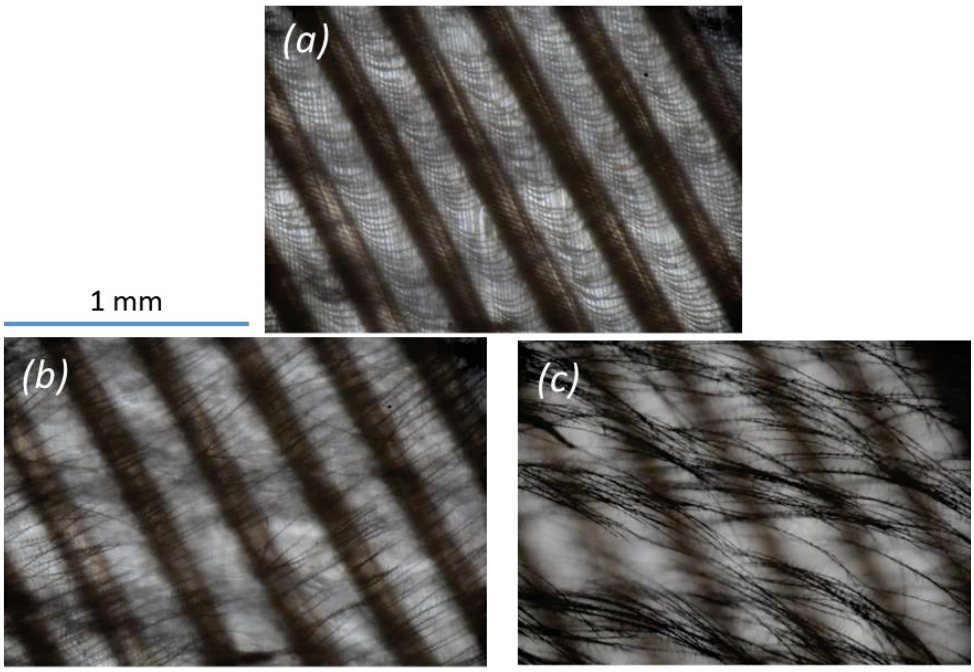

Figure 1.7 Base (a), middle (b), and top (c) layers of great gray owl feather.

During the time of these measurements and observations, it was also decided to investigate commercial velvet as a potential experimental substitute, in the hopes that the commercial velvet would have similar structure and dimensions. If this were the case, the commercial velvet could be applied to surface roughness, and any noise cancelling effects could be observed and related to those of the owl's downy coating. However, as Figure 1.8 shows, the commercial velvet has very different characteristics from the owl's downy coating. The structure of commercial velvet, rather than being comprised of barbed hairs which bend over, is made of bundles of stiff, cylindrical fibers which rise vertically from the surface. The bundles are closely packed, and as such have a much smaller open area percentage than the owl's downy coating. Because of these observed differences in the structure of velvet compared with the owl down, commercial velvet was not pursued as an experimental substitute.

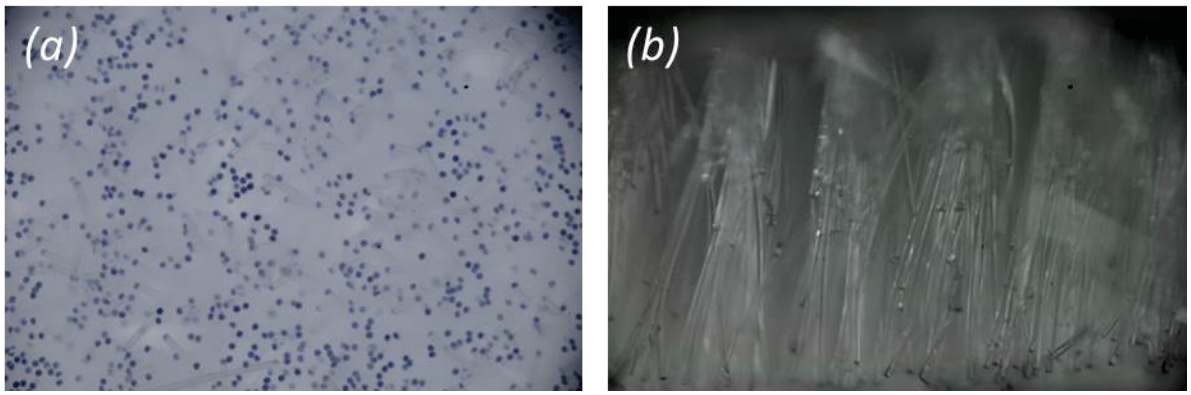

Figure 1.8 Microscopic images of commercial velvet showing straight, bundled fiber in top down view (a) and side view (b)

1.4 Objectives

The present study takes inspiration from the structure and features of the owl's feather in order to develop and test a surface with the goal of demonstrating the reduction of noise caused by flow over a rough surface. This paper details the development and testing of several bio-inspired treatments using the Virginia Tech Anechoic Wall-Jet Facility. Far-field sound and surface pressure fluctuation data are obtained for a total of eight owl-inspired configurations shrouding various rough surfaces. The objectives of this paper are the following:

- Develop an experimental surface or structure which mimics the form and supposed function of an owl's feather, with particular attention to the velvety coating on its top surface, and can be applied to a rough surface such that the flow-induced noise from the surface is reduced.
- Analyze the effects of this surface or structure on the surface pressure spectra and far-field sound levels in the presence of a smooth wall, as well as various rough surfaces.
- Determine the effects of the particular geometric parameters which define the surface or structure on the surface pressure spectra and far-field sound.
- Refine the surface or structure to eliminate any additional noise due to the item itself.
- Compare the effects of this surface or structure on surface pressure spectra to the expected effects of a similar forest-type canopy.

Chapter 2 - Experimental Setup

2.1 Experiment Design

Once the structure of the owl's downy coating was known, it was necessary to devise an experimental analog that mimicked the key elements and characteristics of the coating, but that was also deterministic or describable. In addition, the scale of the experimental apparatus was required to be sufficiently large such that it would demonstrate utility in common engineering structures. While the owl's downy coating itself was comprised of microscopic hairs, application to structures such as submarines or buildings would likely require significantly larger features.

Because the goal of this investigation was the reduction of roughness noise, the experimental apparatus would, by default, need to include surface roughness at its most basic layer. This surface roughness would then be augmented with an additional feature inspired by the owl's downy coating with the purpose of attenuating the scattered noise. The original conceptual design called for individual flexible elements to be placed among a fetch of surface roughness (hemispheres, sandpaper, etc.), with the hopes that these flexible elements would absorb some of the turbulent energy in the boundary layer, which would result in the attenuation of surface pressure fluctuations, as well as a reduction of far-field noise. However, this initial idea presented serious and difficult design and manufacturing issues which were not easily solved. In particular, some of the most difficult questions regarding these flexible elements were:

- Should the entire element be flexible, or should it be a stiff element with an elastic attachment point at the substrate?
- How elastic/flexible should these elements be? If the elements were sufficiently flexible such that it could see the effects of the relatively low flow speeds in the boundary layer, would they return to a known position in the absence of flow?
- What material should be used for the elements, as the chosen material would affect the elasticity?
- What dimensions should these elements have?
- How would these elements be mounted among the surface roughness, particularly in the case of the sandpaper roughness?
- How would the surface be manufactured? Would each element have to be placed individually?

While the path to answer these questions would likely lead to an interesting study regarding the effectiveness of noise-canceling flexible roughness elements, and their dependence on particular parameters, another design concept offered a much more efficient design and manufacture schedule and would (hopefully) be equally or more effective in reducing noise. This idea was developed after re-examining the structure of the owls' downy coating, in particular the effective "canopy" structure of the coating as a whole. One could reasonably suppose that the coating's primary function was to replace the hard surface of the feather itself with a more compliant and porous surface that would be "seen" by the main flow. Regarding the coating as a collection of individual hairs, one could then imagine that each hair's primary function was only to contribute to the structure of this porous "canopy". If this were the case, the "stalk" of each hair

would not be important to the function of the downy coating as long as the top layer of each hair was still elevated above the surface of the feather.

Following this reasoning, the downy coating could be simulated using only a porous material which could be elevated above a fetch of surface roughness. This solution would eliminate the need for individual elements by essentially decoupling the two relevant surfaces (the surface roughness and downy coating analog), and would allow each to be tested independently.

2.2 Virginia Tech Anechoic Wall Jet Facility

The Virginia Tech Anechoic Wall-Jet Wind Tunnel (Figure 2.1) was used for the entirety of this investigation. The tunnel was built in 2005 for the specific purpose of measuring noise produced by flow over surface roughness. The tunnel produces flow at a nozzle, which is adjacent to a long, wide aluminum plate. The flow develops into a boundary layer flow topped by a mixing layer, and microphone instrumentation is placed above the plate, well outside of the flow. The surface to be studied is mounted directly to the wall-jet plate beneath the microphones. Surface pressure microphones may also be placed in the plate itself.

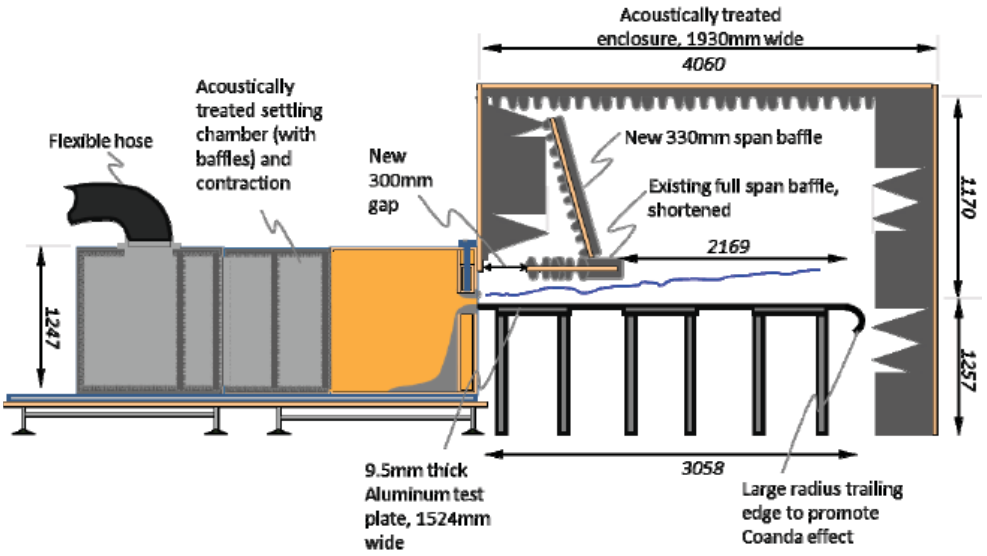

Figure 2.1. Schematic side-view of Virginia Tech Anechoic Wall-Jet Wind Tunnel

A centrifugal fan, enclosed by medium density fiberboard (MDF), drives the flow, and is separated from the rest of the tunnel by a flexible rubber hose. The flow moves through the hose into an acoustically treated settling chamber which features baffles to eliminate the direct propagation of fan noise through the chamber. The flow is then accelerated by a short contraction just upstream of the 1219 mm wide nozzle. The nozzle height, while originally adjustable, was fixed at 12.7 mm in order to eliminate leaks present around the adjustment mechanism. The flow speed at the nozzle can be set to a high degree of accuracy between 20 and 60 m/s using measurements of pressure both in the settling chamber (total pressure) and in the test section (static pressure). The pressure differential is measured with a Setra 239 pressure transducer with a range of $\pm$3.75 kPa. To measure the temperature in the flow, a thermocouple is placed at one spanwise end of the nozzle, at the edge of the nozzle flow, and is connected to an Omega DP86T temperature display with analog output.

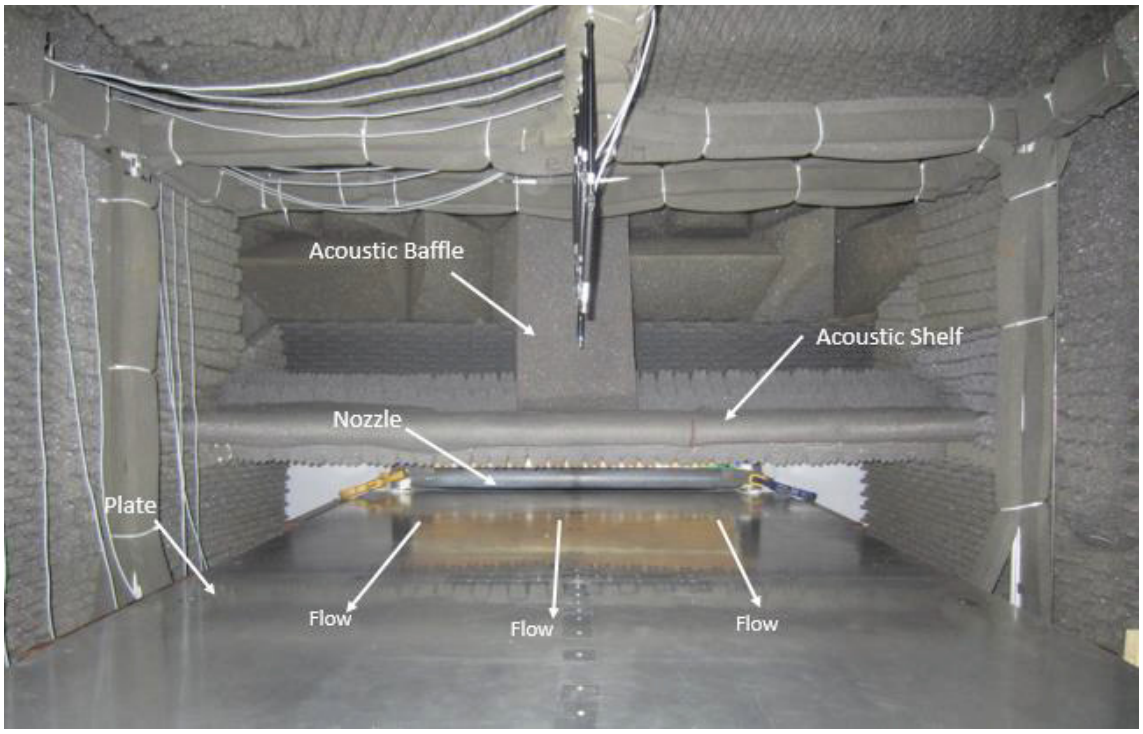

Figure 2.2. Photographic view of the test-section of the Wall-Jet Tunnel, as viewed from the downstream end of the test plate

Downstream of the nozzle, the air flows and decays over a 1600 mm wide plate that is 3058 mm long (Figure 2.2). The plate is wide enough to contain the full jet, and studies by Grissom (2007) have shown that edge effects do not contaminate the background far-field noise present during tunnel operation. The plate is contained within an acoustically treated chamber that features egg crate acoustic foam on the ceilings and side walls, and large wedges on the upstream and downstream walls. The egg crate foam is effective at damping noise above about 1900 Hz, while the acoustic wedges damp all noise above 188 Hz. The chamber has a 50mm gap around the bottom through which the flow can dissipate into the lab atmosphere.

An acoustically treated shelf is placed above the plate near the upstream wall which serves to shield the far-field microphones from the flow noise produced at the nozzle (Figure 2.2). The shelf extends the entire width of the anechoic chamber. It originally extended from the wall above the nozzle to 924mm downstream of the nozzle. However, it was found through flow velocity measurements downstream of the nozzle that, in this configuration, the shelf blocked the flow of air that was naturally caused by the entrainment of fluid above the nozzle. The blockage caused by the shelf resulted in a very limited spanwise uniform region downstream of the nozzle (only about 400mm wide). To remedy this situation, a 300 mm gap was opened between the wall above the nozzle and the shelf for improved air circulation. An additional acoustically treated baffle was placed above the gap at the spanwise center of the plate to compensate for the decreased ability of the shelf to shield the far-field microphones from the nozzle noise (Figure 2.2). This new configuration extended the spanwise uniform region to nearly 700mm with a minimal increase in background noise levels.

2.3 Boundary Layer Measurements

In order to fully characterize the flow in the tunnel, velocity measurements were recorded at several streamwise locations along the flat plate. To relate these discrete measurements to flow throughout the tunnel, some knowledge of the development of the flow structure is necessary. Wygnanski *et al.* (1992) describe velocity measurements performed on a different wall-jet facility to analyze the development of the flow as it moves over a flat plate. They found that the "law of the wall" applies only to the viscous sublayer for wall-jet flows, but they state that the "law of the wake" can be applied to the inner region of wall-jet flows. Most importantly, they developed several formulations to relate the maximum velocity in the boundary layer and the boundary layer thickness to non-dimensional flow properties using the fact that the boundary layer profiles were self-similar once the flow was fully developed. Slightly modified versions of these equations are given later in this section. These relations allow for the full characterization of flow development in the wall-jet facility used for this study.

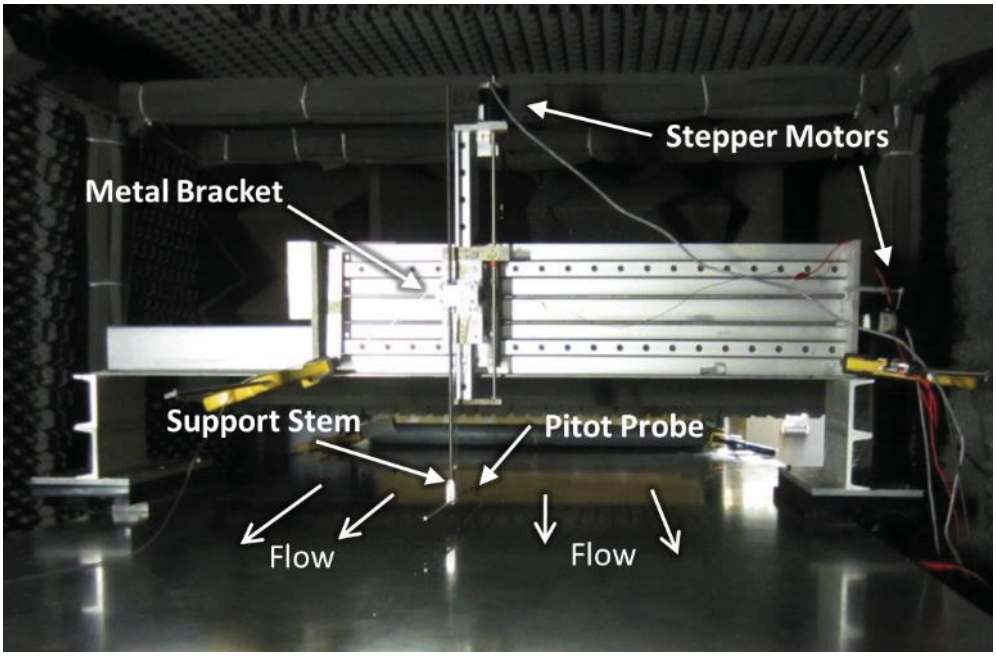

Figure 2.3. Photographic view of the boundary layer measurement system mounted on the test plate

Flow velocity was measured using a flattened-head Pitot probe manufactured in-house. The support structure for the Pitot probe can be seen in Figure 2.3. The probe itself can be seen in Figure 2.4, while the dimensions of the probe tip are given in Figure 2.5. Note that the thicker wall could have been placed above the probe opening to obtain measurements closer to the wall, but the asymmetry of the probe was unknown to the author at the time of the measurement, and visual inspection did not readily reveal the different wall thicknesses. To support the probe, a metal frame was placed on the plate which featured two 6.4 mm thick base plates spaced 1.32 m from edge to edge. The vertical support structures attached to these bases were spaced 1.44 m apart. These dimensions were such that the supports could be placed outside the main region of flow, as the nozzle is 1.22 m wide. A cross-bar ran between the two vertical supports, such that the bottom of the cross-bar was elevated 216 mm above the plate. This allowed the majority of the flow to pass beneath the cross-bar unhindered. A mechanism was placed on the cross-bar

which featured two Compumotor 557-83-MO stepper motors connected to threaded rods, which were in turn connected to a metal bracket. Finally, a 3.2 mm diameter rod was held vertically by this bracket, and the rod extended below the cross-bar. A right-angle bracket was used to connect this vertical rod with a similar 3.2 mm diameter rod oriented horizontally to which the Pitot probe itself was attached. In this way, the two stepper motors could control the vertical and spanwise movement of the Pitot probe. The streamwise position was set by manually moving the entire structure.

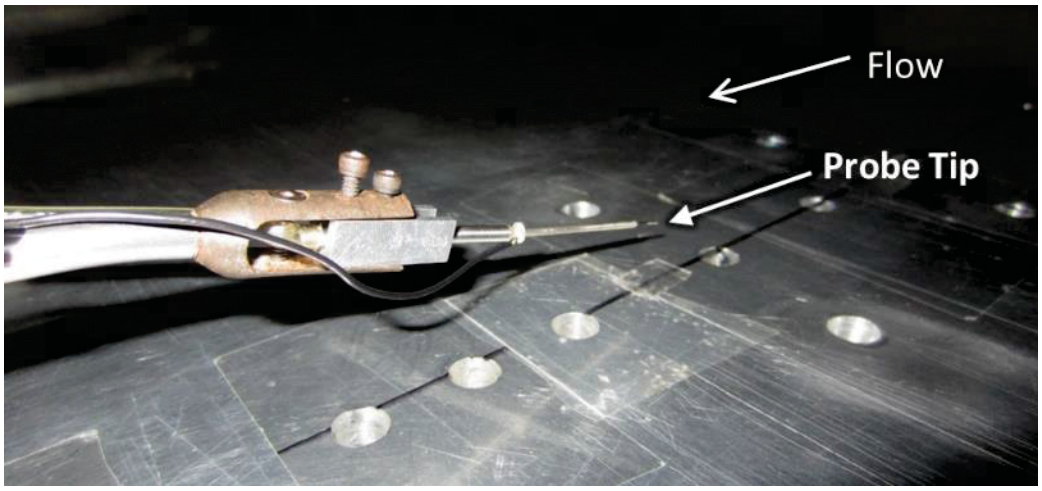

Figure 2.4. Photographic view of the flattened-head Pitot probe in place above the test plate

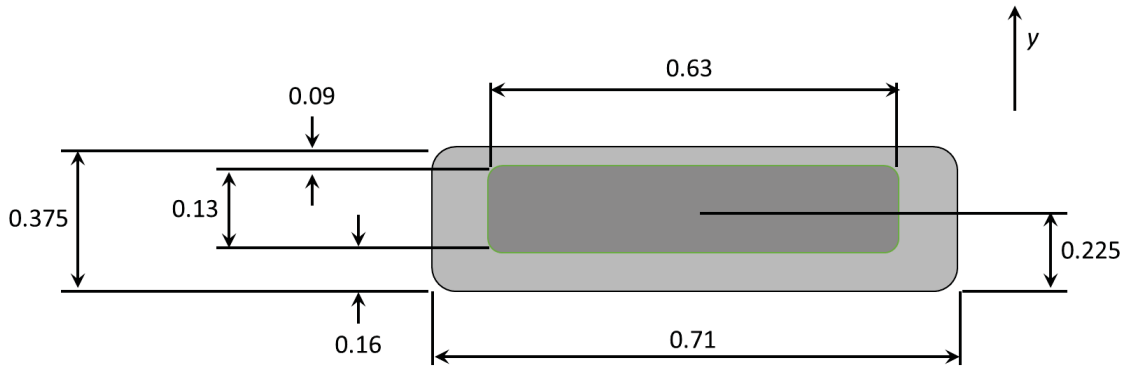

Figure 2.5. Schematic view of the tip of the flattened-head Pitot probe. The darkest area represents the open port.

The Pitot probe was connected to a Setra 239 pressure transducer, which in turn was connected to an Agilent E1432 16-bit digitizer, along with the transducer used to measure the jet velocity and the temperature probe (described in Section 2.2). Measurements of jet velocity, local velocity, and temperature were taken simultaneously. Mean velocity data was calculated using the average of 50 records containing 1024 data points sampled at 6400 Hz. This resulted in a total measurement time of eight seconds.

In order to detect contact between the plate and the probe, an electrical circuit was set up which would be closed upon contact with the metal plate. A digital multimeter was used to monitor the resistance in the circuit. Boundary layer profile measurements extended from the contact location to 150 mm above the plate, and were taken at the spanwise center of the plate. Measurements were taken at streamwise locations of 1054, 1257, 1372, 1410, 1562, and 1867 mm downstream of the nozzle, and for flow speeds at the nozzle of 30, 40, 50, and 60 m/s.

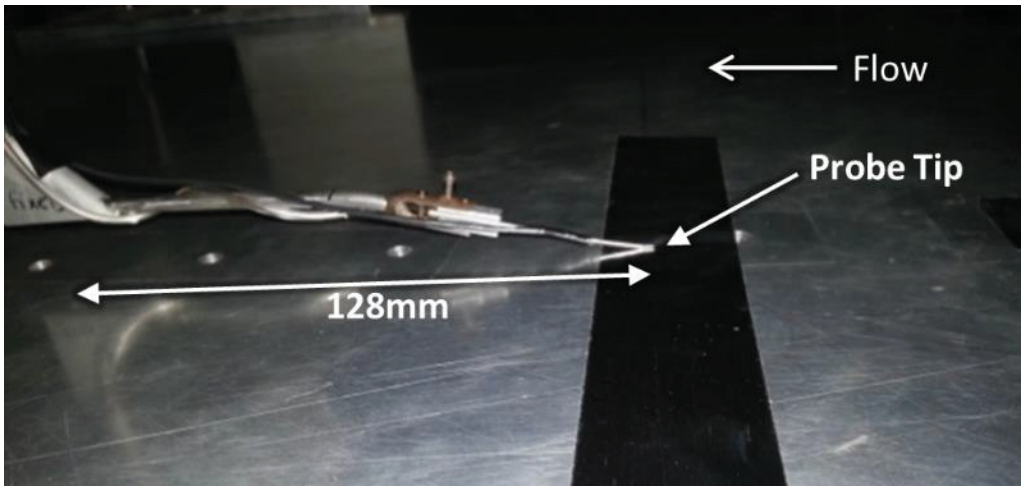

Figure 2.6. Photograph showing the forward extent of the probe in front of the mounting bracket

Some discussion of the streamwise extension of the probe is necessary to understand the uncertainty of the measurements made in this configuration. To minimize the upstream effect of the traverse system and probe mount, it was necessary to place the probe far forward of the structure using a long stem. However, this introduced an additional problem in that the structural rigidity of such an arrangement was not sufficient to prevent buffeting and shaking of the probe by the passing airflow. As such, the probe head was placed about 230 mm upstream of the structure as a compromise between competing factors. The final arrangement can be seen in Figure 2.6. To further minimize vibration of the structure, the entire support structure was firmly clamped to the plate itself to minimize shaking. During tests, the stability of the probe was visually verified with the tunnel running at maximum velocity, and only minimal shaking was observed and was estimated to introduce an uncertainty of ± 0.5 mm to the set measurement location. The uncertainty of the stepper motors themselves was not measured, but was assumed to be much less than that due to shaking, as the motors were able to consistently move the probe by increments approaching 0.02 mm. In addition to the uncertainty in the position, the uncertainty of the velocity values themselves was assumed to be approximately ± 0.3 m/s and was primarily judged based on the scatter observed in the data.

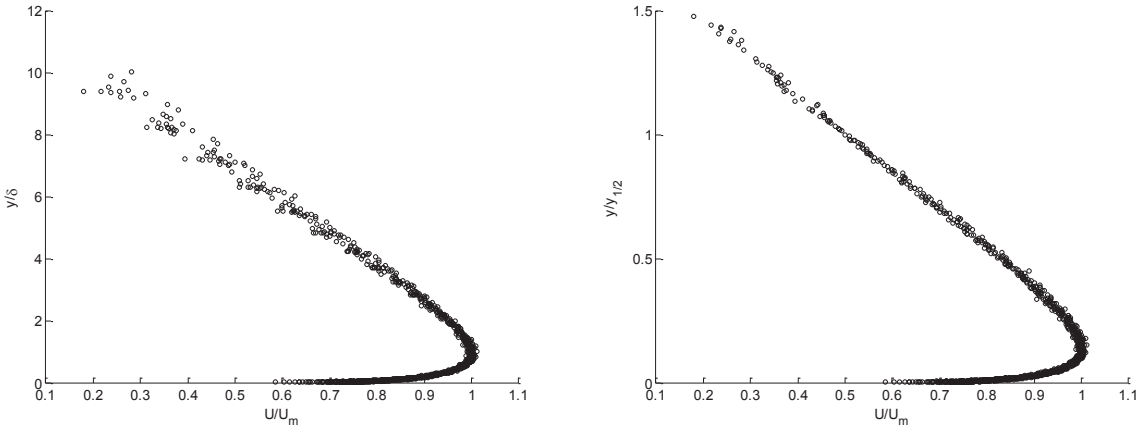

Figure 2.7. All measured boundary layer profiles normalized on maximum velocity and boundary layer thickness (a) or $y_{1/2}$ (b)

The measured boundary layer profiles, normalized on boundary layer thickness and maximum velocity can be seen in Figure 2.7. The profiles were also normalized on maximum velocity and the quantity $y_{1/2}$, which is defined as the vertical distance to the point where the velocity decays to half the maximum value in the outer region of the boundary layer, as shown in Figure 2.7. As can be seen in Figure 2.7, the boundary layer profiles are self-similar when normalized. Specifically, the normalization of the vertical distance on boundary layer thickness leads to excellent collapse of the data in the inner region of the boundary layer, while normalization on $y_{1/2}$ improves the collapse of the data in the outer region with a slight increase in spread of the inner region data.

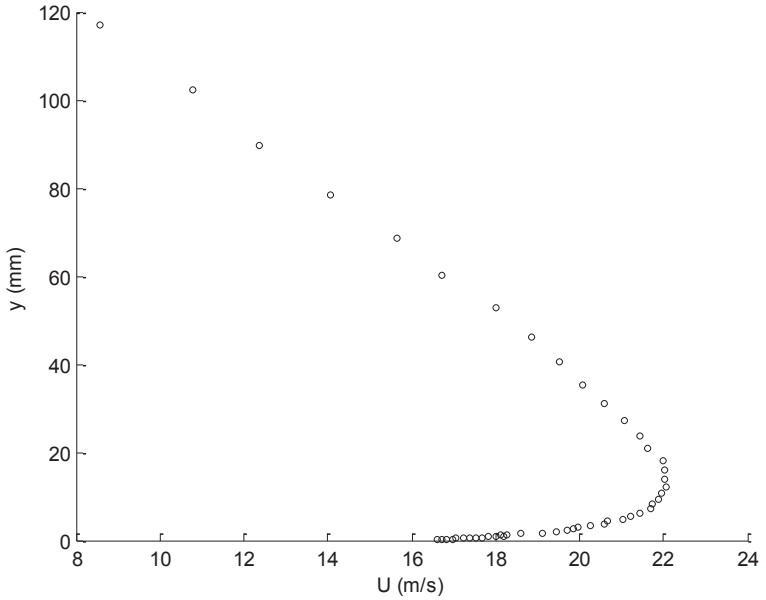

Figure 2.8. Reference profile obtained at 1257 mm downstream of the nozzle with a jet speed of 60 m/s

In order to use these profiles to characterize the flow everywhere in the tunnel, the boundary layer parameters first needed to be extracted from each profile. First, a reference profile was chosen that presented the least amount of scatter in the data, particularly near the location of maximum velocity. For the current data set, the reference profile was obtained at a streamwise location of 1257 mm with a jet speed of 60 m/s. The boundary layer thickness was then input as 14 mm, which was chosen (somewhat subjectively) as the location of maximum velocity. Next a curve fit, which approximated the profile close to the wall as a function of velocity raised to a variable power, was used to extrapolate the data points closest to the wall in order to determine the integral thicknesses using the following relations:

$$\delta^* = \int_0^\delta \left(1 - \frac{U}{U_m}\right) dy \tag{2.1}$$

$$\theta = \int_0^\delta \left(1 - \frac{U}{U_m}\right) \frac{U}{U_m} dy \tag{2.2}$$

Here, δ^* is the displacement thickness, θ is the momentum thickness, δ is the boundary layer thickness, U is the local velocity at a point in the boundary layer, and U_m is the maximum velocity in the boundary layer. These integrals were evaluated numerically using the data collected by the flattened-head Pitot probe and the extrapolated data near the wall. All of the boundary layer parameters at each location are shown in Table 1.

Table 1. All boundary layer parameters obtained from the measured profiles

Run	X (in)	X (mm)	U_{jet} (m/s)	Re	T_f (K)	U_{ref} (m/s)	U_m (m/s)	δ (mm)	δ^* (mm)	θ (mm)	Re_m	Re_j	Re_x	C_f	$y_{1/2}$ (mm)
1	49.5	1257.3	30	45953	296.3	30.04	10.67	13.96	0.795	0.664	8972	22976	2274664	0.0060	91.8
2	49.5	1257.3	40	61645	295.7	39.87	14.38	13.65	0.761	0.641	11949	30823	3051436	0.0057	96.0
3	49.5	1257.3	50	76614	297.0	49.91	18.18	14.31	0.717	0.608	15716	38307	3792411	0.0054	97.4
4	49.5	1257.3	60	91494	298.2	60.06	22.05	14.00	0.717	0.616	18516	45747	4528975	0.0053	100.5
5	41.5	1054.1	30	46462	295.7	30.03	11.38	12.44	0.723	0.599	8627	23231	1928162	0.0061	79.1
6	41.5	1054.1	40	61749	296.2	40.05	15.53	12.44	0.671	0.566	11729	30875	2562588	0.0057	81.2
7	41.5	1054.1	50	76691	297.2	50.03	19.58	12.46	0.654	0.560	14720	38345	3182658	0.0055	85.1
8	41.5	1054.1	60	91139	298.6	59.96	23.55	12.43	0.610	0.528	17519	45570	3782284	0.0053	85.8
9	54	1371.6	30	46712	294.4	30.00	10.32	16.27	0.978	0.793	10291	23356	2522442	0.0059	106.4
10	54	1371.6	40	61987	295.3	40.03	13.99	15.41	0.856	0.719	13147	30994	3347300	0.0056	106.9
11	54	1371.6	50	76826	296.6	49.98	17.57	15.71	0.777	0.668	16711	38413	4148617	0.0054	107.8
12	54	1371.6	60	91355	298.3	60.04	21.33	15.20	0.795	0.685	19426	45677	4933148	0.0052	110.6
13	55.5	1409.7	30	46622	295.4	30.18	10.11	15.83	1.006	0.799	9736	23311	2587536	0.0059	107.4
14	55.5	1409.7	40	61610	296.1	40.03	13.62	16.41	0.925	0.753	13544	30805	3419330	0.0056	109.2
15	55.5	1409.7	50	76614	296.3	49.96	17.31	16.42	0.901	0.749	17158	38307	4252053	0.0053	112.5
16	55.5	1409.7	60	91003	298.2	59.99	20.84	16.19	0.832	0.692	20153	45501	5050650	0.0052	115.3
17	61.5	1562.1	30	46224	295.8	30.05	9.53	17.99	0.950	0.786	10380	23112	2842770	0.0059	119.1
18	61.5	1562.1	40	61430	296.1	40.00	12.93	17.01	0.887	0.746	13294	30715	3777933	0.0056	123.7
19	61.5	1562.1	50	76294	296.6	49.99	16.48	18.64	0.994	0.852	18452	38147	4692095	0.0053	124.2
20	61.5	1562.1	60	90352	298.4	59.82	19.75	18.77	0.872	0.744	22041	45176	5556651	0.0051	129.4
21	73.5	1866.9	30	45869	296.3	29.99	8.83	21.68	1.344	1.094	11523	22935	3371388	0.0057	149.5
22	73.5	1866.9	40	61106	296.5	40.02	12.04	22.46	1.239	1.039	16260	30553	4491273	0.0054	150.4
23	73.5	1866.9	50	76341	295.6	49.88	15.21	21.50	1.220	1.031	19711	38170	5611049	0.0052	156.5
24	73.5	1866.9	60	90755	297.6	60.02	18.37	21.79	1.119	0.950	23826	45378	6670515	0.0050	156.5

Once these parameters were known, it was necessary to fit the data to the power-law relations of Wygnanski *et al.* (1992). These relations were of the form:

$$\frac{U_m}{U_O} = A_U Re_j^{n+1} Re_x^n \tag{2.3}$$

$$\frac{\delta^*}{b} = A_D Re_j^{p-2} Re_x^p \tag{2.4}$$

$$\frac{y_{1/2}}{b} = A_Y Re_j^{m-2} Re_x^m \tag{2.5}$$

$$\delta = A\delta^* \tag{2.6}$$

$$\theta = B\delta^* \tag{2.7}$$

Here, U_O is the jet velocity, A_U, A_D, A_Y, A, and B are constants to be determined, Re_j is the Reynolds number based on jet velocity and nozzle height, Re_x is the Reynolds number based on jet velocity and distance to the measurement location, b is the nozzle height, and n, m, and p are power-law constants to be determined.

From the data collected with the flattened pitot probe, experimental values could be used in the above relations for all variables except the constants and power-law constants. By considering all data sets, with different streamwise locations and flow speeds, a best-fit (method of least squares) algorithm was used to estimate the constants and power-law constants. The results are shown in Table 2.

Table 2. Power-law constants which characterize the flow parameters in the Wall-Jet Tunnel

A_U	1.6814
A_D	0.0063
A_Y	0.015
A	18.2966
B	0.8357
n	-0.4702
p	0.9099
m	1.0651

Figure 2.9 through Figure 2.13 compare the calculated values (ordinate) for U_m, δ, and δ^* with the actual measured values (abscissa) at each measurement point. The diagonal line denotes the line of perfect fit and has a slope of one. The figures show that the least error occurs for the maximum velocity and half-height fits, while the boundary layer parameters show significantly more scatter, with a maximum error of about 10%.

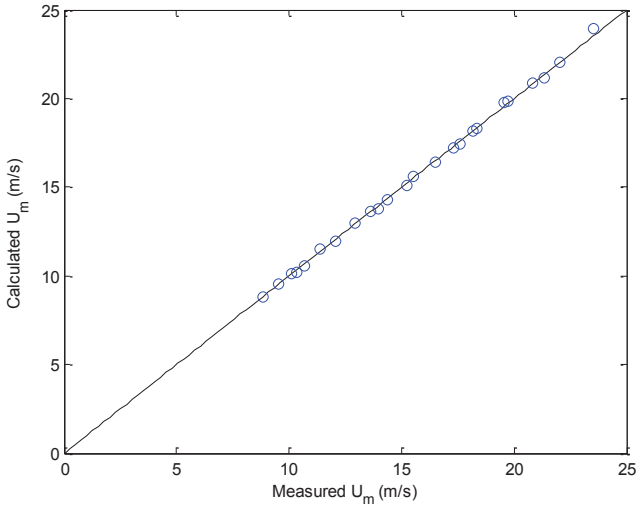

Figure 2.9. Comparison of measured values of U_m to those calculated using the power-law constants above

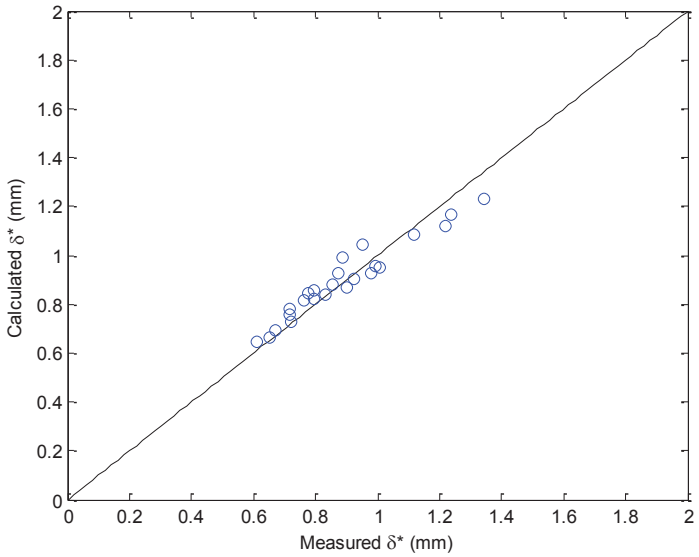

Figure 2.10. Comparison of measured values of δ^* to those calculated using the power-law constants above

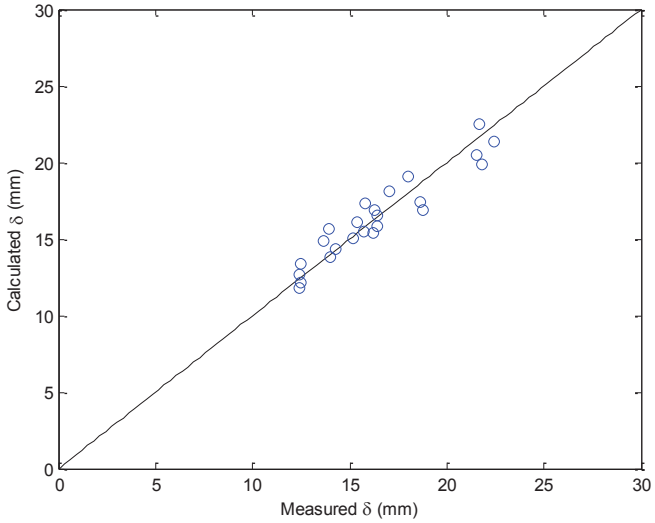

Figure 2.11. Comparison of measured values of δ to those calculated using the power-law constants above

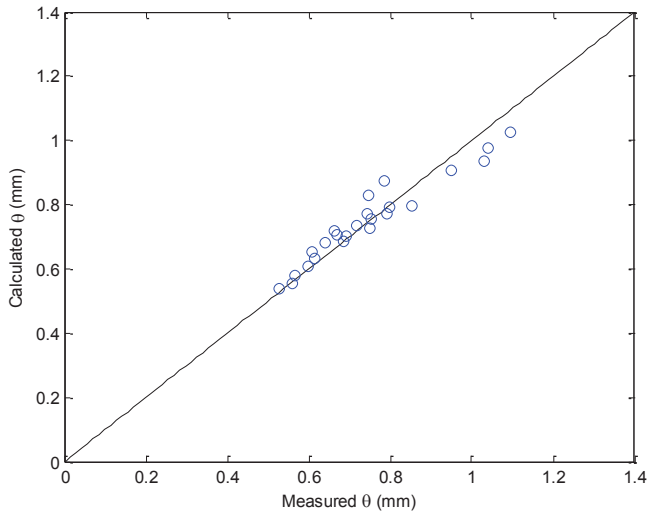

Figure 2.12. Comparison of measured values of θ to those calculated using the power-law constants above

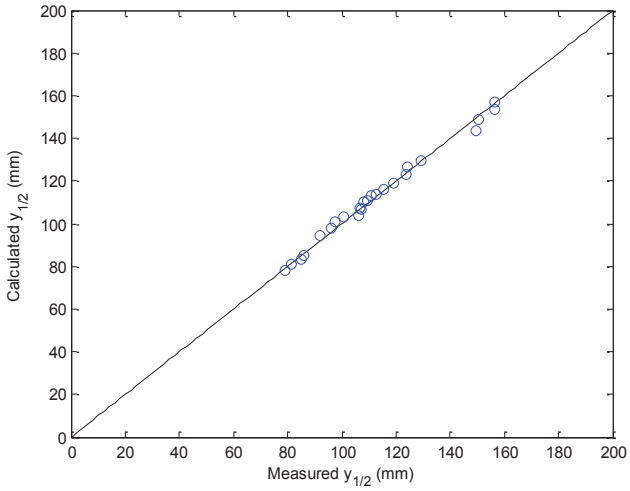

Figure 2.13. Comparison of measured values of $y_{1/2}$ to those calculated using the power-law constants above

2.4 Microphone Instrumentation

As mentioned above, far-field microphones were placed above the plate, outside of the flow. These microphones were Bruel and Kjaer type 4190 ½" diameter microphones with a flat-frequency response up to 20kHz. Bruel and Kjaer UA-1317 microphone holders were attached to a horizontal, streamwise-oriented beam approximately 0.8 m above the plate which extended from a support structure at the same height. The support structure was attached to rails on either side of the flat plate, and was therefore placed well outside the flow region. The support structure and beam were covered with flat acoustic foam to reduce the acoustic scattering from these elements, but the holders were left exposed.

Sennheiser KE4-211 pinhole electret microphones were used to measure surface pressure fluctuations and were mounted flush with the plate or flat surface. This was accomplished by placing a flat object over each microphone hole on the top surface of the plate and then inserting the microphone into the plate from below. Once contact was made with the flat object above, the microphone was secured in place using tape. Even using this method, however, some uncertainty was nonetheless observed for the placement of these microphones up to ± 0.5 mm.

The pinholes on these microphones were manufactured to be 1mm in diameter. However, this would lead to spatial averaging of the smallest turbulent structures which would result in decreased response at high-frequencies. This effect was investigated by Devenport et al (2011), and their results showed that a pinhole diameter of 0.5 mm was sufficient to eliminate any spatial averaging effects for the facility used in this investigation. Therefore, brass 1/2mm pinhole coverings were epoxied in place over the standard face of the microphone (Figure 2.14). This eliminated any problems associated with spatial averaging, but altered the frequency response. As such, it was necessary to calibrate each microphone before using them.

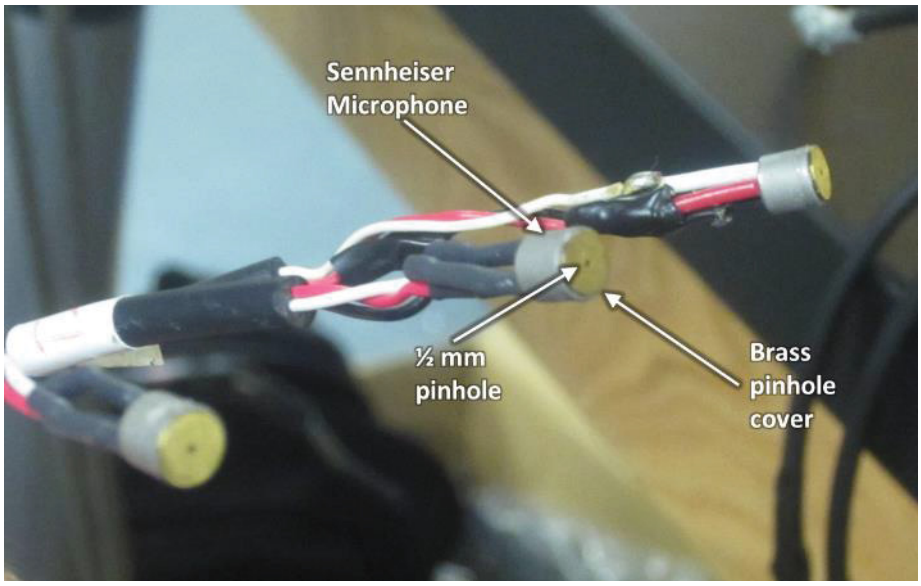

Figure 2.14. Photographic view of the Sennheiser surface pressure microphones featuring attached brass ½ mm pinhole covers

The unmodified Sennheisers had a nominally flat frequency response up to 10 kHz, but the modified microphone (with the ½ mm pinhole covering) would feature a resonance peak at some frequency near or below 10 kHz followed by a rapid decrease in sensitivity at higher frequencies. The phase response of the microphone would also be affected by the modifications, with the largest phase shift in the vicinity of the resonance peak.

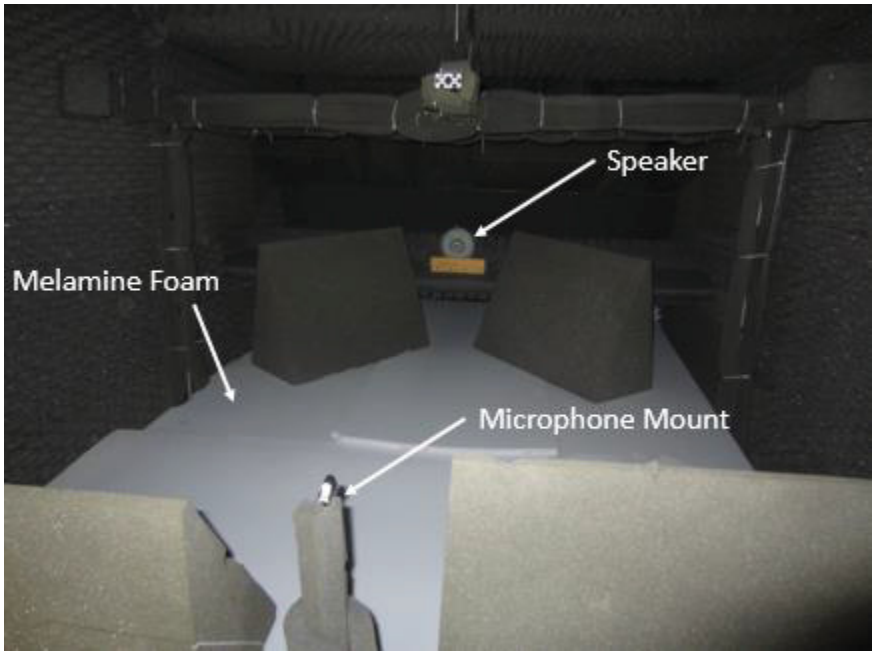

Figure 2.15. Photographic view of the microphone calibration setup in the test section of the Wall-Jet Tunnel

In order to record the characteristics of the new microphones, a University Sound model ID60C8 speaker was mounted on top of the acoustic shelf in the Wall-Jet Tunnel, and flat panels of 25.4mm thick melamine acoustic foam were placed over the plate. A mount was placed 2.045

m from the speaker, and a microphone bushing was attached to the mount. This arrangement is seen in Figure 2.15. A laser pointer aimed through the bushing verified that the center axis of the microphone bushing was aligned with the center of the speaker.

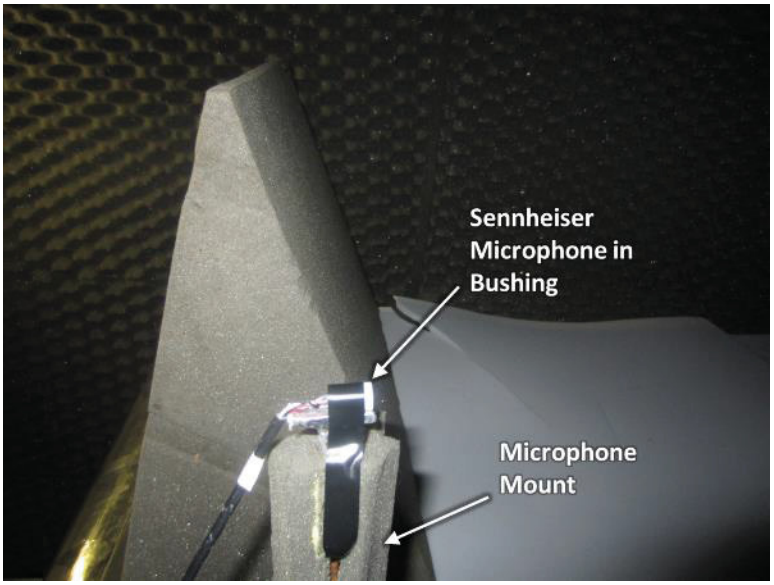

Figure 2.16. Photographic view of a Sennheiser microphone held in a bushing mounted in the test section of the Wall-Jet Tunnel, as part of the microphone calibration setup

A B&K type 4138 1/8th inch diameter microphone with a standard salt-and-pepper cap was first mounted as a reference microphone to calibrate the output of the speaker. This microphone has a flat frequency response up to 25.6 kHz. The sensitivity of this microphone was measured beforehand using a B&K type 4228 Pistonphone with output at 250 Hz, and was found to 0.51 mV/Pa. The speaker was driven by an Agilent VXI system generating white noise. Once the speaker was calibrated, the B&K microphone was removed and the Sennheiser to be calibrated was placed in the bushing on the microphone stand (Figure 2.16). Data from both the B&K and Sennheiser microphones were recorded using the same Agilent system used to drive the speaker. In this way, the microphone calibration function $C(f)$ could be obtained using the following formulas:

$$C(f) = \frac{G_{v_m v_s}(f)}{|G_{v_s v_s}|^2 M(f)} \tag{2.8}$$

$$M(f) = \frac{G_{p_r v_s}(f)}{|G_{v_s v_s}|^2} \tag{2.9}$$

In these equations, the spectral density function $G_{xy}(f)$, in terms of generic sources x and y is defined as:

$$G_{xy}(f) = \frac{2}{T} E[X(f)^* Y(f)] \tag{2.10}$$

In these equations, v_m denotes the voltage from the microphone to be calibrated, v_s denotes the voltage input to the speaker, p_r is the pressure record from the reference microphone, T is the total record length, and E denotes the expected value of the term in brackets. In words, the cross-spectra of the signal from the 1/8th inch microphone and the signal sent to the speaker is divided by the autospectra squared of the signal sent to the speaker and the sensitivity of the 1/8th inch microphone. This yields the speaker calibration. The cross-spectra of the signal from the Sennheiser microphone and the signal sent to the speaker is divided by the autospectra squared of the signal sent to the speaker and the speaker calibration. This yields the Sennheiser microphone calibration.

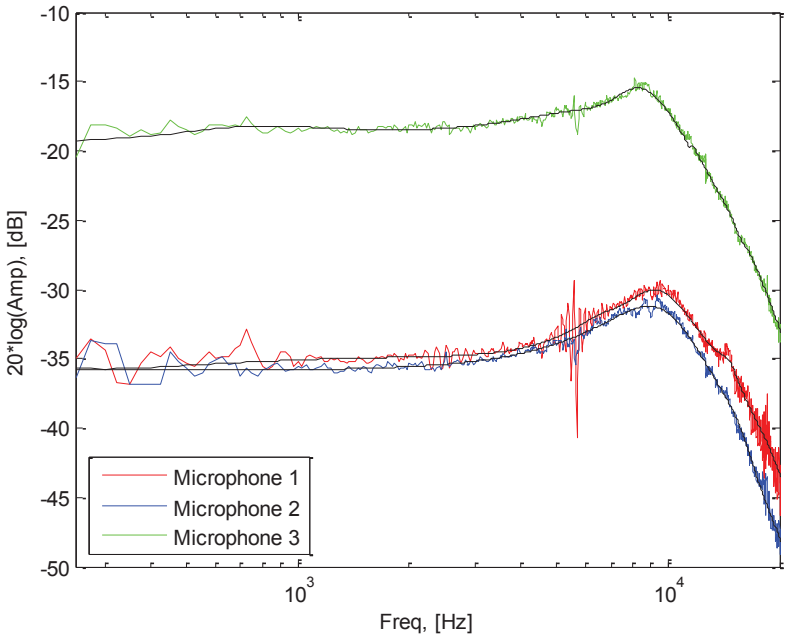

Figure 2.17. Amplitude calibration curves featuring the raw data for the three microphones (see legend) along with the smoothed calibration curves (black lines)

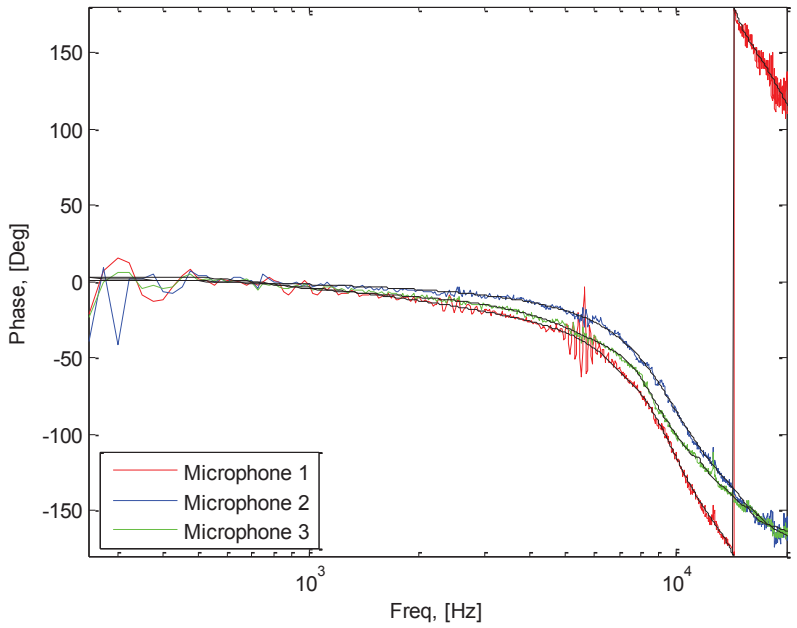

Figure 2.18. Phase calibration curves featuring the raw data for the three microphones (see legend) along with the smoothed calibration curves (black lines)

Calibration data was obtained for three Sennheiser microphones. Figure 2.17 shows the amplitude calibration data, which displays the resonance peak discussed above near 8-9 kHz for all three microphones. Note that the "dB" scale used for this plot does not feature any normalization (such as a reference pressure), and only refers to the logarithm function used to condition the data for plotting. The amplitude for microphone 3 can be seen to be offset by approximately 16 dB from the other microphones because this microphone was connected to a signal amplifier with a higher built-in gain that that for the other two microphones. The calibrations account for this difference such that any results from the microphones will be normalized properly. Figure 2.18 shows the phase calibration data obtained for the three microphones, and a reversal of phase is observed for all three microphones in the frequency range of the resonance peak observed in Figure 2.17, as expected. To eliminate noise in the calibration data, the calibration data were smoothed using a curve-fit algorithm. The curve-fit was accomplished by first disregarding any widely-scattered data in the low frequency range (as seen in Figure 2.17 and Figure 2.18). A Laplace-transformed transfer function was then chosen such that the error between the fit and data was minimized, while simultaneously ensuring that, at low-frequencies, the fit flat-lined to the nominal value seen in the data for amplitude, as well as zero degrees of phase. The transfer function was of the form:

$$H(s) = \frac{B(s)}{A(s)} = \frac{b_1 s^{nb-1} + b_2 s^{nb-2} + \cdots + b_{nb}}{a_1 s^{na-1} + a_2 s^{na-2} + \cdots + a_{na}} \tag{2.11}$$

The results of the curve-fit are also plotted in Figure 2.17 and Figure 2.18 as the black lines, and are observed to adequately follow the measured data across all frequency ranges. The curve-fit calibration functions could then be applied directly to any data taken by the formula:

$$\Phi_{p_i p_j}(f) = \frac{E[V_i^*(f)V_j(f)]}{C_i^*(f)C_j(f)} \tag{2.12}$$

Here, the indices i and j refer to individual microphones, E denotes the expected value of the function in brackets, V is the pure voltage signal obtained during an experimental measurement, and C is the calibration function obtained above.

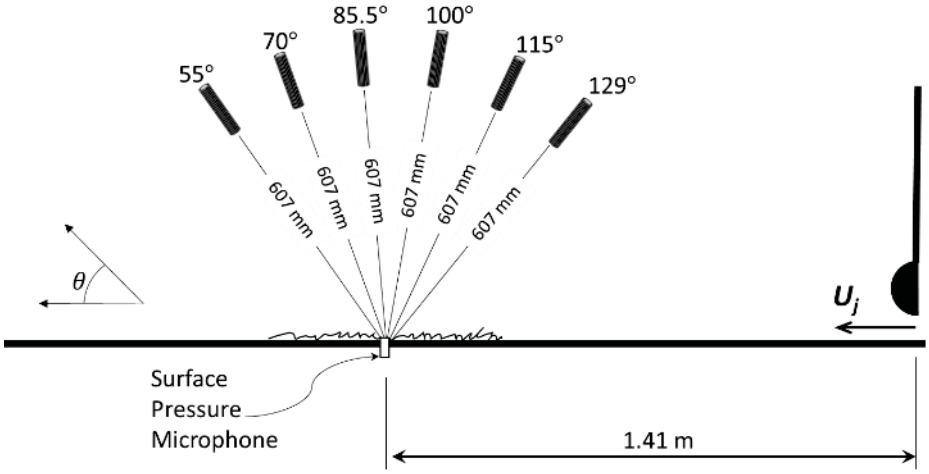

Figure 2.19. Schematic view of microphone configuration A.

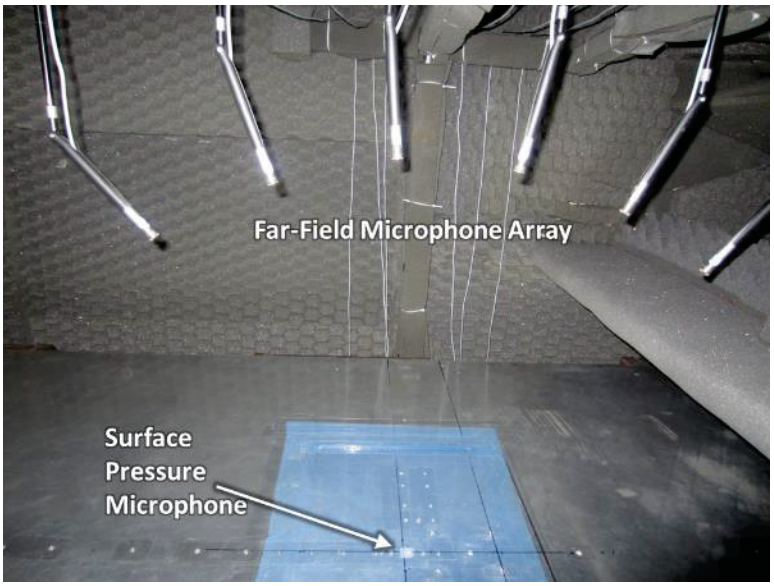

Figure 2.20. Photographic view of microphone configuration A with a fabric canopy installed

Two configurations of microphones were used to test two different types of canopies to be discussed later. The first configuration (configuration A), shown schematically in Figure 2.19, featured six far-field microphones arranged in a circular arc with a radius of 607 mm. This configuration was used while testing fabric canopies (see Section 2.6). The microphones were focused at a spanwise-centered point on the wall-jet plate 1.41 m downstream of the nozzle exit. These microphones were oriented at 55, 70, 85.5, 100, 115, and 129 degrees relative to the downstream direction. In addition, one surface pressure microphone was placed at the focus point

of the circular array, 1.41 m downstream of the nozzle. This arrangement as it was set up in the wind tunnel is shown in Figure 2.20.

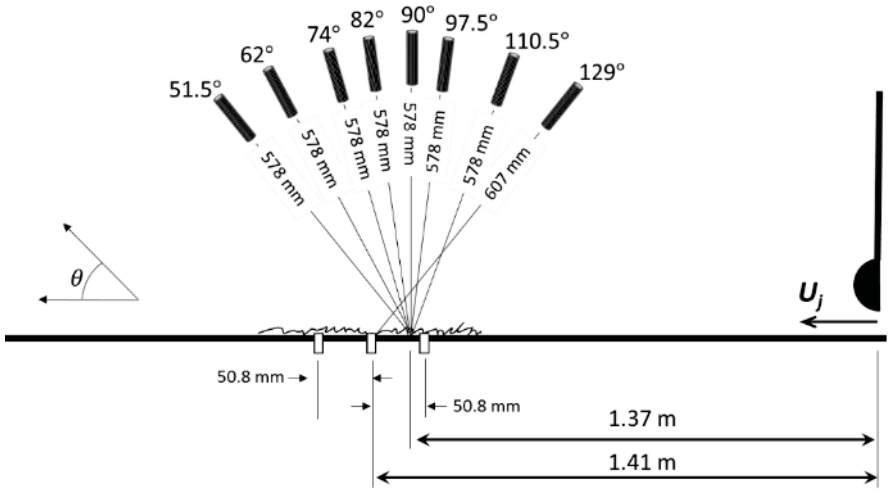

Figure 2.21. Schematic view of microphone configuration B.

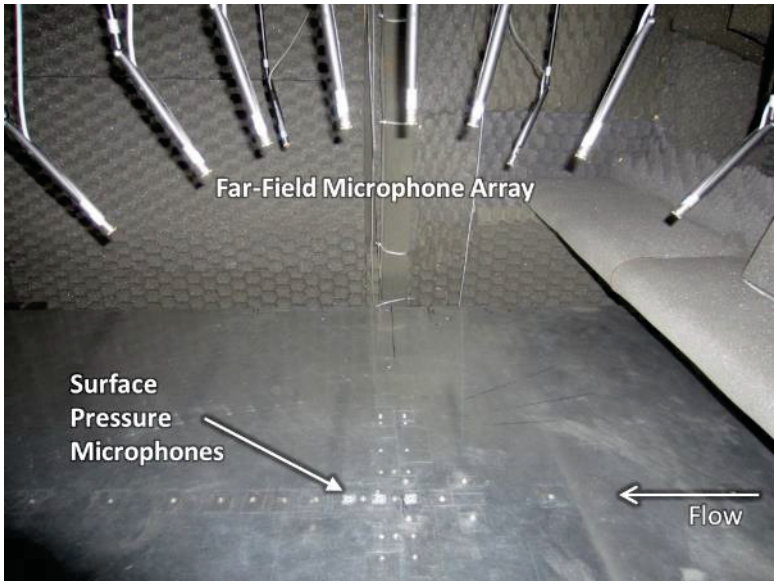

Figure 2.22. Photographic view of microphone configuration B with a clean surface

The second configuration (configuration B), shown schematically in Figure 2.21, featured eight far-field microphones arranged in a loose arc above the wall-jet plate. This configuration was used while testing unidirectional canopies (see Section 2.7). The placement of the most upstream microphone (oriented 129 degrees relative to the upstream direction) was matched to that of the most upstream microphone of configuration A. This microphone was directed at a point 1.41 m downstream of the nozzle exit. Seven other microphones were placed in a spanwise-centered circular arc. However, this arc was focused at a point 1.37 m downstream of the nozzle exit and had a radius of 578 mm. The microphones were oriented at 51.5, 62, 74, 82, 90, 97.5, and 110.5 degrees relative to the downstream direction. For this configuration, three surface pressure microphones were placed in a spanwise centered array. The center microphone in the array was placed at the same location as the one surface pressure microphone in configuration A. The other

two microphones were placed 50.8 mm directly upstream and downstream of this center microphone. This arrangement as it was set up in the tunnel is depicted in Figure 2.22.

The radius and angle of inclination of each microphone were measured and set using a metal t-square and digital inclinometer. The uncertainty of the radial measurement was ± 4 mm, while that of the angular measurement is ± 1 degree.

For all measurements, far-field sound and surface pressure fluctuations were measured simultaneously. The far-field microphones were high-pass filtered above 22.4 Hz, while the surface pressure microphones were high-pass filtered above 0.7 Hz. All microphones were sampled at 65536 Hz for 32 seconds. This data was broken into records of 2048 samples, and frequency spectra were obtained by averaging the Fast-Fourier Transform of each record utilizing a Hanning window with a 50% overlap. The resulting spectra were normalized on a reference pressure, p_{ref}, of $20E$-6 Pa and plotted on a decibel scale using the following formula.

$$SPL = 20log_{10}(p_{rms}/p_{ref}) \tag{2.13}$$

Here, SPL denotes the Sound Pressure Level in decibels (dB) and p_{rms} is the root-mean-square of the sound pressure calculated for a given frequency. Considering the microphone set-up, sampling techniques, and processing methods, the uncertainty in the far-field microphones is assumed to be ± 1 dB, while that for the surface pressure microphones is assumed to be ± 2 dB to account for increased uncertainty in their vertical position in the wall.

2.5 Rough Surfaces

Three rough surfaces were tested. All were positioned symmetrically with respect to the wall-jet plate centerline, and were centered at a streamwise location of 1410mm. The first two surfaces, a hemispherical roughness fetch and a sandpaper roughness fetch, were mounted directly on the wall jet plate. The hemispherical roughness, pictured in Figure 2.23, extended 300mm in the streamwise direction and 600mm in the spanwise direction, and consisted of 3mm hemispheres spaced 16.5-mm center to center in a square array. This surface was identical to that tested previously, as part of roughness noise studies, by Alexander (2011). The surface pressure microphone used with this surface was placed at the center of the roughness fetch, at a location centered in the square area between four roughness elements. The second surface, pictured in Figure 2.24, was formed by a sheet of 20-grit sandpaper roughness extending 200 mm streamwise and 600 mm spanwise. This type of surface, tested previously by Devenport *et al.* (2011), has a nominal grain size of 0.95mm, a grain density of 0.23 grains/mm^2, and an RMS roughness height of 0.206mm. The edges of these roughness patches were taped and faired to the surrounding wall using 0.1mm thick aluminum tape. Devenport *et al.* (2011) demonstrated that, with this arrangement, the perimeter of the roughness substrate and the tape produces no detectable noise.

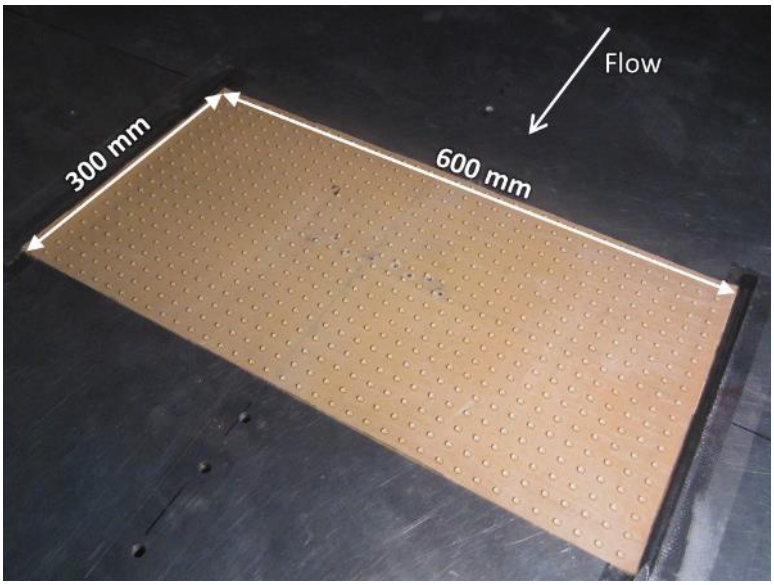

Figure 2.23. Photographic view of the rough surface featuring a grid of evenly spaced 3mm hemispheres

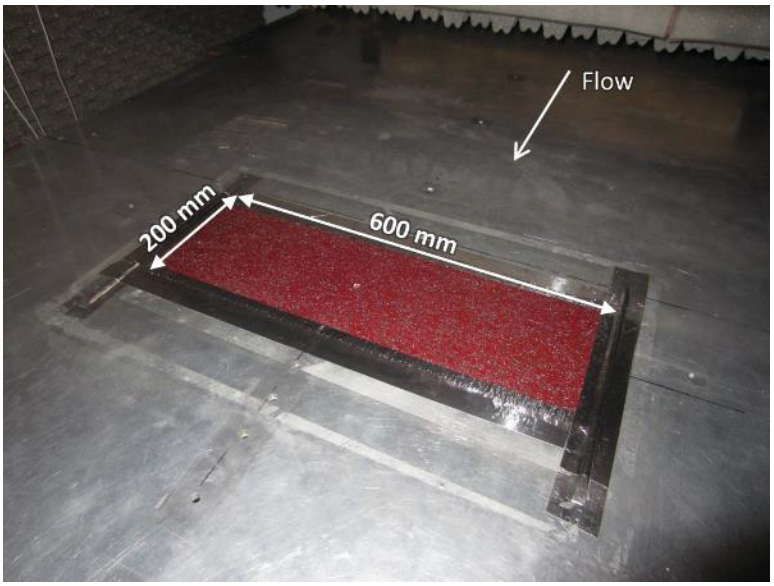

Figure 2.24. Photographic view of the sandpaper-type rough surface

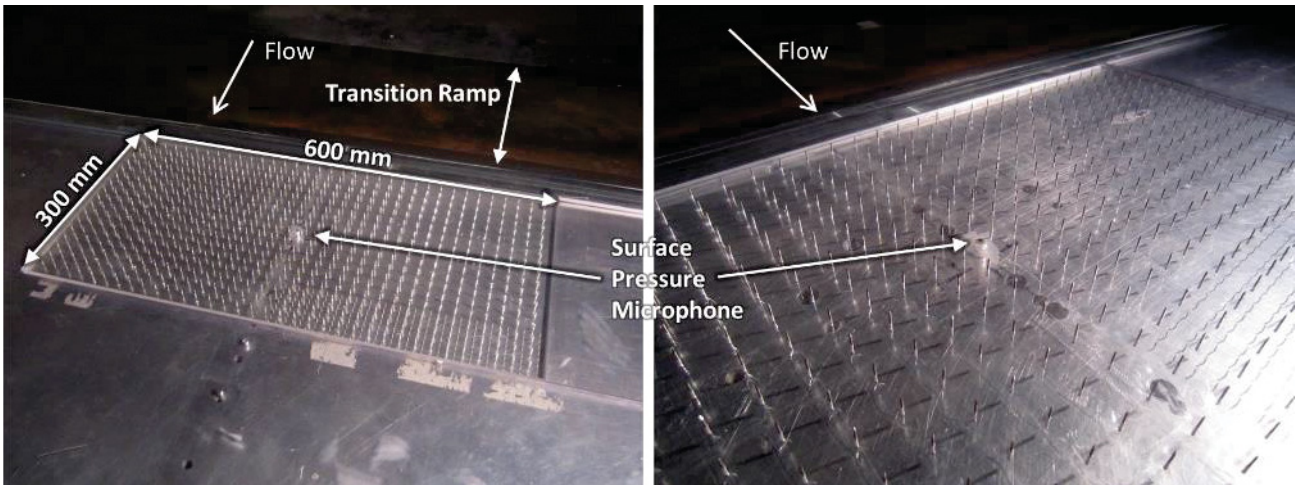

Figure 2.25. Photographic view of the rough surface featuring a grid of evenly spaced 6.4 mm high needles

The third rough surface tested, designed to mimic the lower layer of the owl down where the hairs are almost perpendicular to the feather surface, consisted of a 300mm by 600mm array of vertical needles arranged in a square array with a 16.5mm center to center distance, as seen in Figure 2.25. The needles protruded 6.4mm above the surface. As with the 3mm hemispherical roughness, the surface pressure microphone used for this surface was placed in the center of the square area formed by four elements (needles). This surface was constructed of 12.7mm long needles mounted from underneath through tight-fitting holes laser-cut into a 6.4mm thick acrylic sheet. The needles were cylindrical of 0.48 mm radius with the exception of the top 1.8mm which consisted of a 4-sided bevel to a sharp tip. The 6.4mm thick substrate for this configuration prevented mounting directly on the wall-jet plate, as for the other surfaces. Instead a shaped metal transition, 305mm in length, was used to smoothly elevate the wall-jet 12.7mm above the base plate (Figure 2.26). The transition, used previously by Awasthi *et al.* (2013), had the shape of a shallow inflection. The 0.7mm high forward step at the leading edge of the transition was faired using 0.1mm thick metal tape to eliminate it as a noise source and to minimize its flow disturbance. The 12.7mm elevation of the flow surface allowed the needle bed roughness to be mounted with its substrate flush with the surrounding wall or, for configurations including a fabric canopy, recessed 6.4mm below it as illustrated in Figure 2.26.

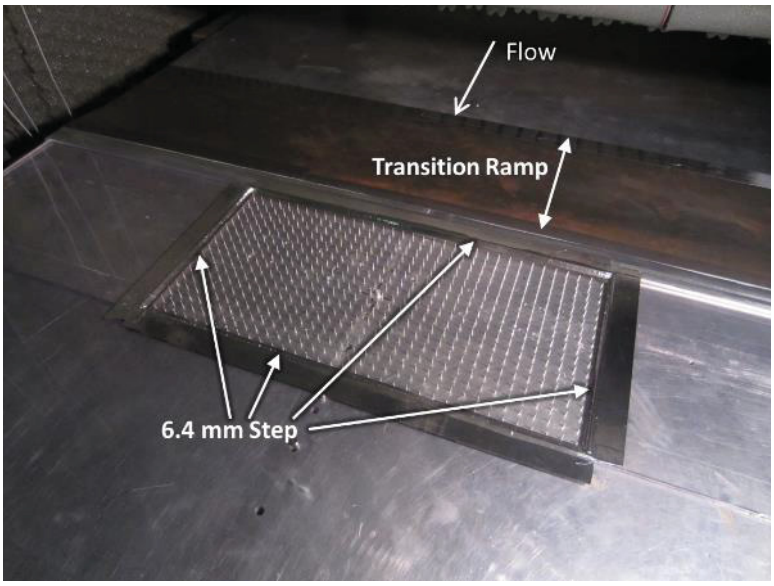

Figure 2.26. Photographic view of the rough surface featuring a grid of evenly spaced 6.4 mm high needles, mounted such that the tops of the needles were at a height equal to that of the surrounding surface

2.6 Fabric Canopies

Following the idea that the owl-feather downy coating could be idealized as a canopy suspended above the surface, five mesh-like polyester or nylon fabrics were used to simulate the canopy. The fabrics were selected based on qualitative similarity to the structure of the owl's downy coating (high open area ratio, interlocking fibers). Pictures of the fabrics are shown in Figure 2.27.

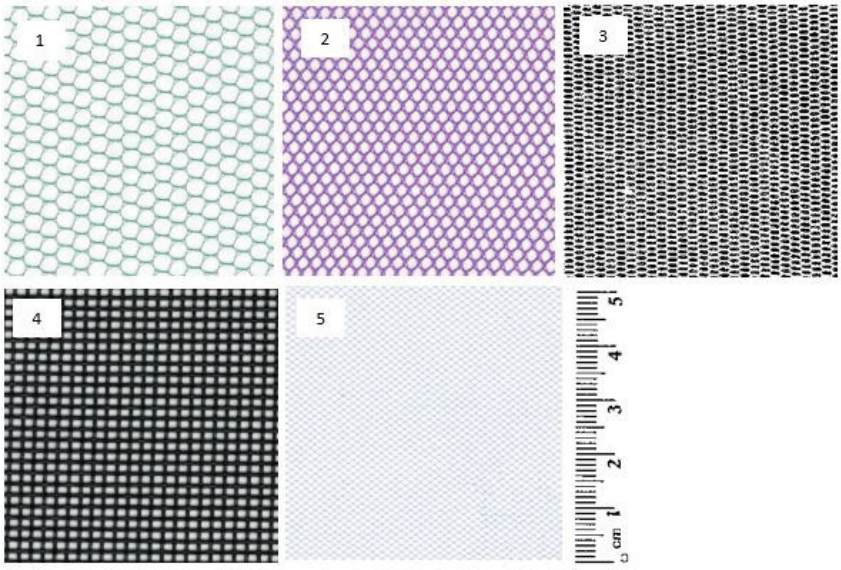

Figure 2.27. Scanned images of samples of each fabric canopy along with a scale applicable to all images

The fabrics chosen were all a type of mesh with a range of pore sizes, thread diameters, and open area percentages. In addition to the length dimensions, the fabrics all featured different elastic properties dependent on several factors including the arrangement of the fibers in the mesh, the winding of individual strands into threads, the diameter of the threads, and the material. The measurable characteristics of the fabrics are given in Table 3.

Table 3. Measured and observable characteristics of all fabric canopies

Fabric no.	Material	Open area	Pore diameter	Thread diameter	Effective tension modulus	Special characteristics
1	Nylon	75%	3.9mm	0.3mm	508 N/m	
2	Nylon	64%	3.1mm	0.4mm	555 N/m	
3	Nylon	76%	2.1mm	0.2mm	1320/18 N/m	Highly anisotropic weave
4	Polyester	38%	2.3mm	0.7mm	7930 N/m	
5	Nylon	70%	1.6mm	0.06mm	117 N/m	Weave is diagonal to fabric edges

In terms of filament size and open area ratio fabric 5 most closely simulates the owl-down canopy, but even with this finest fabric the thread diameter is about three times the estimated diameter of the owl's hairs. As seen in Figure 2.27, the fabrics were not isotropic, but some displayed similarities when rotated. All fabrics were tested with the vertical direction in Figure 2.27 aligned with the flow direction, thus placing a significant fraction of the fibers perpendicular to the flow direction for fabrics 1, 3 and 4, but with most of the fibers at 45° to the flow for fabrics 2 and 5.

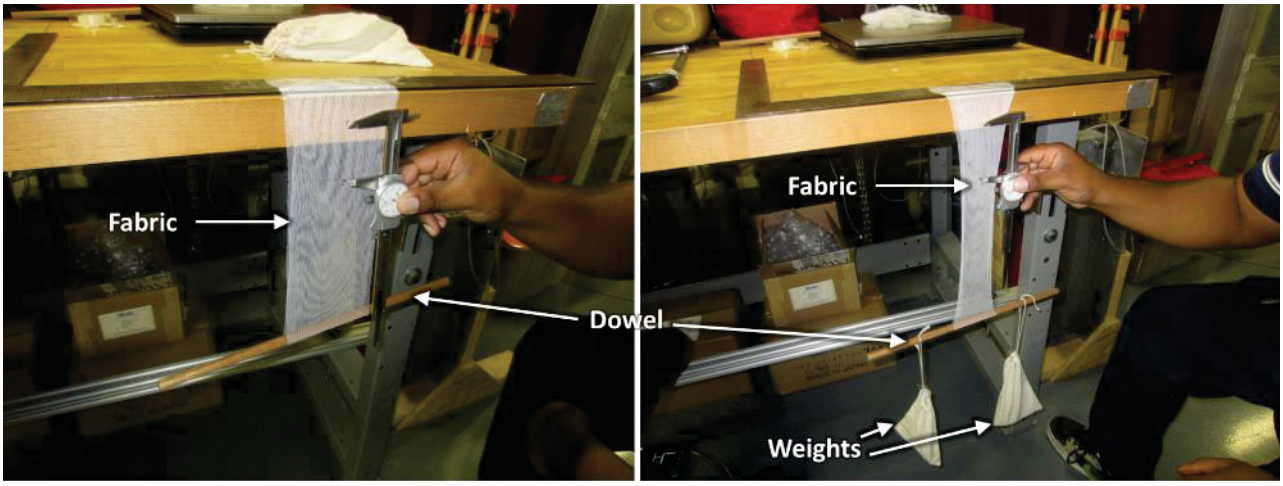

Figure 2.28. Photographs depicting the modulus testing of fabric 3. The image on the left shows the fabric with only the dowel placed in the fabric loop, while the image on the right shows the fabric after the weights have been attached to the dowel

Tension in the fabric was a possible factor in the performance of the canopy, as it affected both the orientation of the fibers comprising the fabric and the effective flexibility of the fibers. As such, the tension in the fabric would need to be measured after it was placed in the tunnel. Since measuring tension directly is difficult, it was decided to measure the stretch of the fabric after it was placed, and relate this back to tension through an effective modulus. Therefore, before

the fabrics were placed in the wind tunnel, an attempt was made to measure the elastic modulus of the fabrics. To accomplish this, a sample was taken from each fabric and folded over. The two loose ends were attached to a lab bench, forming a loop of fabric hanging down from the lab bench. The fabric was marked at two places, and the distance between the marks was measured. Then, a dowel was inserted into the loop, and weights were added to the dowel. The distance between the marks was measured again. This arrangement is seen in Figure 2.28 for fabric 3. Finally, by comparing the two distances with and without the weight added to the fabric, and accounting for the dimensions of the fabric itself, an effective modulus could be calculated, as given in Table 3. Similar marks were made for the fabric placed in the tunnel, and distances were measured in a similar manner in both the streamwise and spanwise directions for later calculations of the tension in the fabrics during the experiment.

For the smooth-wall, hemisphere and sandpaper-roughness conditions the fabric canopies were suspended above the surface by using two tapered half-round dowels mounted on either side of the test area, as shown in Figure 2.29 and Figure 2.30. The dowels effectively created 4-mm high ridges running down either side of the test area. Draping the fabrics over these dowels, tensioning the fabric spanwise and then taping the fabrics to the flow surface outside of the test area enabled a measure of control of the fabric height.

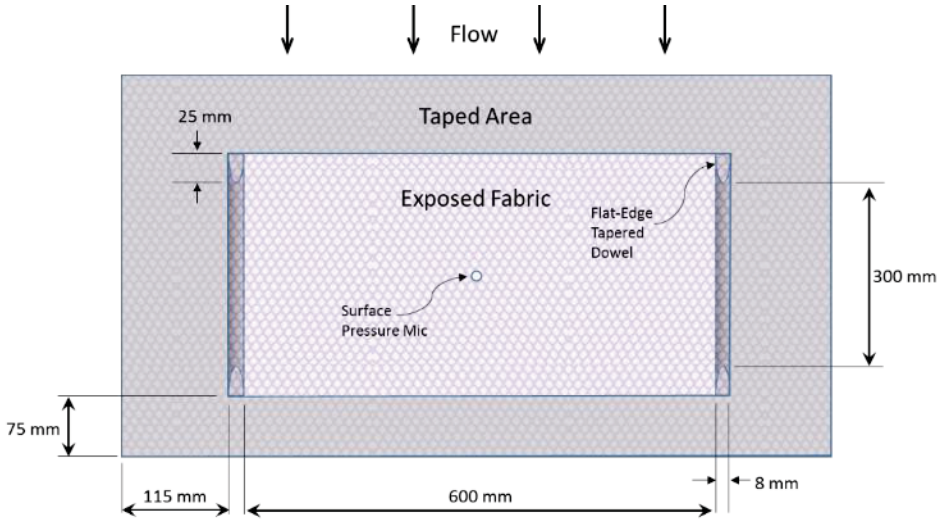

Figure 2.29. Schematic overhead view of the overall test apparatus featuring fabric, support dowels, and taped edges

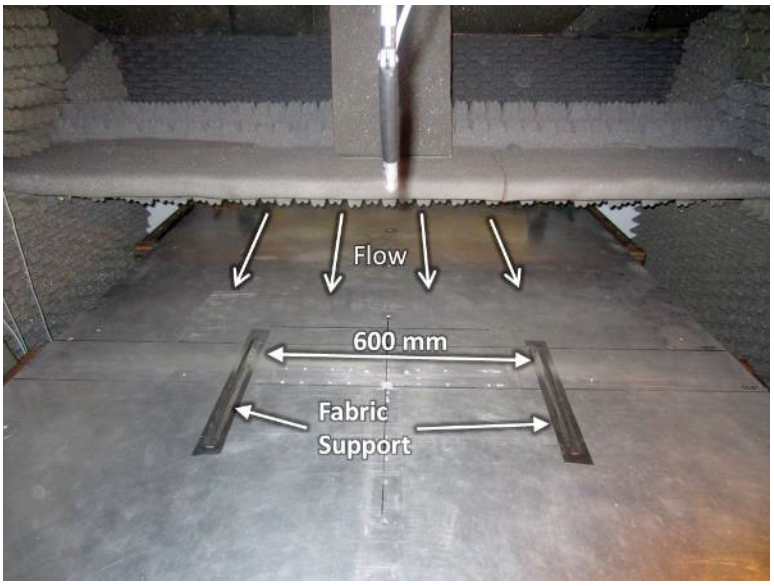

Figure 2.30. Photographic view of the fabric support dowels mounted on the test plate in the Wall-Jet Tunnel

For the needle-bed roughness, as discussed above, the rough surface itself was recessed 6.4-mm below the surrounding flow surface in order to provide the necessary elevation of the fabric canopies, as seen in Figure 2.31 and Figure 2.32. The steps generated around the perimeter of the rough surface were rounded using quarter-round dowels – an arrangement that did not significantly change the roughness noise generated by this surface, or the pressure fluctuations at its center, in the absence of a canopy covering (see Chapter 3).

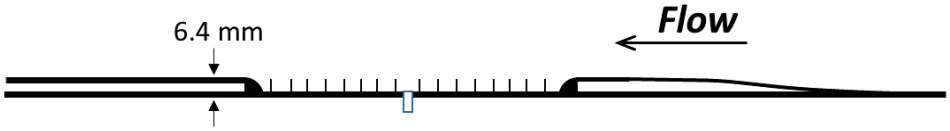

Figure 2.31. Schematic side view of the upstream transition ramp and recessed needle bed featuring quarter-round dowels at the edges of the bed

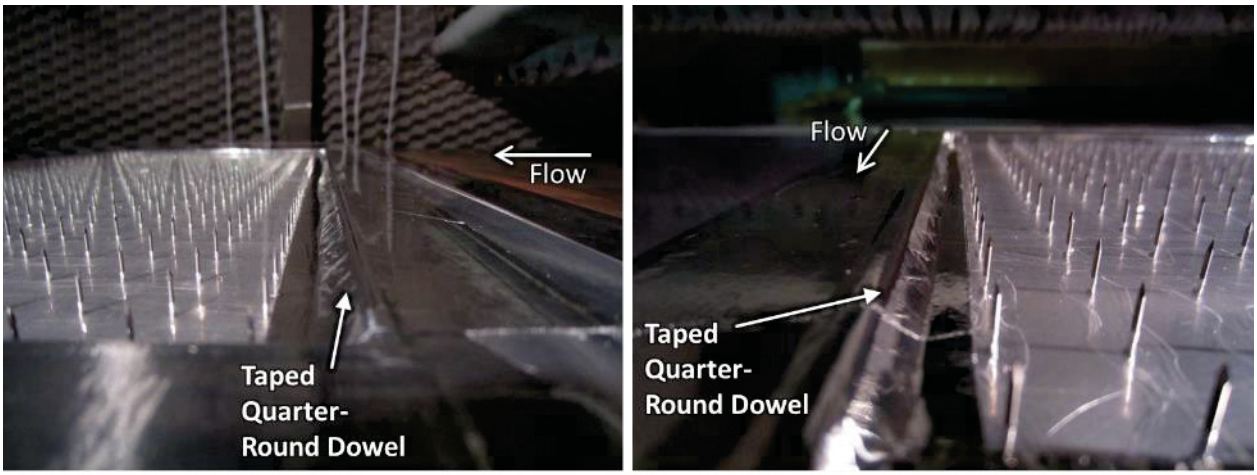

Figure 2.32. Photographic view of the taped quarter-round dowels on the upstream (a) and spanwise (b) edges of the recessed needle bed

During placement of the fabrics wrinkles tended to form in the fabric. A specific procedure was used in order to minimize wrinkles and to yield a smooth, uniform fetch of fabric suspended above the surface. First, double-sided tape was placed around the perimeter of the test area. Next, the fabric was held suspended as one side of the fabric was placed on the double-sided tape next to one dowel. The fabric was then stretched taut and placed on the double-sided tape next to the other dowel as the upstream and downstream edges of the fabric naturally fell on the upstream and downstream double-sided tape. At this point, the fabric was taut in the spanwise direction, but was usually very wavy or wrinkled in the streamwise direction. The fabric was detached from the upstream and downstream edges and pulled taut to eliminate these wrinkles. As the fabric was cut larger than necessary to make this process easier, it was necessary to cover any excess fabric with clear tape. An example configuration is shown in Figure 2.33 and Figure 2.34. Once this process was completed, the fabric strain in the streamwise and spanwise directions could be measured.

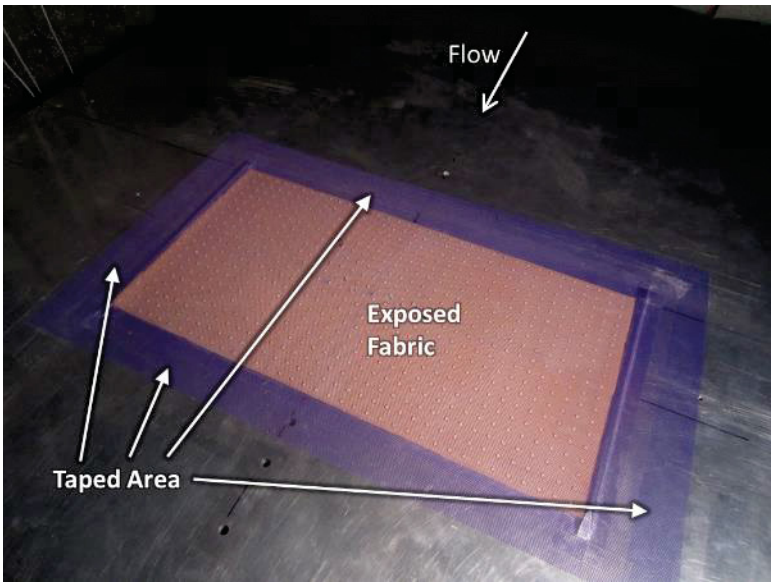

Figure 2.33. Photographic overall view of fabric 2 in place over 3mm hemispherical roughness

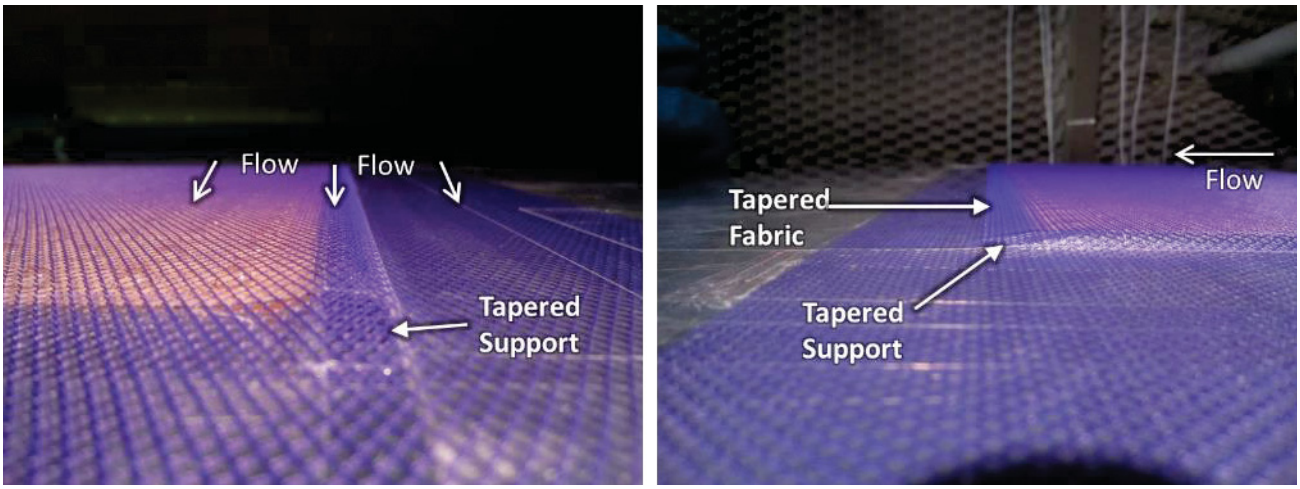

Figure 2.34. Photographic close-up views of fabric 2, emphasizing the taped fabric edges and tapered dowels

Precise placement of flexible surfaces, like the fabrics used here, is quite difficult and this resulted in a range of positions for each configuration. Despite the tension present in the fabrics, the fabrics had a tendency to sag near the center of the fetch. This sag was considered to be unavoidable considering the relatively large distance (600 mm) between the fabric supports. However, the presence of roughness beneath the canopies tended to lend some support to the canopy and relieve some of the sag. As such, the true canopy heights at the center of the fetch and at the supports were measured for each fabric with each rough surface. With the fabrics mounted using the dowels above the smooth wall, the canopy was placed 2.0±0.5mm above the wall at its center and 4mm above at the edges adjacent to the dowels. For the 3mm hemispheres (using dowels) the canopy height was 3.5±0.5mm at the center and 4mm at the dowels. For the sandpaper roughness, the canopy height was 2.5±0.5mm at the center and 4mm at the dowels, and for the needle bed the height was 6±0.5 mm at the center and 6.4mm at the streamwise and spanwise edges of the fetch.

The tension in each fabric was roughly constant across all rough surfaces, and was calculated using the measured strain in the fabric for each run, as described above. Precise values for the tension are unavailable because the fabrics were placed under a combined state of spanwise and streamwise tension, and the effect of this combination with respect to the strain in each direction was not well-characterized. However, approximate values can be obtained by assuming that the streamwise tension was sufficiently less than the spanwise tension, such that only the spanwise strain measurement can be used for the calculation of spanwise tension. For fabrics 1, 2, and 3, the spanwise tension across the fabric was consistently about 5±2 N. For fabric 4, the spanwise tension was about 15±5 N due to its much higher effective modulus. Fabric 5 was consistently placed with spanwise tension of approximately 9±2 N. The influence of the tension on the shapes of the fabric pores was not directly measured. However, it was assumed that the shapes of the fabric pores would not be significantly altered from their unloaded shapes, based on the relatively low magnitudes of the tension, and the fact that at least some tension was applied in the streamwise direction which would combine with the higher spanwise tension to help restore the fabric's original shape.

2.7 Unidirectional Canopies

Unidirectional canopies, essentially fabric canopies with fibers only aligned with the flow direction, were also tested. These were comprised of fluorocarbon fishing line (forming the fibers) suspended from a pair of 3D-printed, smoothly curved, 6.4mm high and 63.5mm long supports placed at the upstream and downstream edges of the same sandpaper roughness used in the mesh canopy experiment. The supports were designed to be as aerodynamically neutral as possible to limit any disturbances in the flow, while still providing a feasible support structure for the fibers. The final printed support structures featured simple rounded edges at the spanwise ends. A profile view of the supports can be seen in Figure 2.35, the isolated supports can be seen in Figure 2.36, and a complete assembly with supports thread, and roughness is seen in Figure 2.37. In addition, configurations were tested which featured the supports and roughness, but no canopy (Figure 2.38), and the supports and canopy, but no roughness (Figure 2.39). The canopy without roughness was produced by removing the sandpaper from a fully assembled configuration, a method which resulted in leftover residue from the double-sided tape used to attach the sandpaper roughness. To smooth the surface beneath the canopy without completely reworking the canopy itself, 0.1mm thick aluminum tape was fed beneath the canopy and attached to the surface below.

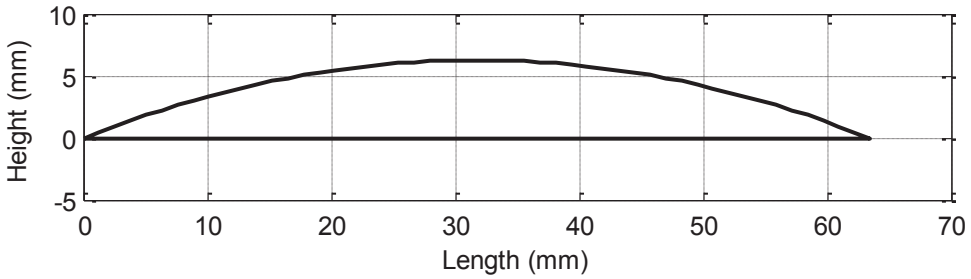

Figure 2.35. Profile of the unidirectional fiber support featured in the computer model used to 3D print the structure

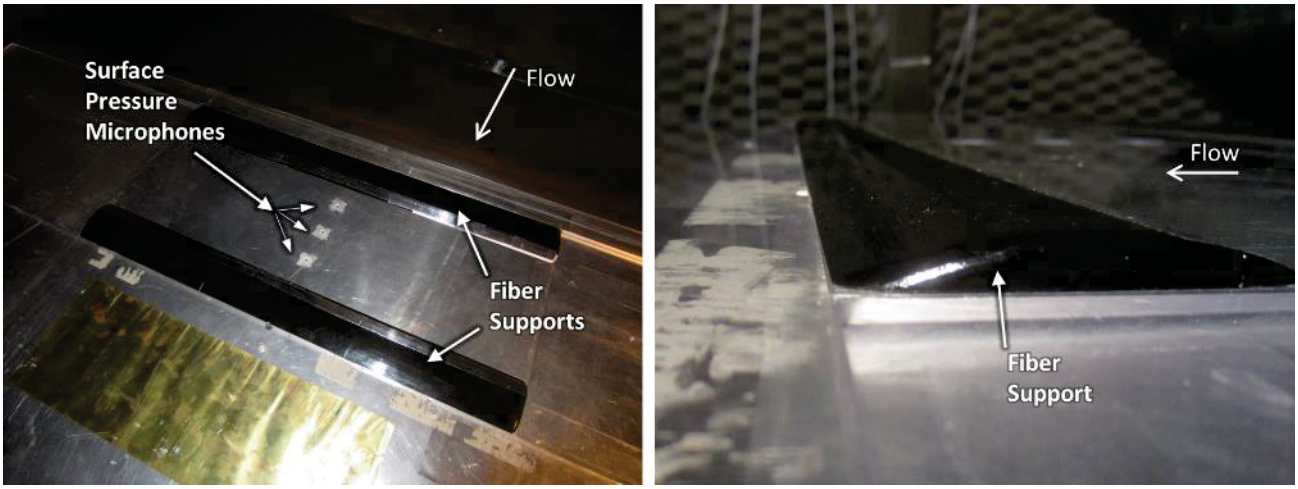

Figure 2.36. Photographic views of the fiber supports mounted in the Wall-Jet Tunnel

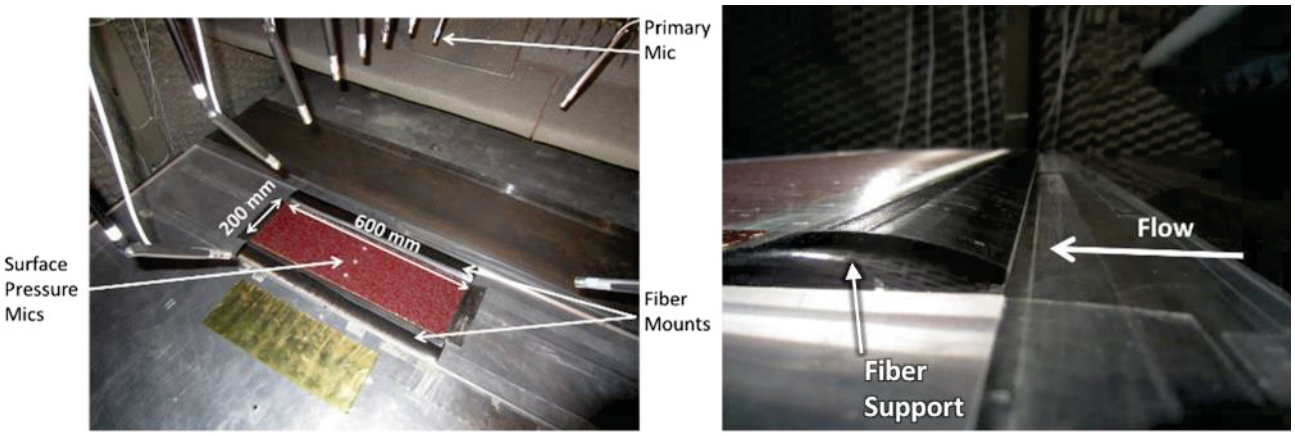

Figure 2.37. Photographic views of the unidirectional canopy setup with sandpaper roughness

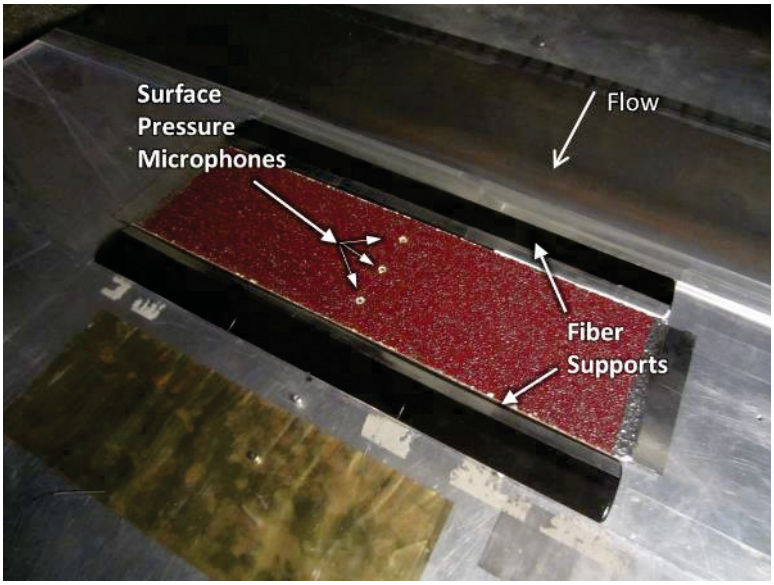

Figure 2.38. Photographic view of the sandpaper and fiber supports mounted in the Wall-Jet Tunnel without a canopy

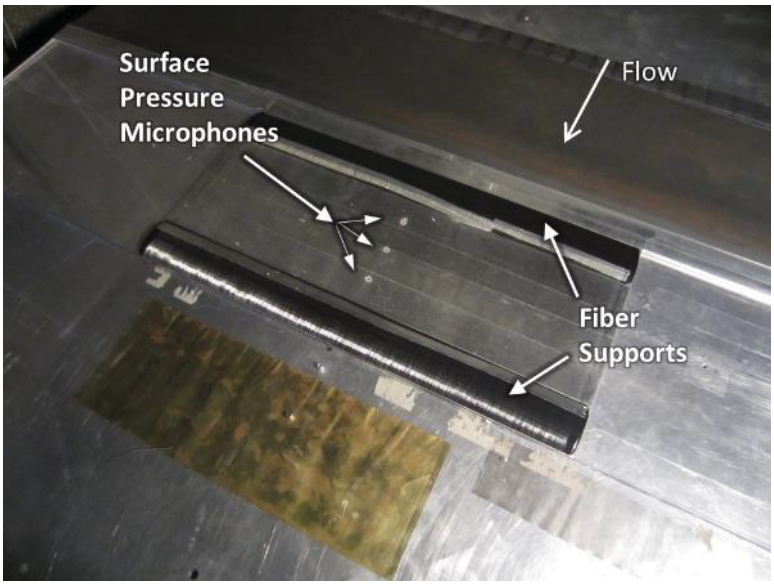

Figure 2.39. Photographic view of the fiber supports and canopy mounted in the Wall-Jet Tunnel with a smooth surface beneath the canopy

The thread supports were attached, using double-sided tape, to an aluminum plate featuring three holes corresponding to the locations of the surface pressure microphones in configuration B, and fishing line was wrapped around the entire plate and over the supports. Considering the dimensions of the support and location of the microphones, the most upstream microphone can be said to be at a location six support-heights downstream of the trailing edge of the support. When assembled in the wind tunnel this arrangement produced a surface flat and continuous with the surrounding wall, with the exception of the streamlined supports at the leading and trailing edges of the test-portion of the surface and the unidirectional canopy formed between them. The spanwise edges of the sandpaper roughness were faired with 0.1mm thick aluminum tape (Figure 2.40). Note that the unidirectional canopy configurations used the same slightly elevated flow surface and smooth transition used with the needle bed.

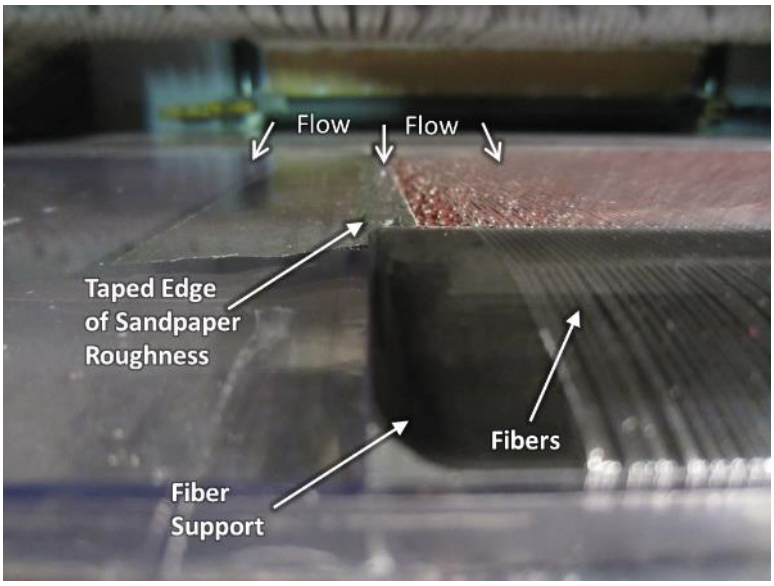

Figure 2.40. Photographic close-up view of the spanwise edge of the unidirectional canopy setup, emphasizing the fairing of the edges of the sandpaper with 0.1 mm thick aluminum tape

Three complete test surfaces were manufactured, each with a different fishing line diameter. Table 4 gives the relevant parameters of the three canopies. The top surfaces of the supports used with each test surface were manufactured with evenly-spaced grooves so as to precisely accommodate the fishing line fibers wound over them and to set the fiber spacing so as to produce an open area ratio of 70%. Figure 2.41 shows close-up views of each of the three canopies suspended above sandpaper roughness. Although the areas around each microphone appear somewhat deformed due to manufacturing, it was assumed that any roughness here would be far less than that present in the surrounding fetch. No inconsistencies in the measured pressure data were observed which could be attributed to the areas around the microphones.

Table 4. Physical characteristics of each unidirectional canopy

Canopy	Fiber Diameter (mm)	Spacing Between Fibers (mm)
1	0.28	1.02
2	0.56	1.82
3	0.91	3.05

The tension used to wrap the fishing line was intended to be kept constant at around 1-2 lbs using a fishing reel with a calibrated line drag setting. However, this proved more difficult than expected for the thickest fishing line, as the line would not stay wrapped on the reel. In this case, the thread was wrapped by hand while attempting to keep the tension in the fibers constant.

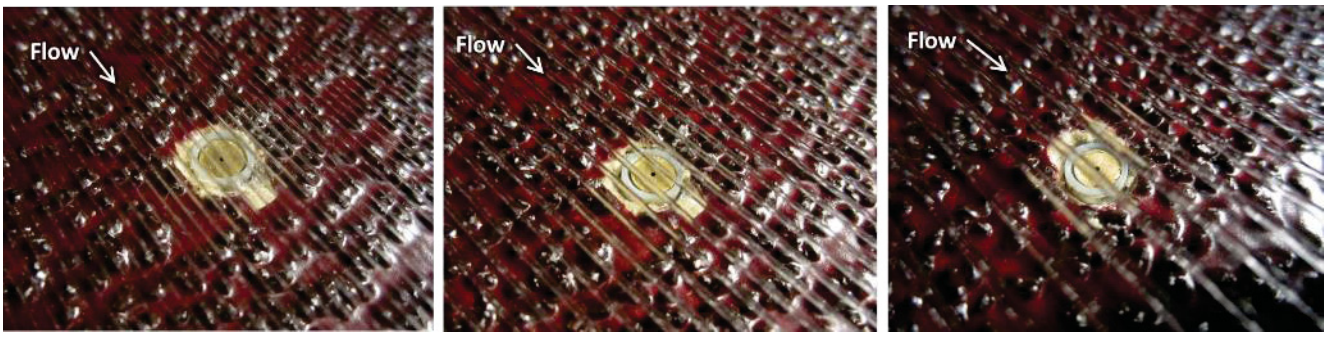

Figure 2.41. Photographic close-up views of each unidirectional canopy (1 (a), 2 (b), and 3 (c)) with surface pressure microphones for reference of scale

Chapter 3 – Results and Discussion

3.1 Validation of Fabric Canopy Mounts

In order to ensure the fabric canopy mounts (described in Section 2.6) had no detrimental effects on the far-field noise or surface pressure spectra in the Wall-Jet Tunnel, a comparison is first presented which displays the benign nature of the supports. Figure 3.1 and Figure 3.2 present far-field noise spectra and surface pressure fluctuation spectra, respectively, measured from the smooth wall and smooth wall with fabric supports. The far-field spectra can be seen to be virtually indistinguishable, meaning the fabric supports have almost no effect on the far-field noise. The surface pressure spectra display a slight increase in levels across all frequencies, but this difference is low enough to fall within the uncertainty of the measurements. Because there is no measureable difference between the smooth wall case and the case featuring the fabric supports, the term "smooth wall" will refer to the case with fabric supports for all data presented in Sections 3.2 through 3.8.

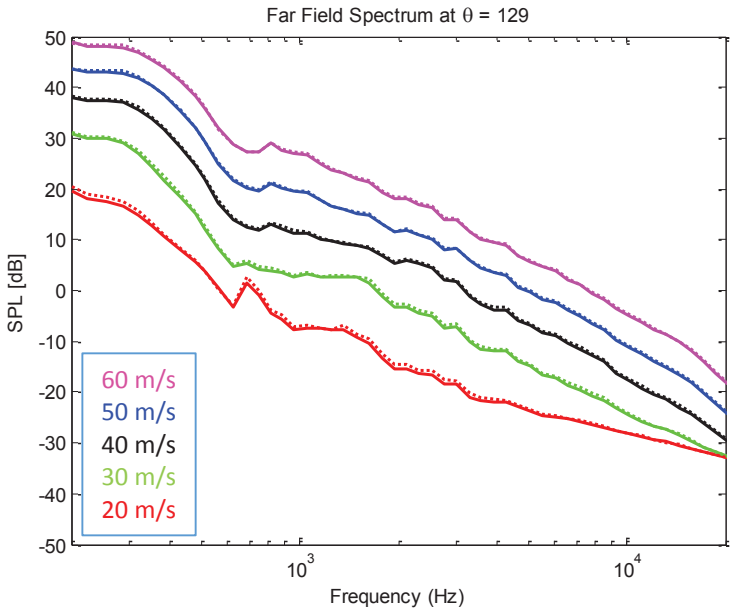

Figure 3.1 Comparison of far-field noise spectra for smooth wall (solid lines) and smooth wall with fabric mounts (dotted lines)

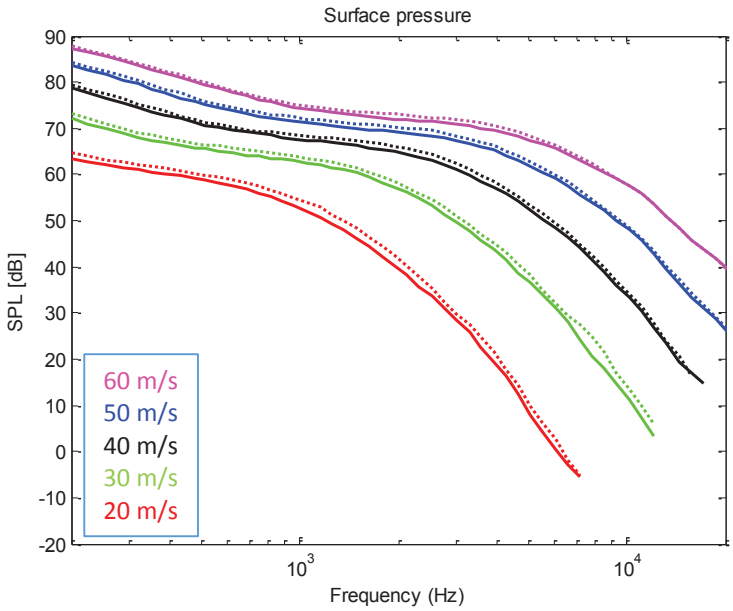

Figure 3.2 Comparison of surface pressure spectra for smooth wall (solid lines) and smooth wall with fabric mounts (dotted lines)

3.2 Effect of Roughness on Surface Pressure Fluctuations

To understand the effect of canopies on the surface pressure fluctuations, it is first necessary to discuss the surface pressure spectra of the smooth wall and uncovered roughness cases. These spectra are presented for each rough surface compared with that for the smooth wall. Figure 3.3, Figure 3.4, and Figure 3.5 show comparisons between the smooth wall and the 3mm hemispherical roughness, sandpaper, and recessed needle bed, respectively.

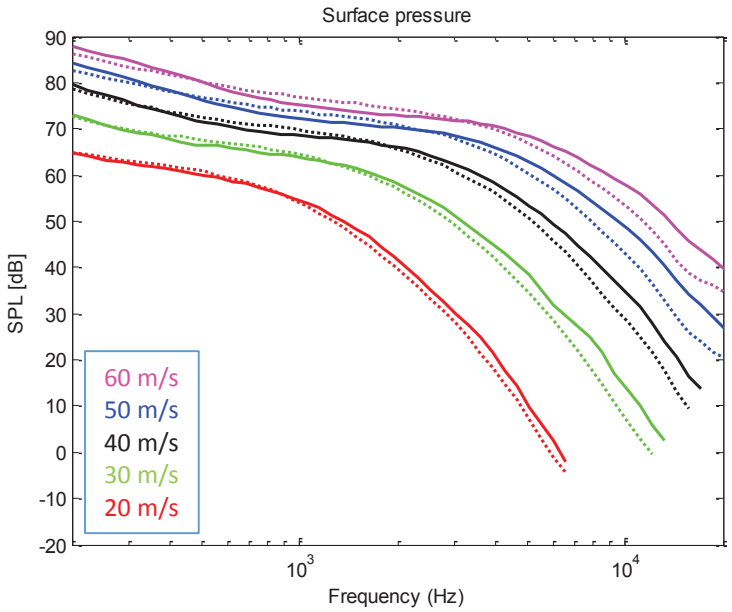

Figure 3.3. Comparison of surface pressure spectra for smooth wall (solid lines) and 3mm hemispheres (dotted lines)

Considering first the smooth wall pressure spectra, three distinct regions become apparent. First, the low-frequency range (below about 1 kHz) can be seen to be dominated by high amplitude fluctuations. These high spectral levels are likely due to the large-scale, high-energy turbulent structures which are present in the outer mixing layer of the flow. In the mid-frequency range (from 1 kHz up to 3-6 kHz depending on velocity), the spectra display a slope that is roughly equal to -0.8. This can be compared to the overlap region of typical external flow boundary layers, and is to be expected for the current flow. Finally, the high-frequency range displays a rapid decrease in spectral levels. This is evidence of the typical energy cascade mechanism of turbulent boundary layers, along with viscous dissipation of the smallest turbulent structures present in the flow. For low jet speeds (20-40 m/s), the spectra have been truncated at higher frequencies to eliminate meaningless data which simply represent the noise floor of the microphones used for this study. As flow speed is increased, the spectra are shifted in the direction of increasing spectral density and increasing frequency. The increased levels at higher velocities are the result of the greater turbulent energy present in the flow. The shift in frequency is caused by an increase in the convective velocity of the turbulent structures which cause the pressure fluctuations. Comparing these spectra to those of Alexander *et al.* (2012) reveals slightly (1-2 dB) higher levels across the entire frequency range, with particularly (2-4 dB) higher levels at low frequencies. These differences are attributed to the modification of the facility in the time between these measurements, which likely had the greatest impact on the low frequency turbulent structures present in the mixing layer, and also resulted in a slightly higher velocity throughout the flow.

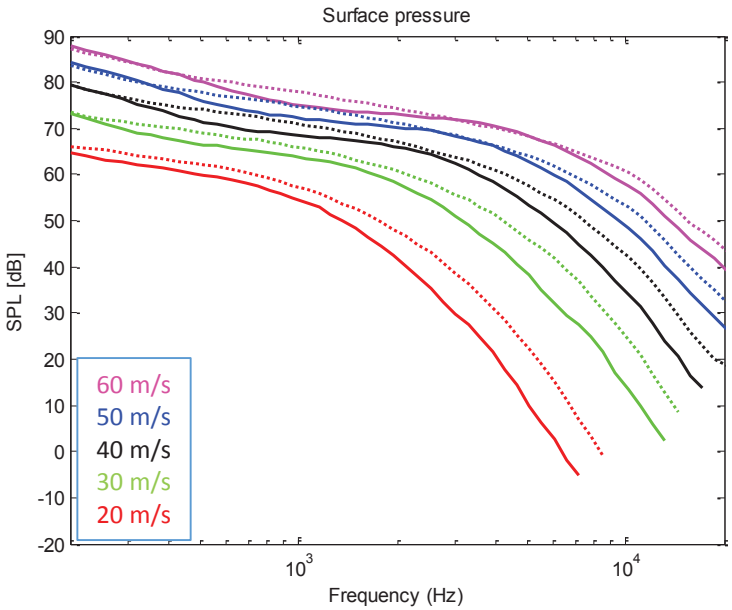

Figure 3.4. Comparison of surface pressure spectra for smooth wall (solid lines) and sandpaper (dotted lines)

With the understanding of the smooth wall results, attention can now be turned to the effects of surface roughness on these spectra. Each rough surface affects the surface pressure spectra in a unique way that is entirely dependent on the particular geometry of the surface. First, as seen in Figure 3.3, the 3mm hemispherical roughness leads to a 1-2 dB increase in pressure levels in the low to mid-frequency range (500 Hz to 2 kHz at a jet velocity of 60 m/s). This is likely due to the large, round elements producing more large scale turbulence. At higher frequencies, an attenuation of up to 5 dB is observed. The effect of this surface on the overall spectra is related to the position of the microphone relative to the surrounding elements. Because the microphone is placed between streamwise rows of elements, the primary flow effects of the elements (turbulent wakes) are not observed by the microphone.

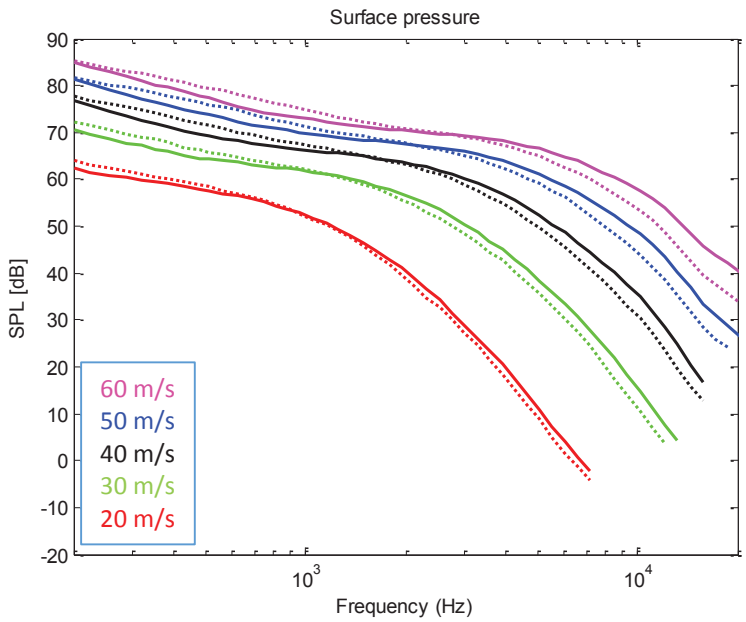

Figure 3.5. Comparison of surface pressure spectra for smooth wall (solid lines) and recessed needle bed (dotted lines)

Next, in Figure 3.4, the sandpaper roughness can be seen to increase the pressure levels by 1-10 dB across the entire frequency range. In contrast with the 3mm hemispheres, this surface is more homogenous, and the increase in turbulence caused by the sandpaper is well-characterized by the spectra. The recessed needle bed roughness (Figure 3.5) shares a similar situation to that of the 3mm hemispheres, and the spectral levels show a 1-3 dB increase at low frequencies, along with attenuation of the high-frequency fluctuations which is slightly less than the attenuation seen in the 3mm hemisphere case.

3.3 Effect of Roughness on Far-Field Sound

Figure 3.6, Figure 3.7, and Figure 3.8 display the far-field noise measured from each rough surface compared with that measured from the smooth wall. The smooth wall data simply represents the background-noise of the wall-jet facility, which has been shown to be dominated by jet noise at the nozzle by Devenport *et al.* (2011). The increased far-field levels are caused by scattering of the near-field pressure fluctuations discussed above. The relationship between far-field noise and wall pressure fluctuations can be related to the discussion above regarding the position of the surface pressure microphone relative to the surrounding roughness elements. Although the surface pressure microphone may not display the true surface pressure spectra which is present at the location of the roughness elements, the far-field microphone records the combined effect of pressure interactions with the full fetch of roughness elements.

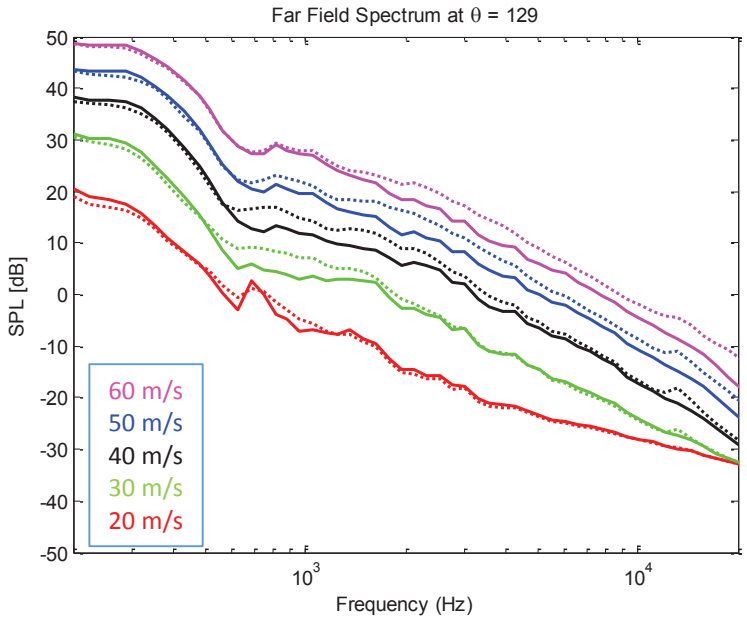

Figure 3.6. Comparison of far-field noise spectra for smooth wall (solid lines) and 3mm hemispheres (dotted lines)

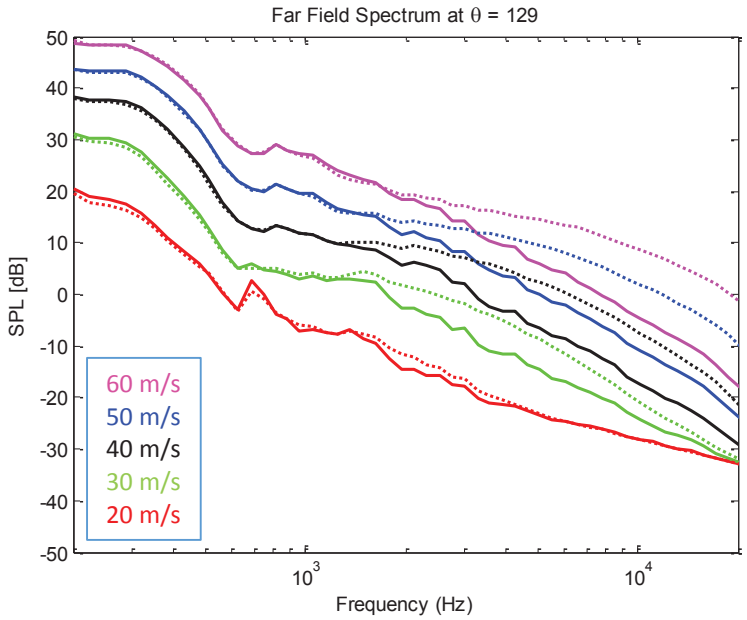

Figure 3.7. Comparison of far-field noise spectra for smooth wall (solid lines) and sandpaper (dotted lines)

The 3mm hemispherical roughness (Figure 3.6) produced a modest increase in noise levels across most of the measured frequency range for jet velocities of 40 m/s and above. The small increase in levels, along with the associated surface pressure fluctuations, show that the scattering effect of the increased turbulence produced by upstream elements leads to increased levels of up to 3 dB above 700 Hz. The effect of the sandpaper roughness (Figure 3.7) is a strong contrast to that of the 3mm hemispherical roughness. Increased levels of up to 15 dB were observed at high frequencies, which demonstrate that not only is the sandpaper a strong producer of increased turbulence, it is also an efficient scattering surface for the turbulent fluctuations in the flow. The majority of the sandpaper's influence on the far-field levels is confined to the mid to high-

frequency range above 1.5 or 2 kHz, depending on flow speed, which is explained by the small size of the roughness elements having little effect on the large-scale fluctuations responsible for low-frequency noise.

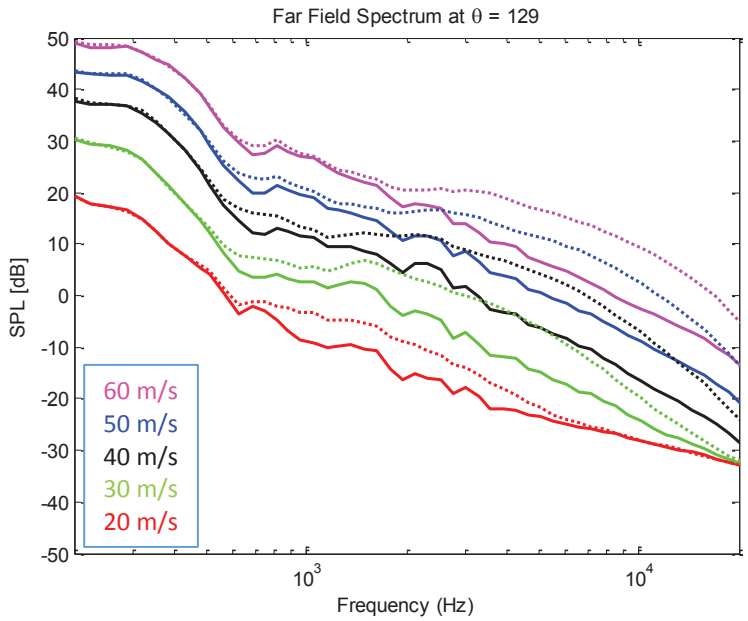

Figure 3.8. Comparison of far-field noise spectra for smooth wall (solid lines) and recessed needle bed (dotted lines)

The needle bed (Figure 3.8) was shown to be an extremely efficient noise producer, leading to increased far-field levels of up to 8-15 dB in the mid-frequency range (near 1-3 kHz depending on flow velocity). In addition, these increased levels were sustained through the high-frequency range, particularly for higher velocities (jet speeds above 40 m/s).

3.4 Effect of Optimal Fabric Canopy on Surface Pressure Fluctuations

In this section acoustic and surface pressure fluctuation results are presented and discussed for the various smooth and rough surface conditions with the canopy coverings. The results of placing fabric 5, described above, over each rough surface will be presented first. This canopy most closely mimics the characteristics of the owl-down canopy since it has the thinnest fibers which run approximately 45 degrees relative to the flow direction, while the other canopies have thicker fibers, some of which run perpendicular to the flow direction. Also, it became clear from the data gathered during this experiment that fabric 5 was the most effective in reducing the far-field noise and surface pressure fluctuations while minimizing additional noise from the canopy itself. Results for the other canopies will be presented later. We also focus our presentation on acoustic measurements made with the forward-most far-field microphone, at a receiver angle of 129°, with a discussion of directionality in Section 3.8.

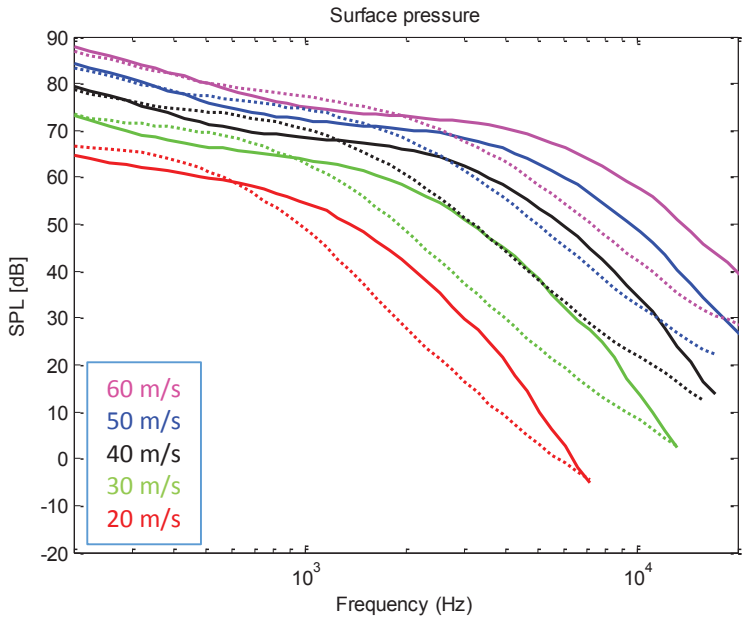

Figure 3.9. Comparison of surface pressure spectra for uncovered smooth wall (solid lines) and smooth wall shrouded by fabric 5 (dotted lines)

Figure 3.9 through Figure 3.12 present surface pressure spectra measured with fabric 5 shrouding the smooth wall and each of the three types of rough surfaces. The dotted lines signify measurements made with the fabric installed above the four surfaces, while the solid lines represent data taken with only the corresponding surface without the canopy. First considering the effect of the canopy on the smooth wall surface pressure fluctuations, it becomes clear that the presence of a canopy has a significant attenuating effect on the flow near the wall. Slight (1-3 dB) increases in the low-frequency component are overshadowed by a strong (10-18 dB) decrease in the middle and high frequency components of the spectra. The shapes of the curves that result from these attenuations may represent spectra in which the turbulent energy cascade is accelerated by the shear layer formed by the canopy. Large turbulent eddies are "cut" into smaller eddies, which then have a shorter cascade before being attenuated completely by viscous interaction. This is similar to the spectral short-cut phenomenon described by Lilley (1998) and Finnigan (2000).

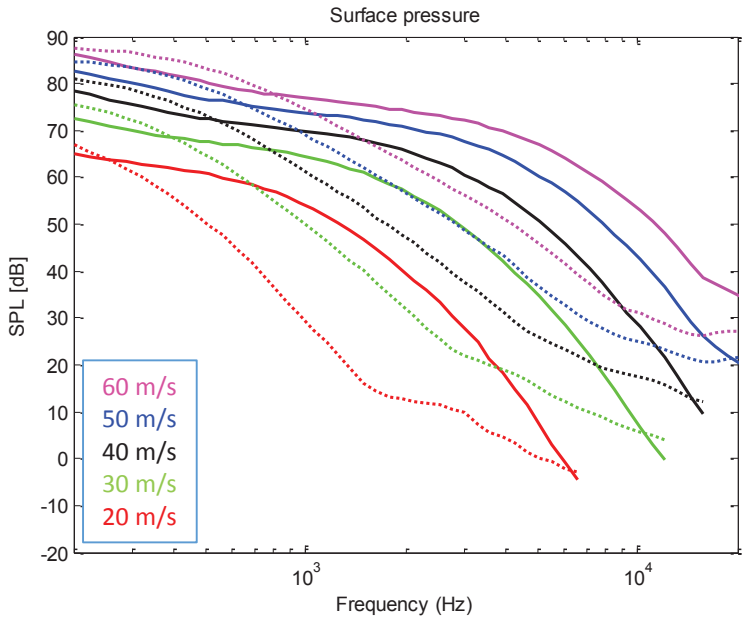

Figure 3.10. Comparison of surface pressure spectra for uncovered 3mm hemispheres (solid lines) and 3mm hemispheres shrouded by fabric 5 (dotted lines)

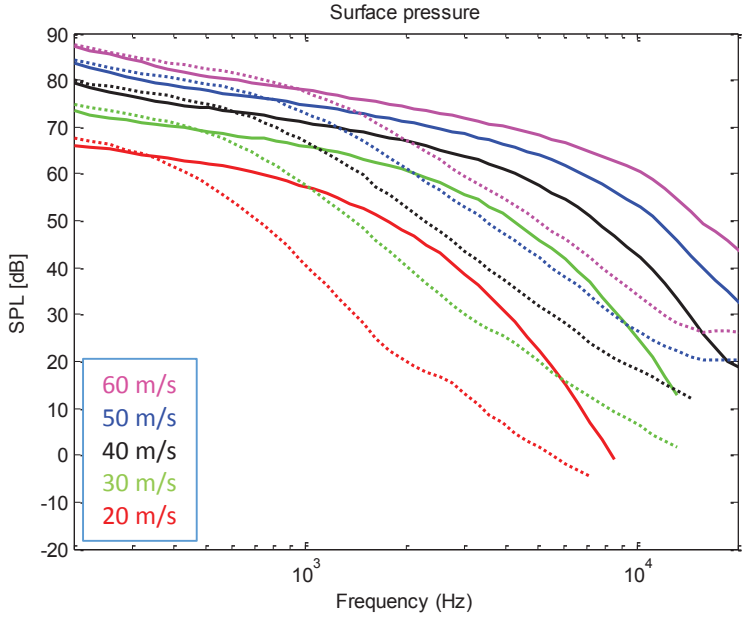

Figure 3.11. Comparison of surface pressure spectra for uncovered sandpaper (solid lines) and sandpaper shrouded by fabric 5 (dotted lines)

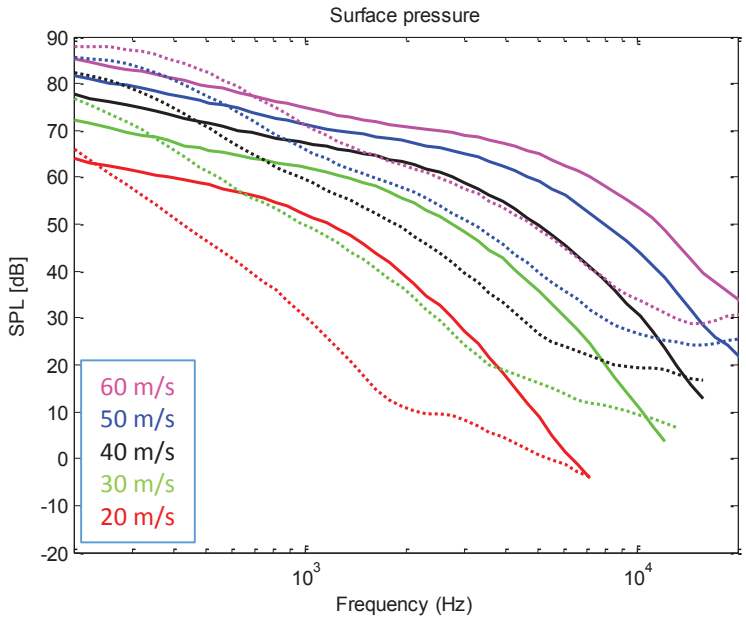

Figure 3.12. Comparison of surface pressure spectra for uncovered recessed needle bed (solid lines) and recessed needle bed shrouded by fabric 5 (dotted lines)

Although these attenuations would be significant in their own right if present for the rough surfaces as well, they are in fact small in comparison to the much larger attenuations which result from the combined presence of both a rough surface and a canopy. For all cases, attenuations of up to 25-30 dB are observed in the mid to high frequency ranges, again with minimal (1-4 dB) increases in the lowest frequency range. The lowest flow speeds seem to experience the greatest attenuation of 30 dB near 1.5-2 kHz, while at higher flow speeds, the attenuation is somewhat reduced to a maximum of 20-25 dB near 8-10kHz. These results could be explained by a slowing of the boundary layer flow by the canopy, which is further enhanced in the presence of roughness.

The results show an interesting parallel to the nature of the owls' downy coating and flight characteristics. It is estimated that in flight, the Reynolds number based on the diameter of an individual hair present in the downy coating is on the order of 7, while at a jet speed of 20 m/s, the Reynolds number based on the diameter of an individual thread present in the fabric canopy approaches 20. This result supports the hypothesis that the owls' downy coating is optimized for their particular flight conditions, while a deviation from those conditions leads to a (admittedly modest) decrease in the effectiveness of the coating.

3.5 Effect of Optimal Fabric Canopy on Far-Field Sound

Considering the substantial reductions in surface pressure fluctuations observed for these cases, one would expect some observable reductions of far-field noise while accounting for the self-noise of the canopy itself, which can be perceived in Figure 3.13.

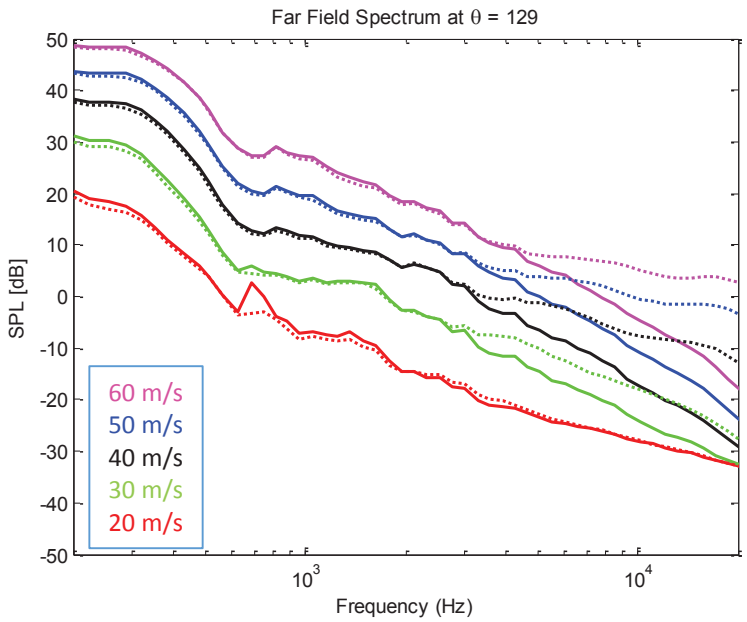

Figure 3.13. Comparison of far-field noise spectra for uncovered smooth wall (solid lines) and smooth wall shrouded by fabric 5 (dotted lines)

Figure 3.13 shows the increased far-field levels measured with the canopy shrouding the smooth wall compared with the levels from only the smooth wall itself. The influence of the canopy is confined to the high frequency region of the spectra. At a jet speed of 60 m/s, the canopy is essentially silent at frequencies below 5 kHz, and the noise steadily grows above this frequency to reach a maximum of 20 dB at 20kHz. Since there is little to no self-noise produced below 5 kHz, one would expect this region to be the best chance for noise reduction considering the sharp decrease in surface pressure fluctuations in this range. Indeed, considering each of the cases where fabric 5 shrouds each of the rough surfaces (Figure 3.14 through Figure 3.16), noise reductions are consistently observed.

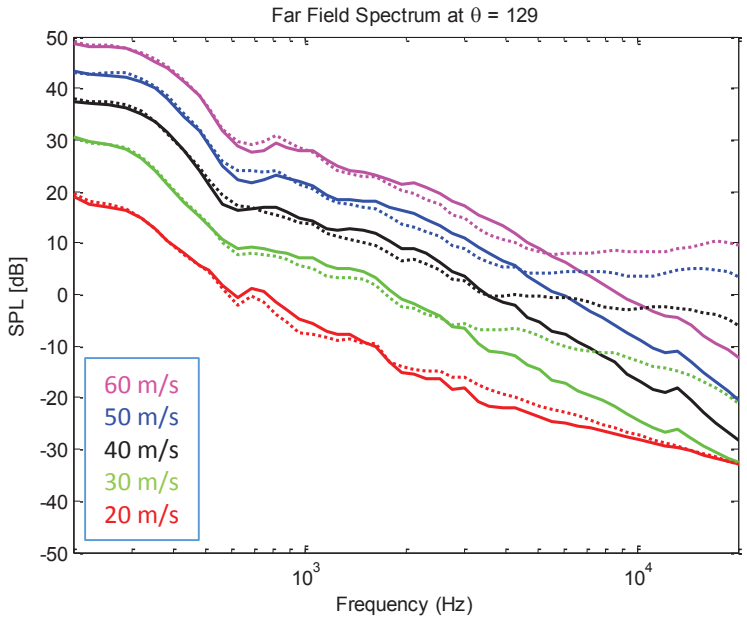

Figure 3.14. Comparison of far-field noise spectra for uncovered 3mm hemispheres (solid lines) and 3mm hemispheres shrouded by fabric 5 (dotted lines)

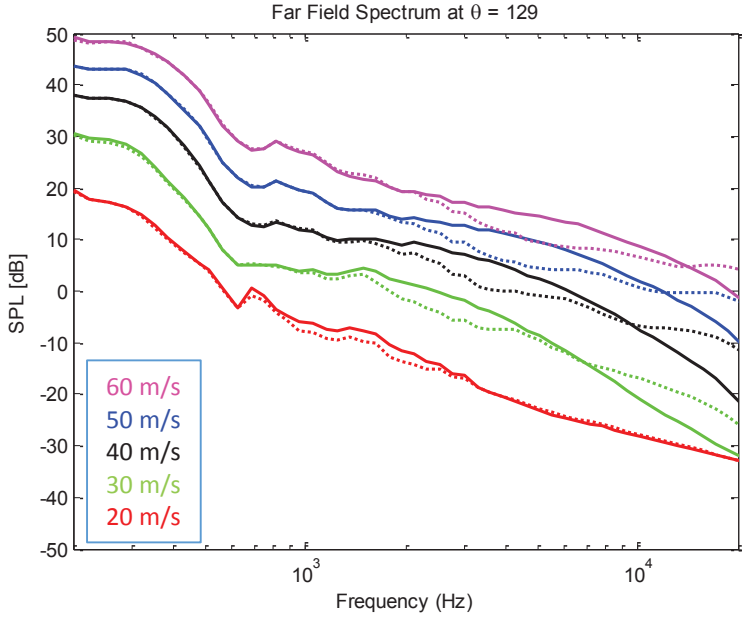

Figure 3.15. Comparison of far-field noise spectra for uncovered sandpaper (solid lines) and sandpaper shrouded by fabric 5 (dotted lines)

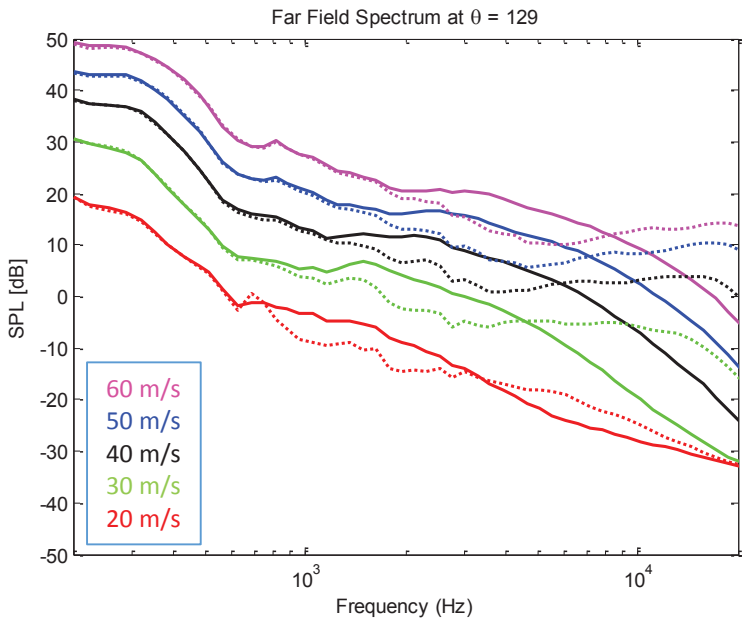

Figure 3.16. Comparison of far-field noise spectra for uncovered recessed needle bed (solid lines) and recessed needle bed shrouded by fabric 5 (dotted lines)

Notably, measureable attenuations of far-field noise are observed for the case of the 3mm roughness (Figure 3.14), despite its relatively low signal-to-noise ratio seen in Figure 3.6. Greater benefit due to the addition of the canopy was observed for the sandpaper roughness (Figure 3.15). Far-field levels were attenuated by 5 dB at 5 kHz for a jet velocity of 60 m/s, and the high-frequency self-noise increased noise levels only above 16 kHz for that case by a maximum of 5 dB. The absolute maximum attenuation was observed for the needle bed case (Figure 3.16), with a 5-8 dB reduction from 3-6 kHz at 60 m/s. However, this case also saw much more high frequency noise due to the canopy, with levels reaching 18dB above the uncovered case at 20 kHz at 60 m/s.

3.6 Effect of Fabric Geometry on Surface Pressure Fluctuation Attenuation

We now turn our attention to the other fabric canopies and their effects on roughness noise. As mentioned above, fabric 5 exhibited the optimal behavior of all of the fabrics investigated by producing the least self-noise while canceling a large portion of roughness noise and yielding a large attenuation of surface pressure fluctuations. However, significant insight about the noise-canceling mechanism can be attained by examining the data from other fabrics and comparing them to their associated geometries. To this end, we now shift the focus to a new subset of the data, with a nozzle speed of 60 m/s.

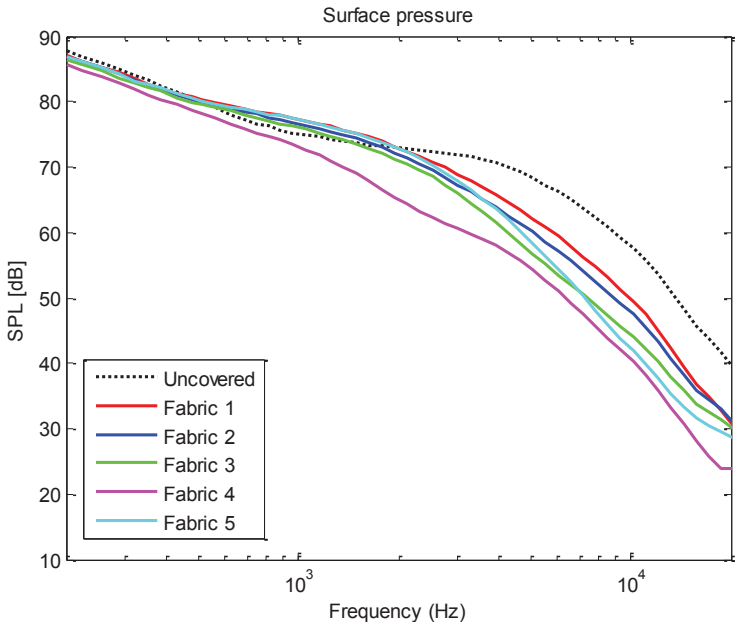

Figure 3.17. Comparison of surface pressure spectra for uncovered smooth wall (dotted line) and smooth wall covered by fabrics (solid lines) at a jet speed of 60 m/s.

Figure 3.17 through Figure 3.20 show the surface pressure spectra with all canopies covering each type of underlying surface. Note that results for fabric 4 covering sandpaper roughness and the needle bed were not obtained for two reasons. First, fabric 4 was quite dissimilar in form to the other fabrics, with a much smaller open area percentage and much thicker fibers, so it was thought that a meaningful comparison between results for this fabric and others would be difficult. Second, it was determined that this fabric performed so poorly above the smooth wall and 3mm hemispherical roughness that testing this fabric above the sandpaper and needle bed would not yield any useful information (this can be seen in Figure 3.21 and Figure 3.22).

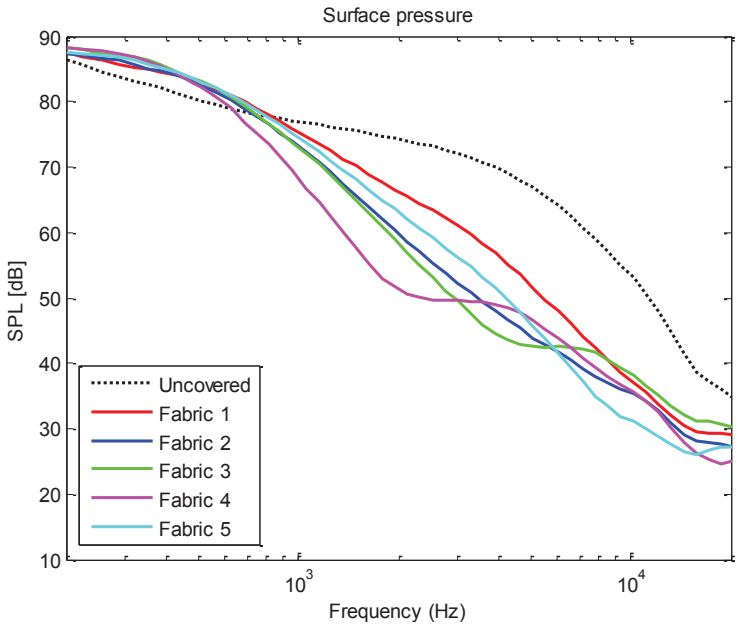

Figure 3.18. Comparison of surface pressure spectra for uncovered 3mm hemispheres (dotted line) and 3mm hemispheres covered by fabrics (solid lines) at a jet speed of 60 m/s.

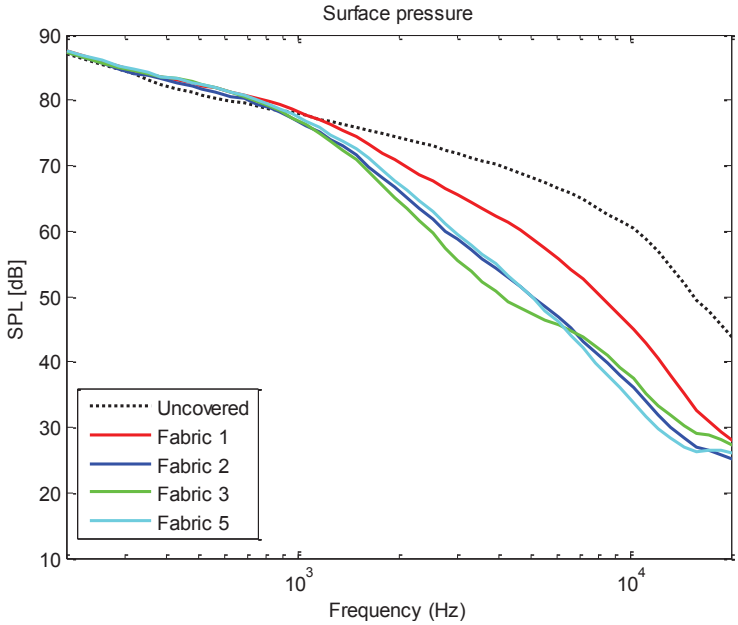

Figure 3.19. Comparison of surface pressure spectra for uncovered sandpaper (dotted line) and sandpaper covered by fabrics (solid lines) at a jet speed of 60 m/s.

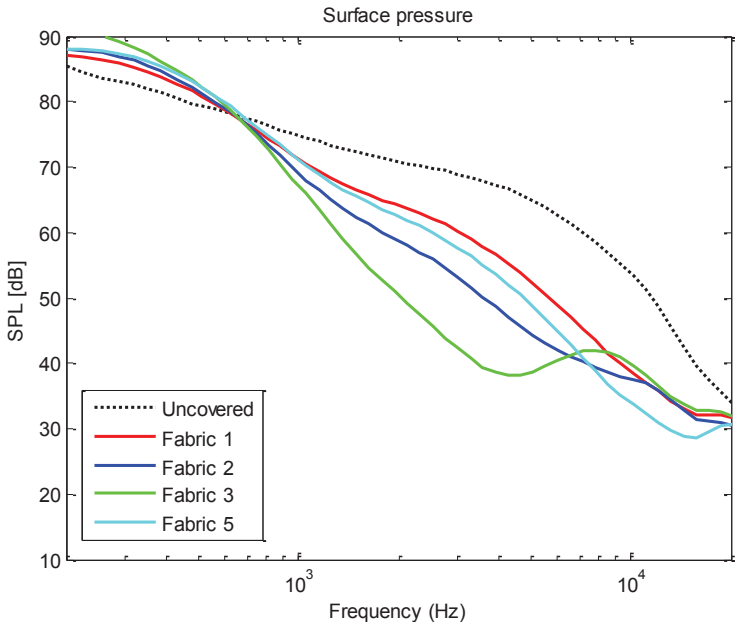

Figure 3.20. Comparison of surface pressure spectra for uncovered recessed needle bed (dotted line) and recessed needle bed covered by fabrics (solid lines) at a jet speed of 60 m/s.

Considering the surface pressure spectra obtained for each fabric, over each underlying rough surface, some behavioral trends become evident. First, comparing all underlying surfaces, the attenuations are largest for the 3mm hemispherical roughness and the needle bed. These surfaces were most effective at elevating the fabric between the mounts, while significant sag was observed to be present for the smooth surface and sandpaper roughness. In addition, these two surfaces experience the most enhancement of low frequency fluctuations. The two phenomena listed here are consistent with the theory relating the surface pressure attenuation to vegetation canopies, where the exponential decay with frequency and increase in the low frequency component seen in the surface pressure spectra are dependent on the height of the canopy above the surface (see Section **Error! Reference source not found.** for further discussion and analysis of this theory).

Another trend seen in the full data set is, for all underlying surfaces, the relative effectiveness of the canopies in attenuating average surface pressure fluctuations remains nearly constant. In each case, fabric 1 achieves the least attenuation overall, while the absolute maximum attenuation is observed for fabric 3 at a frequency near 5kHz. This demonstrates repeatability of the results as well as the robustness of the method of using fabrics to attenuate surface pressure fluctuations for different types of rough surface.

As the surface pressure fluctuations are directly caused by the turbulent eddies present adjacent to the wall, the fabrics can be assumed to influence the structure and path of these eddies as they flow past the fabric, thereby resulting in the observed attenuation of pressure fluctuations. Because each fabric resulted in a unique attenuation pattern, it is clear that the particular geometry of the fabric will influence the turbulent eddies in a unique way. By observing the parameters of each fabric, along with its attenuation pattern, the effect of each geometric parameter (ie. fiber thickness, pore size, etc.) can be identified.

The least effective canopy, fabric 1, has the largest space between the fibers at 3.9 mm, with small (0.3 mm diameter) fibers relative to the size of the "pores". Based on its poor

performance relative to the other fabrics, it is plausible that the turbulent eddies are relatively unhindered by the presence of the sparse, fine fibers. Fabric 2 has slightly smaller (3.1 mm) pores than fabric 1, and thicker (0.4 mm diameter) fibers. This fabric achieves 8 dB more attenuation over Fabric 1 in the mid-frequency range for cases with roughness present, but in most cases at high frequencies (by 10 kHz), the attenuation returns to that seen for Fabric 1. The thicker fibers could be the cause of the increased attenuation at mid frequencies, as the thicker fibers are able to absorb more energy from these (relatively strong) eddies, while the smallest eddies are still able to pass through the fabric's pores unhindered, resulting in limited attenuation at high frequencies.

Fabric 5 has the smallest pores of diameter 1.6 mm, but also has very thin, delicate fibers with diameter of 0.06 mm. The mid-frequency attenuation can be seen to fall somewhere between fabrics 1 and 2 for all cases, while the high-frequency attenuation reaches 5 dB over those for fabrics 1 and 2. The mid-frequency behavior can be considered to be a result of competing factors, the first of which is the increased number of fibers present in the flow (thereby increasing the amount of energy that can be absorbed), while the second factor is the much thinner fibers which decrease the amount of energy able to be absorbed by the fabric. The high-frequency fluctuations, which are caused by small, relatively weak eddies, can be seen to be easily dampened by the closely-spaced fibers.

Fabric 3 has small pores (2.1 mm diameter) and fibers which are of medium thickness (0.2 mm), along with a large percentage of fibers oriented perpendicular to the flow direction. The effects of these parameters are such that this fabric exhibits good attenuation in the mid-frequencies, likely due primarily to the medium thickness of the fibers. Based on previously discussed results, one might expect the small pores to also lead to good high-frequency attenuation as well, or at least a marked improvement over fabrics 1 and 2. However, we see that the high-frequency levels sharply increase near 8kHz, particularly for the 3mm hemisphere and needle bed cases. This result may be explained by the orientation of the fibers. Because a large portion of fibers are perpendicular to the airflow, it is plausible that high-frequency eddies are actually produced in the wakes of the fibers themselves which then interact with the surface below the fabric. This theory is supported by the behavior of fabric 4 shrouding the 3mm hemispherical roughness. Also featuring fibers largely perpendicular to the flow direction, fabric 4 produced a peak near 4kHz, with the frequency difference likely caused by its thicker fibers producing larger vortices in their wake.

Considering the above points, it becomes clear that the attenuation of surface pressure fluctuations is not as simple as placing a barrier of a certain open area percentage between the main flow and the surface roughness, as four of the five fabrics tested here had open area percentages near 70%. The particular geometric parameters of the fabrics create a strong frequency-dependence on the attenuation. As such, it can be said that there is no particular, optimal fabric for the attenuation of broadband surface pressure fluctuations. Rather, the geometry of the fabric must be chosen in order to perform best for a frequency range of interest while considering the size and strength of the turbulent eddies to be blocked.

3.7 Effect of Fabric Geometry on Far-Field Noise Spectra

Now, with an understanding of the effects of the fabric on surface pressure fluctuations, focus can be turned to the far-field acoustic signatures of the fabrics over each rough surface. Figure 3.21 through Figure 3.24 display the far-field noise spectra of each rough surface and fabric with the background noise subtracted, so the displayed spectra represent the noise produced only

by the item of interest. Again, some trends are clearly displayed in the data. In general, fabrics with thicker fibers (notably fabric 4) and more fibers oriented perpendicular to the flow (fabrics 3 and 4) produce more noise, as seen for all underlying surfaces. In addition, for fabrics 3 and 4, the peaks in the far-field spectra occur at the same frequencies as the peaks seen in the surface pressure spectra for these fabrics (near 8kHz and 4kHz, respectively). This would imply that these fabrics do indeed produce eddies of a certain size, depending on the thickness of the fibers, which then interact with the underlying surface (and perhaps the downstream portion of the fabric itself) to scatter the unsteady pressure to the far-field.

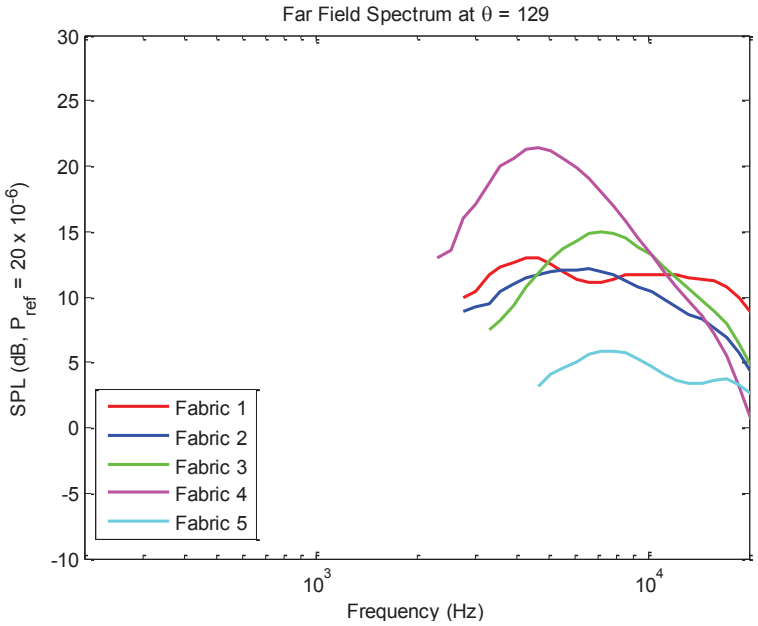

Figure 3.21. Comparison of background-subtracted far-field noise spectra for smooth wall covered by fabrics at a jet speed of 60 m/s.

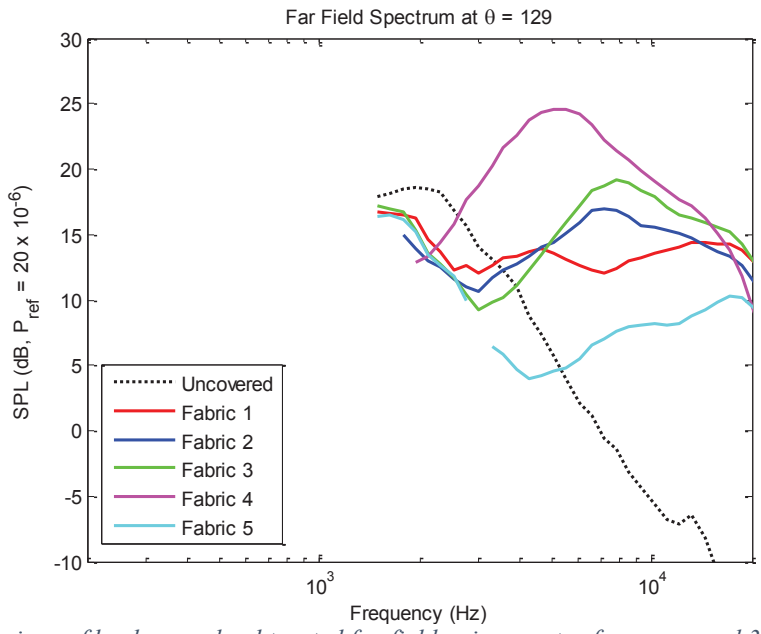

Figure 3.22. Comparison of background-subtracted far-field noise spectra for uncovered 3mm hemispheres (dotted line) and 3mm hemispheres covered by fabrics (solid lines) at a jet speed of 60 m/s.

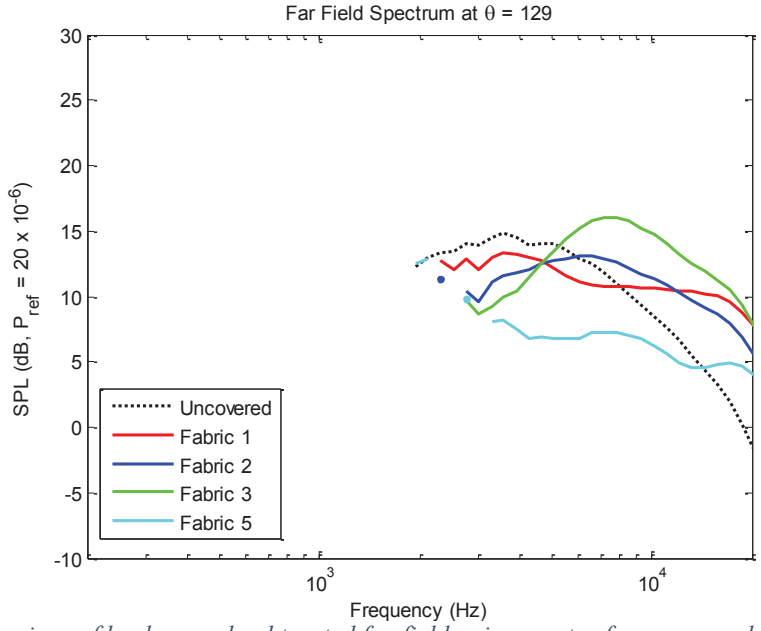

Figure 3.23. Comparison of background-subtracted far-field noise spectra for uncovered sandpaper (dotted line) and sandpaper covered by fabrics (solid lines) at a jet speed of 60 m/s.

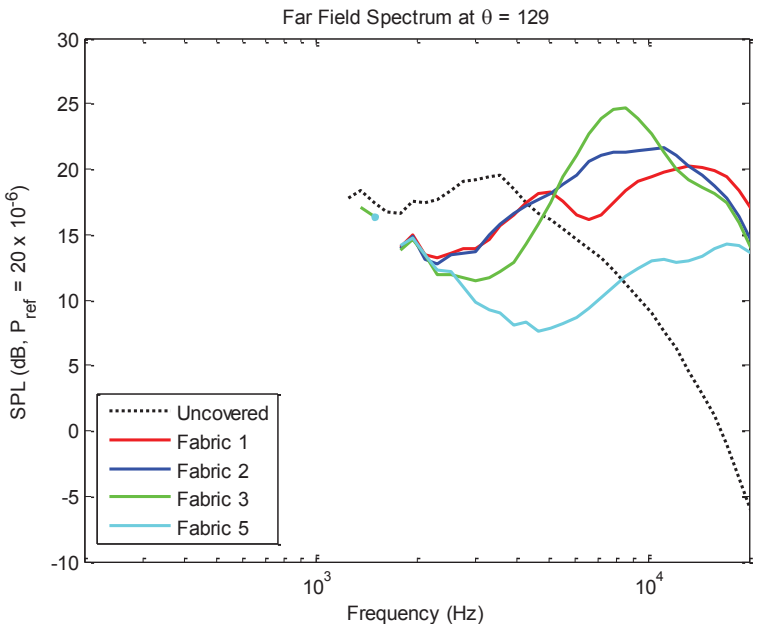

Figure 3.24. Comparison of background-subtracted far-field noise spectra for recessed needle bed (dotted line) and recessed needle bed covered by fabrics (solid lines) at a jet speed of 60 m/s.

Looking at the different surfaces separately, it appears that surfaces which were more effective at elevating the fabric also resulted in the production of more far-field noise. Interestingly, these surfaces also produced the most attenuation of the surface pressure fluctuations, which means the data shows a direct correlation between surface pressure attenuation and far-field noise production, with the notable exception of fabric 5 which produced the least far-field noise with moderate attenuations of surface pressure fluctuations. The higher levels of far-field noise may be explained by higher flow velocity at the location of the canopy when the canopy is raised, due to the nature of the boundary layer of the unmodified tunnel, which results in more energy available to be scattered by the fabric itself.

The precise far-field frequency-dependent behavior is difficult to characterize in terms of fabric geometry, aside from the peaks for fabrics 3 and 4 mentioned above. In relation to each other, the fabrics exhibit some interesting behaviors for each of the rough surfaces. In each case, excluding fabric 5, the fabrics which cause the most reduction in roughness noise at the mid-frequencies also produce the highest peak in the upper frequencies. Specifically, fabric 4 eliminates essentially all noise due to 3mm roughness up to 2 kHz, but produces the highest peak at 5-6kHz. Interestingly, considering a peak frequency of 6 kHz, a thread diameter of 0.7 mm, and an edge velocity of approximately 22 m/s, the Strouhal number can be calculated to be 0.2, which is precisely the value for bluff-body vortex shedding. For the other rough surfaces, fabric 3 cuts most of the noise up to around 3 kHz, but produces a large peak near 8kHz. Fabric 2 is somewhat of a middle case, while fabric 1 yields a nearly flat spectra from 3kHz up to 20kHz. This trend is evidence of the spectral-short cut mechanism described in the context of flows over forest canopies. The transfer of energy from lower to higher frequencies may be the cause of the increased high-frequency noise. As more energy is transferred from lower frequencies, as with fabrics 3 and 4, the additional high-frequency energy results in high levels in the upper frequency range. This trend is present for all underlying rough surfaces, but is most clearly seen for the 3mm hemispherical roughness (Figure 3.22).

As was the case with the surface pressure attenuations, it is again evident that any reduction of roughness noise is not as simple as placing a fabric of certain open area above the roughness, as the particular geometric features of the fabric play a large role in the performance and additional noise generated by the fabrics.

The needle bed results (Figure 3.24) require additional notes regarding uncertainty in the measured spectra. During the experiments featuring both the needle bed and a fabric covering, some additional noise may have been caused by vibrations of the fabric and its associated impacts with the needle bed itself. This was observed through entering the wind tunnel, manually listening to the sound of the needle bed and fabric, and identifying the subjective characteristic of the noise produced. As such, these results may be considered to have an additional $\pm$2-3 dB uncertainty in the spectra, as the acoustic signature of the arrangement was not purely caused by aeroacoustic effects, but rather through structural vibration and interaction. Although the far-field results may be suspect, the surface pressure results were not thought to be affected, and the fact that the trends observed for the far-field noise were similar to those seen for other rough surfaces indicates that the issue may not have resulted in broadband noise contamination.

3.8 Directionality of Fabric Canopy Far-Field Noise

As discussed above, the most upstream microphone, situated at 129° relative to the flow direction, was used to analyze the far-field noise results. The issue of directionality should be considered separately for both the rough surfaces themselves and for the canopies, and rather than present all results obtained during the experiment, representative samples will be chosen for the rough surfaces and canopies. As such, background-subtracted far-field results from multiple microphones are presented first for the sandpaper roughness in Figure 3.25. These results were chosen for the high signal-to-noise ratio which allows the background-subtracted results to clearly display the relevant data from each microphone. Results from multiple microphones are then presented in Figure 3.26 for fabric 3 shrouding sandpaper, also for the high signal-to-noise ratio.

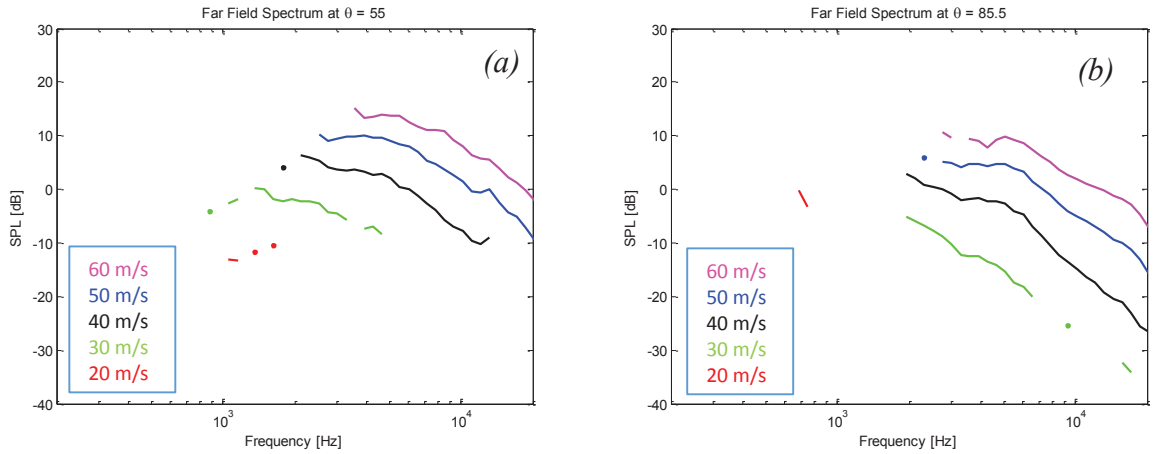

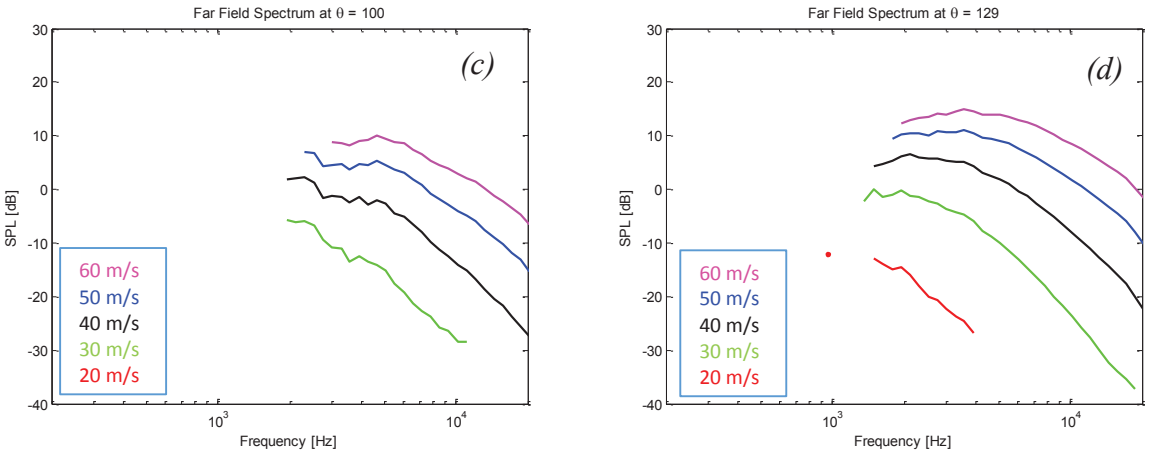

Figure 3.25. Comparison of background-subtracted far-field noise spectra for sandpaper roughness for microphones at 55° (a), 85.5° (b), 100° (c), and 129° (d)

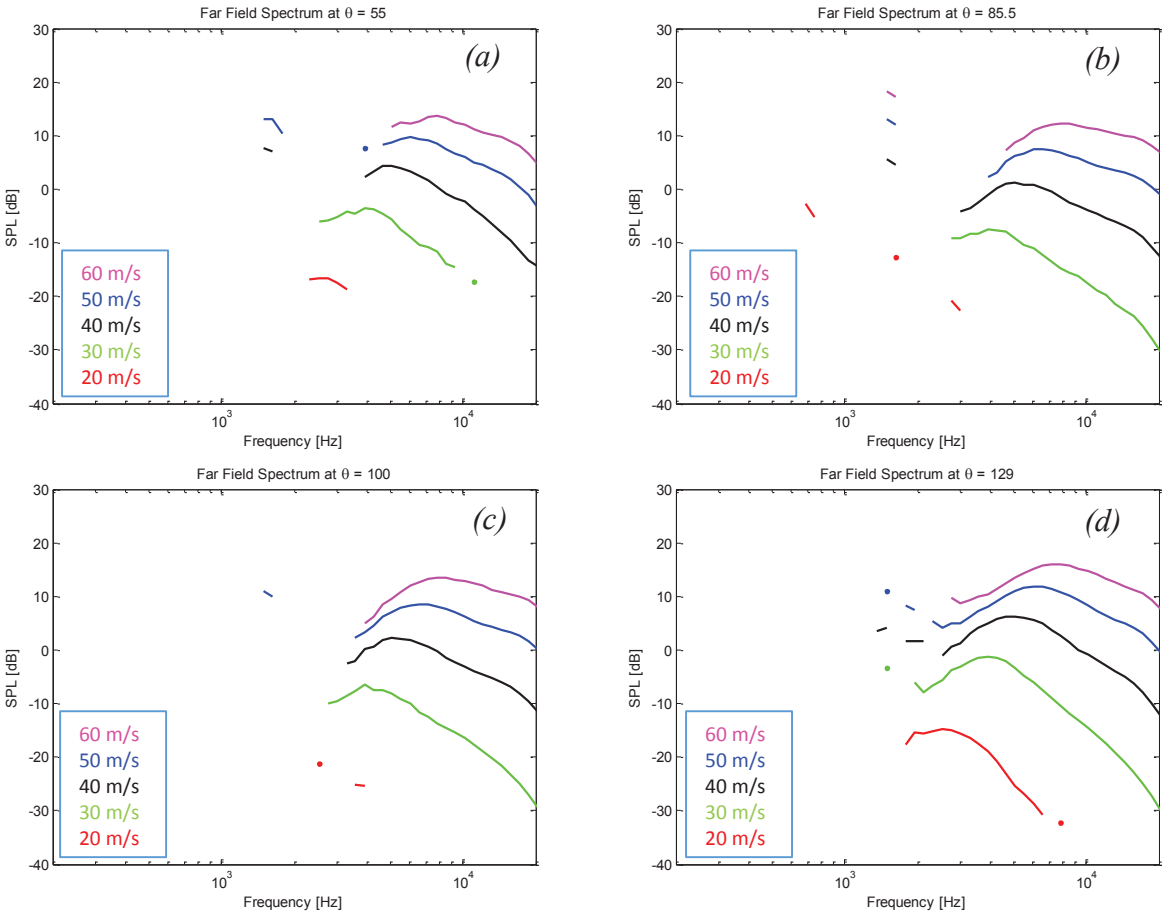

Figure 3.26. Comparison of background-subtracted far-field noise spectra for sandpaper shrouded by fabric 3 for microphones at 55° (a), 85.5° (b), 100° (c), and 129° (d)

As can be seen in Figure 3.25 and Figure 3.26, the effect of directionality is approximately the same both with and without a canopy present. The majority of noise is projected upstream and downstream (towards the 55° and 129° microphones), which suggests a dipole-type noise source. Analysis of the isolated fabric, though not shown here, also revealed a dipole-type directivity,

which confirms that the presence of a fabric does not alter the typical directivity of roughness noise. It can also be concluded that data from the microphone located at 129° is representative of the data taken from all microphones.

3.9 Validation of Unidirectional Canopy Mounts

The results of the fabric canopy experiment showed that, in general, far-field noise increased as the fabrics featured cross-threads placed at higher angles relative to the flow direction. As such, a new hypothesis was developed which stated that if these cross-threads were to be removed, leaving a canopy with only fibers oriented in the flow direction, then the majority of the canopy self-noise could be eliminated, while the noise-cancelling aspects of the canopy could (hopefully) be retained. This led to the development of a unidirectional canopy featuring faired thread supports upstream and downstream of the roughness fetch. There was concern that the presence of these supports would substantially alter the flow over the sandpaper or canopy, thereby affecting the acoustic behavior of these items. Therefore, before presenting data for the effects of the unidirectional canopies, we first show results that reveal the comparatively minor effects of the thread supports on the radiated noise and surface pressure field.

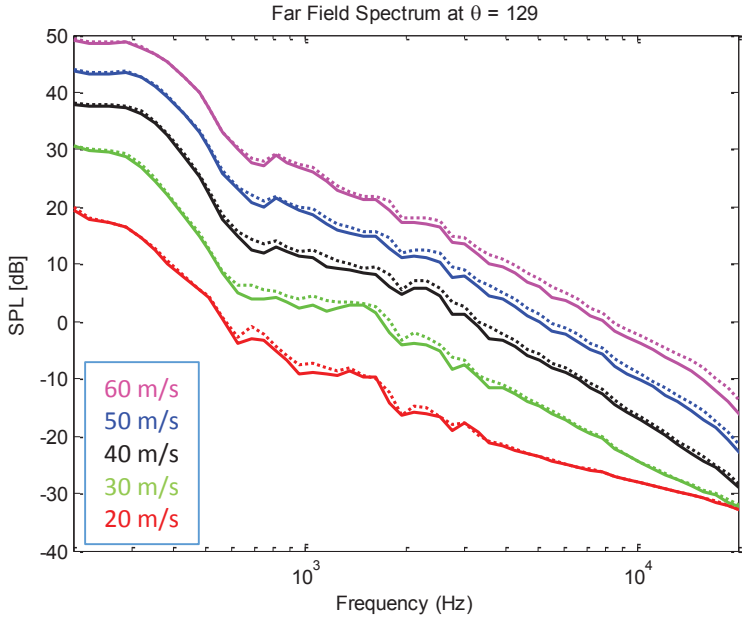

Figure 3.27. Comparison of far-field noise for smooth wall with transition (solid lines) and transition with thread supports (dotted lines)

Figure 3.27 shows the isolated effect of the thread supports compared to the background levels of the tunnel without roughness. The supports raised the far-field levels by approximately 1-2dB above the background across the frequency spectrum. It is hypothesized that the majority of the far-field effect is due to scattering of the nozzle noise from the curved surface of the support, and not to any additional aerodynamic source. Because the typical signal-to-noise ratios of the sandpaper/canopy configurations were much higher than 1-2dB, it was assumed that this small increase would not hide any significant data once the sandpaper/canopies were added.

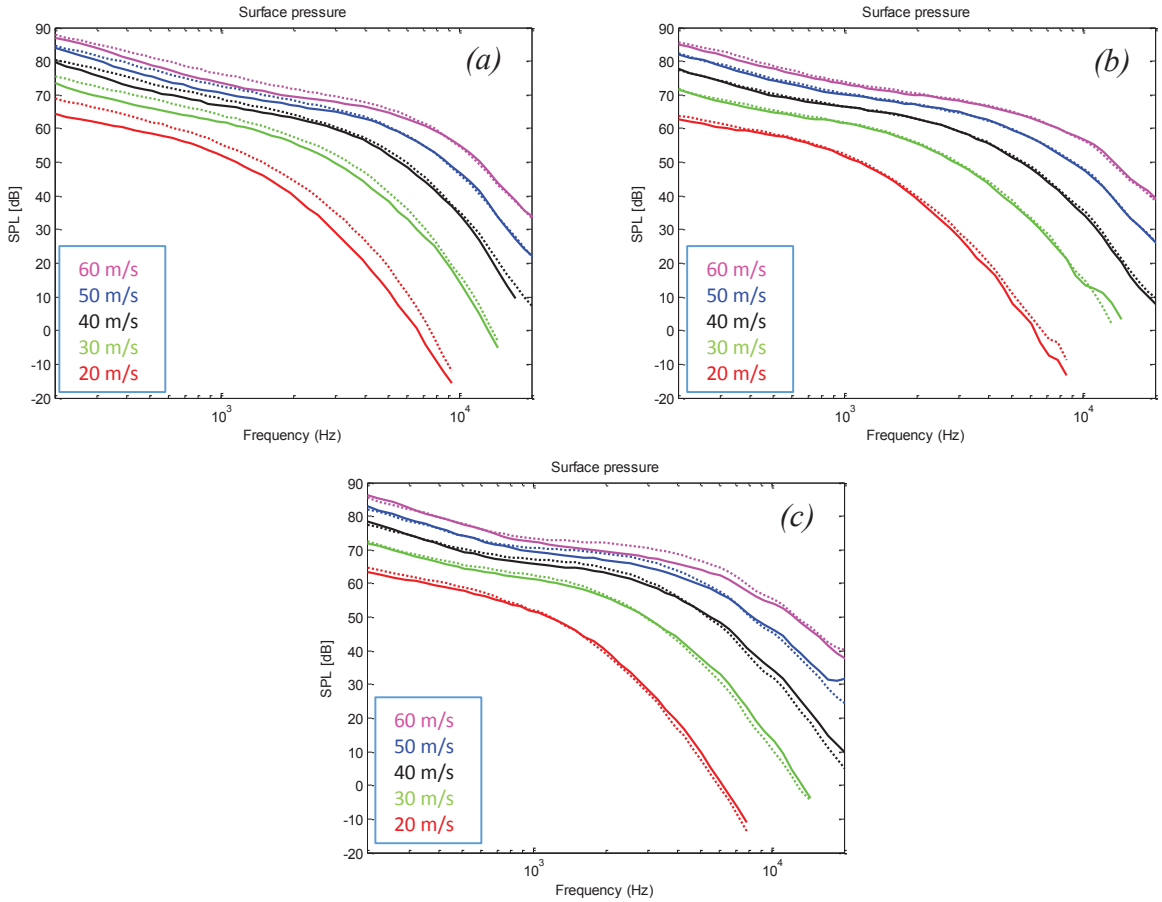

Figure 3.28. Comparison of surface pressure spectra for smooth wall and transition (solid lines) to transition with thread supports (dotted lines) for surface mics 1 (a), 2 (b), and 3 (c)

Because the far-field acoustic signatures of the sandpaper or canopies are due to scattering of the surface pressure fluctuations, it was also necessary to ensure that these were not significantly altered by the presence of the supports. A large change in the surface pressure fluctuation spectra could influence the scattered sound and lead to inconclusive far-field results. Figure 3.28 shows the effect of the supports on the surface pressure spectrum measured by the three surface pressure microphones of configuration B. The most upstream location (microphone 1, Figure 3.28a) shows an increase in magnitude across the frequency range for all speeds, with the greatest increase at 20m/s. This could be caused by local separation at the down-slope of the support, which decreases in severity with increasing Reynolds number. Interestingly, the center location (microphone 2, Figure 3.28b) shows almost no effect from the addition of the supports. The downstream location (microphone 3, Figure 3.28c) experiences an increase in low and mid frequency levels, which could be due to either slight upstream influence of the downstream support, or the uncertainty of the vertical microphone placement in the wall. Overall, it was decided based on these measurements that, although some minor differences were evident in the surface pressure spectra, the mounts did not influence the flow field enough to significantly alter the conclusions which could be drawn from any succeeding data.

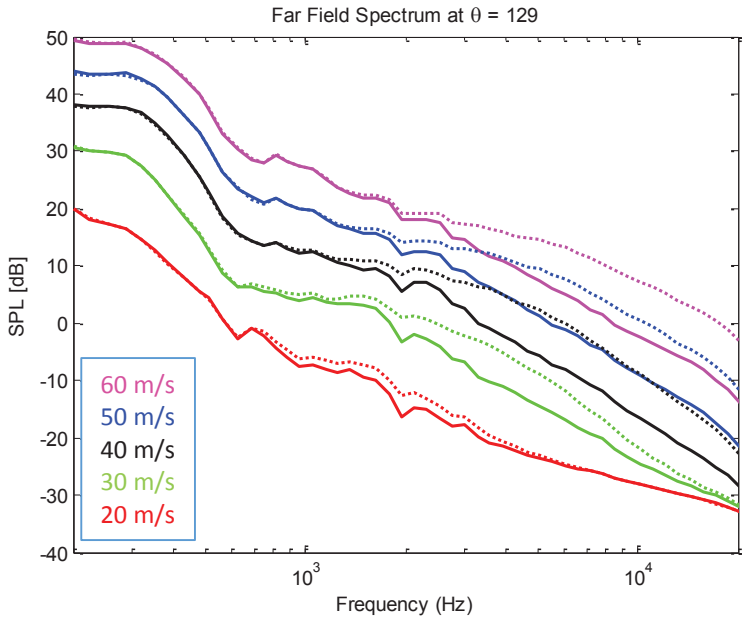

Figure 3.29. Comparison of far-field noise for thread supports (solid lines) and thread supports with sandpaper (dotted lines)

One final check was made regarding the influence of the mounts, which was to place sandpaper between the mounts, as it would be once a canopy was added, and to compare the acoustic data from this configuration with that from the configuration featured in the fabric canopy experiments with only the sandpaper present. Figure 3.29 and Figure 3.30 show the effect of placing sandpaper roughness between the mounts. The qualitative near- and far-field effects are nearly identical to the effect of sandpaper in the fabric canopy experiments. The presence of the mounts does not significantly alter the noise generation of the sandpaper, so it was assumed that the effects of adding a canopy would not be influenced by the support structure.

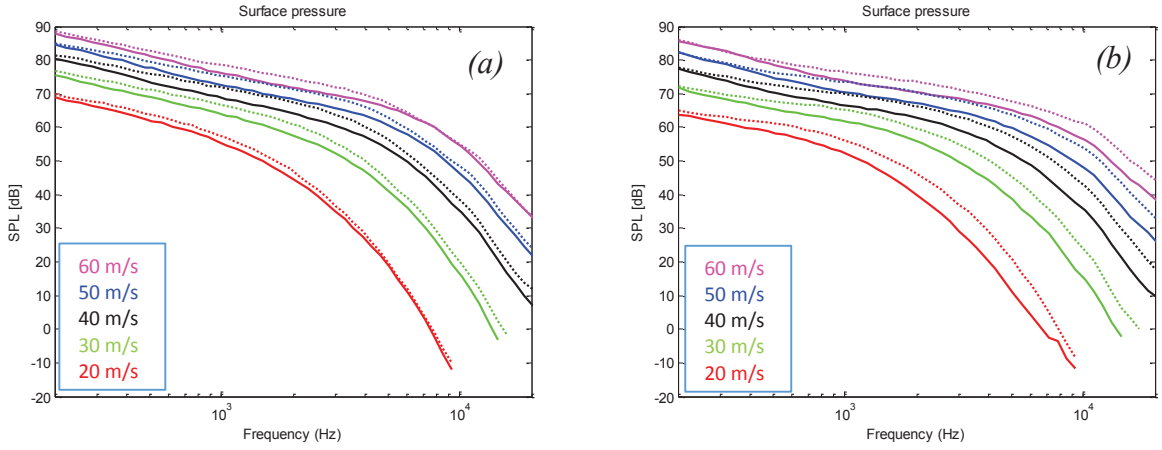

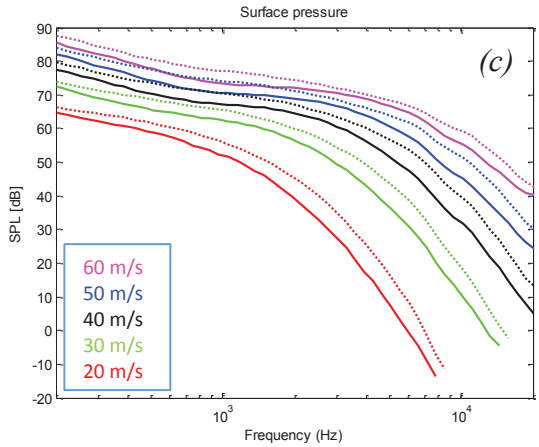

Figure 3.30. Comparison of surface pressure spectra for thread supports (solid lines) and thread supports with sandpaper (dotted lines) for surface mics 1 (a), 2 (b), and 3 (c)

3.10 Effect of Unidirectional Canopy on Noise and Surface Pressure Fluctuations

Figure 3.31a shows the far-field effects of stringing the thinnest fibers over the sandpaper roughness. At higher speeds, far-field sound levels were reduced by as much as 7dB at higher frequencies. At low speeds, the far-field results are distorted somewhat by the noise floor of the microphones, but even so, a noise reduction of about 5 dB is observed. Fortunately, these reductions are achieved without the large increases in high-frequency noise observed with the mesh canopies. Comparing Figure 3.31a and Figure 3.29 shows that a noise reduction is obtained for all frequencies at which roughness noise is observed.

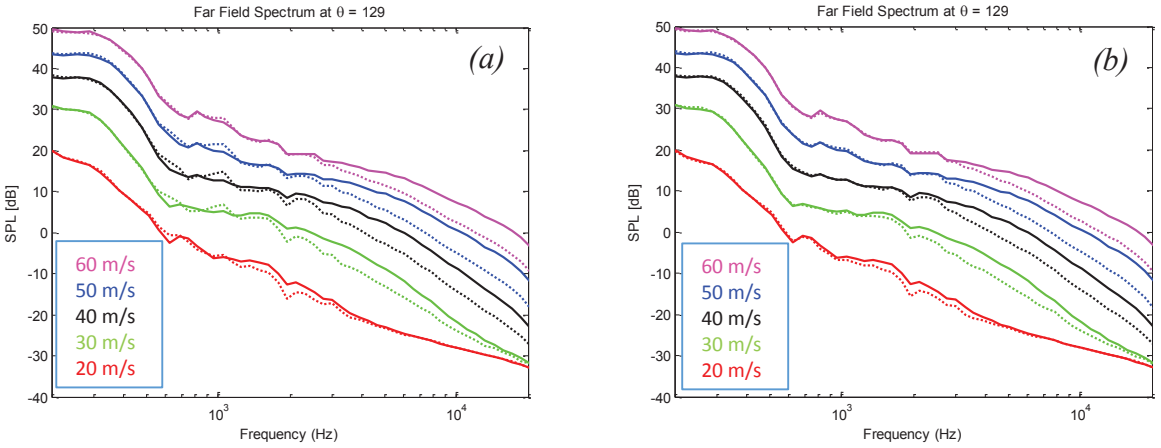

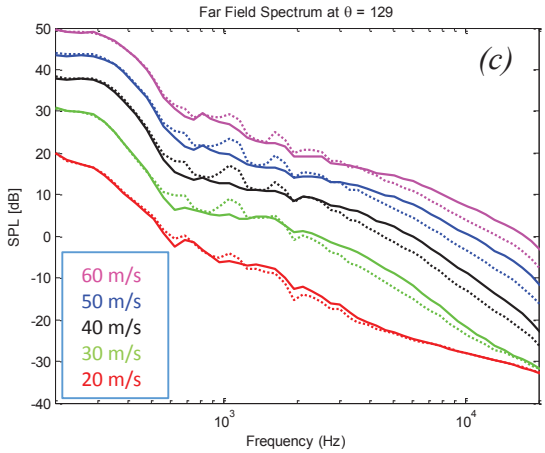

Figure 3.31. Comparison of far-field noise spectra for uncovered sandpaper with mounts (solid lines) and sandpaper covered by canopies 1 (a), 2 (b), and 3 (c) (dotted lines)

Figure 3.31 also shows the acoustic results for unidirectional canopies with different thread diameters, but the same open-area ratio of 70%. As the diameter of the thread (and the spacing between the fibers) increases, the canopy appears to become less effective at reducing the far-field noise. This may be explained by the differences in the attenuation of the surface pressure fluctuations produced by adding the canopy in each case.

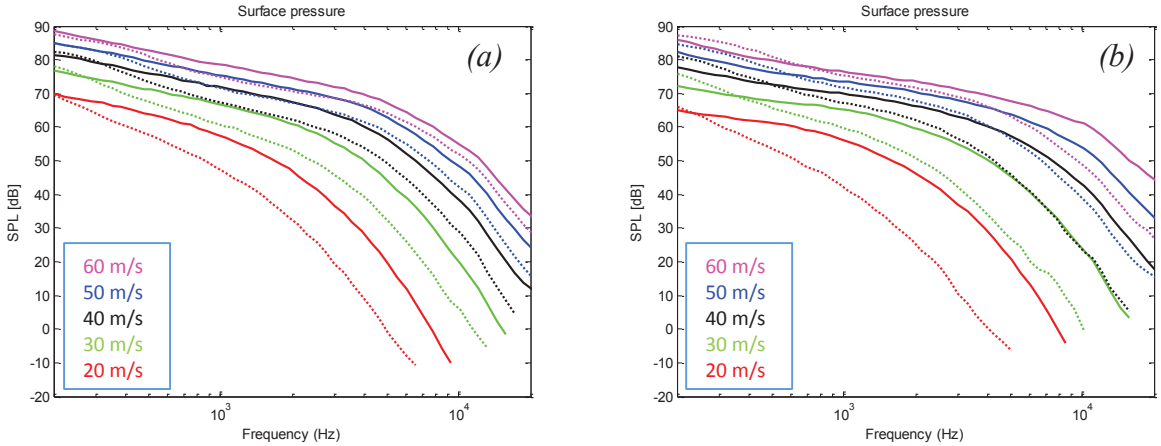

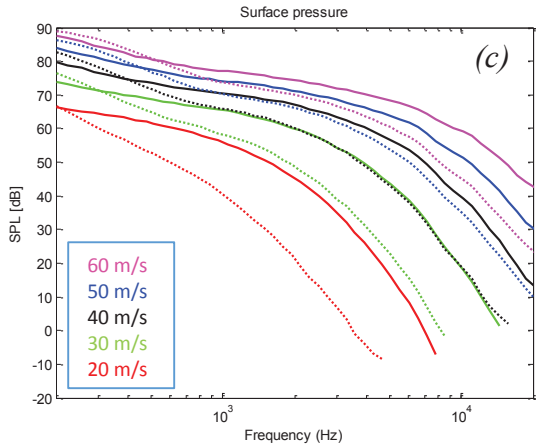

Figure 3.32. Comparison of surface pressure spectra for uncovered sandpaper with mounts (solid lines) and sandpaper covered by canopy 1 (dotted lines) measured by surface mics 1 (a), 2 (b), and 3 (c)

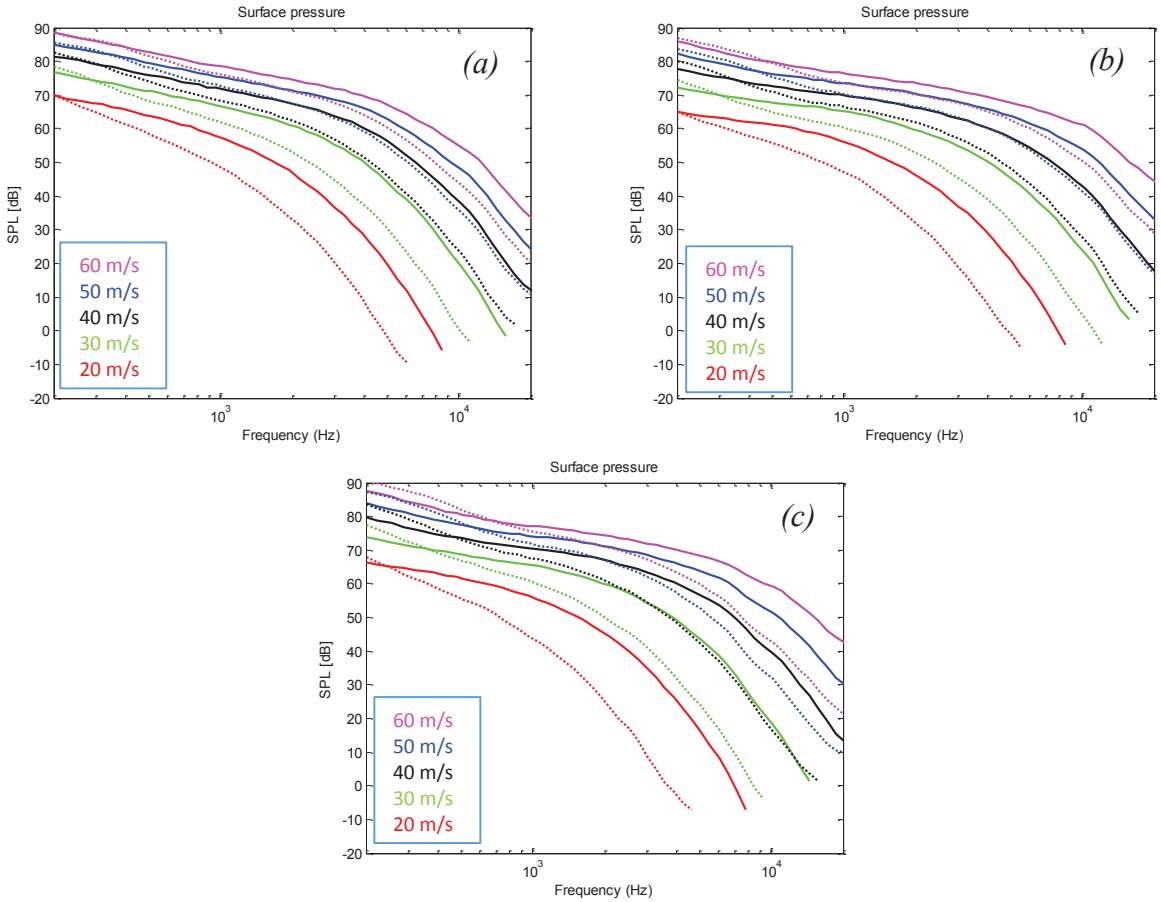

Figure 3.33. Comparison of surface pressure spectra for uncovered sandpaper with mounts (solid lines) and sandpaper covered by canopy 2 (dotted lines) measured by surface mics 1 (a), 2 (b), and 3 (c)

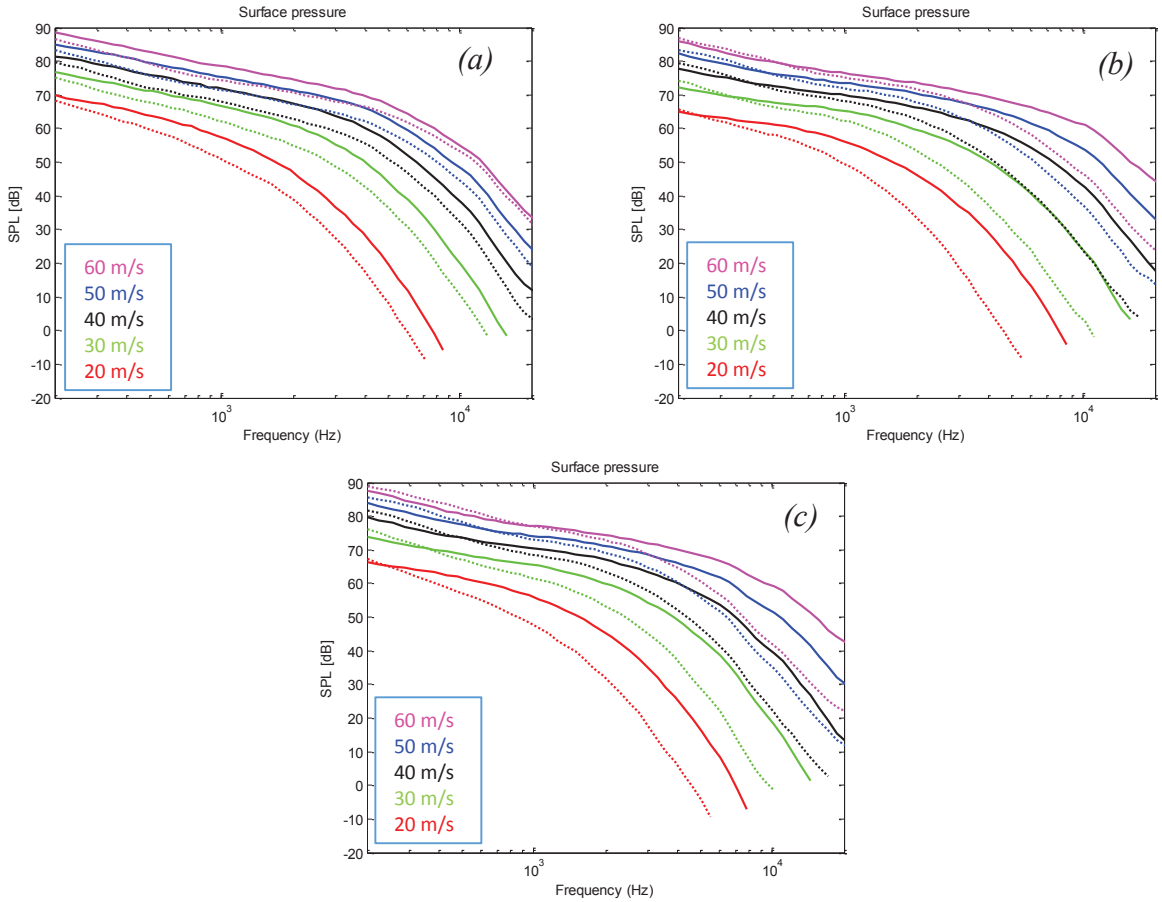

Figure 3.34. Comparison of surface pressure spectra for uncovered sandpaper with mounts (solid lines) and sandpaper covered by canopy 3 (dotted lines) measured by surface mics 1 (a), 2 (b), and 3 (c)

Figure 3.32, Figure 3.33, and Figure 3.34 show the difference in the measured surface pressure spectra for each of the three canopies, at each of the three microphone locations. Interestingly, the trends are not as obvious as one would expect from looking at the far-field data. One would expect to see larger attenuations for the finest canopy and smaller attenuations for the coarsest canopy. In actuality, one sees different trends depending on the microphone and speed being considered. For instance, the 20 m/s data given by microphone 3 displays the expected trend, but the 60m/s data given by the same microphone displays the exact opposite trend in which the coarsest canopy leads to the greatest attenuation at high frequencies. At times, even for the same microphone and speed, different trends are observed depending on which two canopies are compared. These different trends lead to some difficulty in isolating and explaining the effects of the canopy parameters. However, the fact that all of the data exhibits similar frequency dependent attenuations shows that the attenuating effect of the canopies is not reliant on any particular geometric parameter. The mechanism by which the canopy acts can be supposed to be sufficiently complex such that the available data cannot grant a full understanding of the interaction between the canopy and the flow.

Although the attenuations from different canopies do not give solid trends, several other patterns emerge when looking at different microphones under the same canopy, and these patterns are consistent across all canopies. First, there appears to be a strong Reynolds number effect on the attenuation. In general, as flow speed over the canopy increases, the attenuation decreases,

especially for the thinnest canopy. For the case of the thinnest canopy and a jet speed of 20 m/s, the attenuation is highest.

Another pattern seems to be that the attenuation develops as it moves downstream. This trend is seen for all three canopies, as the attenuation seen by microphone 1 is always modest at best, but is most evident in the data corresponding to canopy 3. This may be the sign of a sort of viscous damping mechanism which influences the flow as it moves downstream beneath the canopy. This damping mechanism may be the result of the turbulent eddies' interactions with the canopy itself, or the fact that the small-scale eddies beneath the canopy cannot be sustained since large eddies are absent in the flow, or a combination of the two.

At a fundamental level, this result points to physical scale as the dominant factor in the effectiveness of the canopy. The distance between the fibers likely plays an integral role by determining the scale of eddies which pass through the canopy unhindered, which are distorted or broken up upon passing through, and which stay above the canopy altogether. As an extreme case, one could think of a canopy with many microscopic fibers, with microscopic areas between them. In this case, even with the same open area ratio of 70%, the fibers would physically prevent all but the very smallest turbulent eddies to pass through unhindered, and viscous effects would dominate at this scale to dampen these eddies. This situation closely resembles that of an owl's wing, and their slow flight speeds and microscopic hairs likely combine to produce extremely efficient pressure fluctuation attenuation at the surface. Considering the results of the fabric canopy experiment, however, it must be noted that although the fine hairs work well for the owl in flight, the owl's slow flight speed limits the intensity of the turbulent eddies present in the flow. A flight or underwater vehicle would need thicker, stiffer fibers as the design speed increased as the turbulent eddies would be more intense and would not be affected by thin, flimsy fibers. In addition, the lack of trends seen between different unidirectional canopies may be the result of competing influences between the thicker fibers and wider spacing.

3.11 Surface Pressure Attenuation – Comparison with Theory

Now that the direct results of the experiments have been described in detail, several finer points remain to be discussed. The first is the comparison with a theoretical form of the attenuation discussed in Clark *et al.* (2014). The form of the attenuation comes from analogous flows over forest canopies, described in Chapter 1, in which a spectral short-cut mechanism acts to rapidly shift energy from the lower end of the frequency range to the higher end, where viscous effects then dampen out much of the fluctuations. To develop the attenuation function, the flow is first assumed to be well-developed beneath the canopy, which eliminates the streamwise position from the equation. Next, the attenuation is assumed to depend on angular frequency (ω), flow speed (U), and canopy height (h_c). Canopy height is chosen as a length scale (as opposed to, say, the pore diameter) because the canopy height will directly influence the shape of the boundary layer beneath the canopy, which will have a direct impact on the strength and development of turbulent eddies beneath the canopy. The non-dimensional exponential term then dictates the functional form of these parameters. The form of the attenuation is therefore given as:

$$G_{pp}{}^{canopy} = Ae^{\left(-\frac{2\omega h_c}{U}\right)} * G_{pp}{}^{no\ canopy} \tag{3.1}$$

The attenuation factor is applied to the power spectral density function of the uncovered surface pressure spectra to yield "theoretical" surface pressure spectra. Because, as a first

approximation, the interesting comparison comes simply from the form of the attenuation, it is reasonable to add a constant multiplier (A) to the exponential attenuation which will assist in the fitting of the attenuation to the data while keeping the form of the attenuation true to its original shape. In addition, the canopy height is kept variable, within reason, in order to assist in the fitting of the attenuation. Although this may seem to be a very liberal approach to examining the viability of the exponential attenuation, the variability present in the placement of the fabric canopies in the experiment somewhat justifies the fine-tuning of the canopy height parameter within the uncertainty of the experimental placement (± 1.5 mm for the 3mm hemispheres). Additionally, while the velocity used in the equation is assumed to be constant, the canopies may reduce the effective velocity, which leads to additional variability in the attenuation factor. This effect will be discussed in more detail below. As will be seen, the fitting of the exponential attenuation yields significant insight into the flow phenomena beneath the canopy.

Table 5. Parameters used to generate exponential curve for each fabric covering 3mm hemispheres

$Fabric$	A	h_c (m)
1	5	0.003
2	4	0.004
3	8	0.005
4	10	0.007
5	6	0.004

One notable difference exists between true forest-type canopies and the experimental (fabric or unidirectional) canopies, which is that the experimental canopies are confined to a thin layer elevated above the surface, whereas the forest canopies extend continuously from the surface to the top layer. This opens the possibility of the presence of eddies beneath the experimental canopies, with length scales smaller than the height of the canopy.

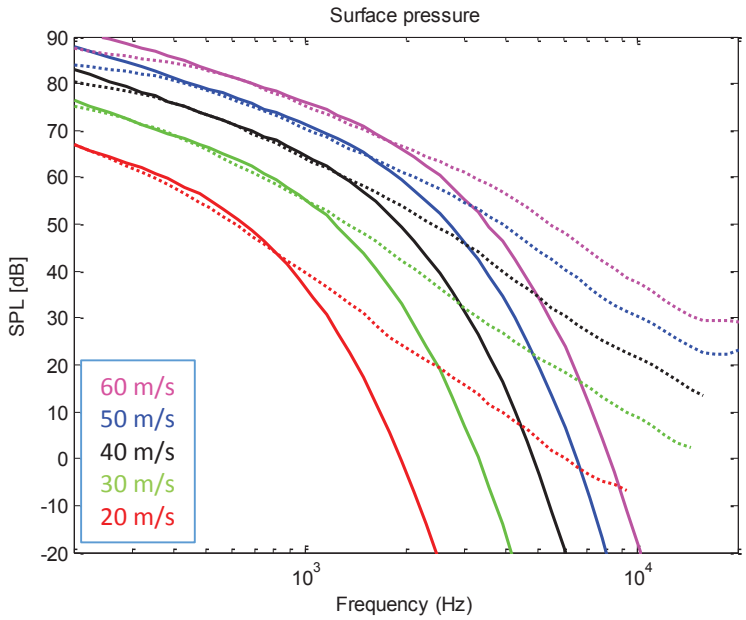

Figure 3.35. Comparison of theoretical (solid lines) and experimental (dotted lines) surface pressure spectra obtained for fabric 1 shrouding 3mm hemispheres

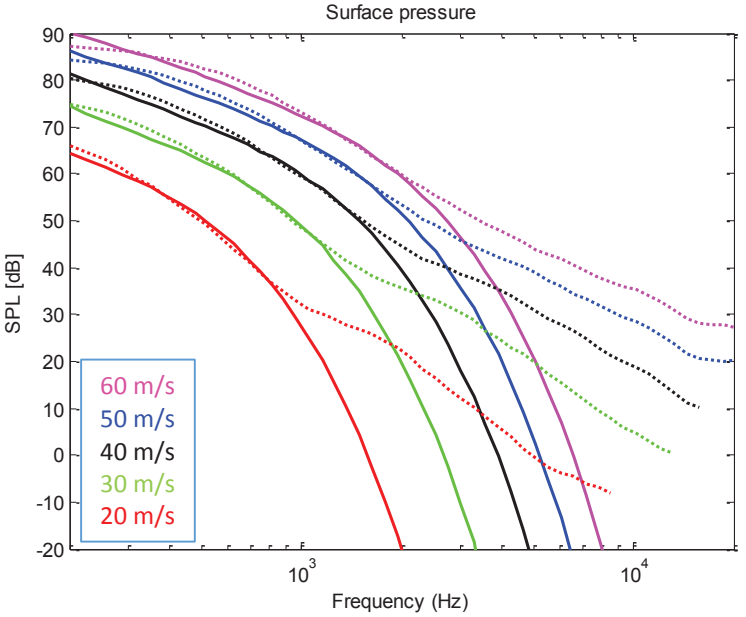

Figure 3.36. Comparison of theoretical (solid lines) and experimental (dotted lines) surface pressure spectra obtained for fabric 2 shrouding 3mm hemispheres

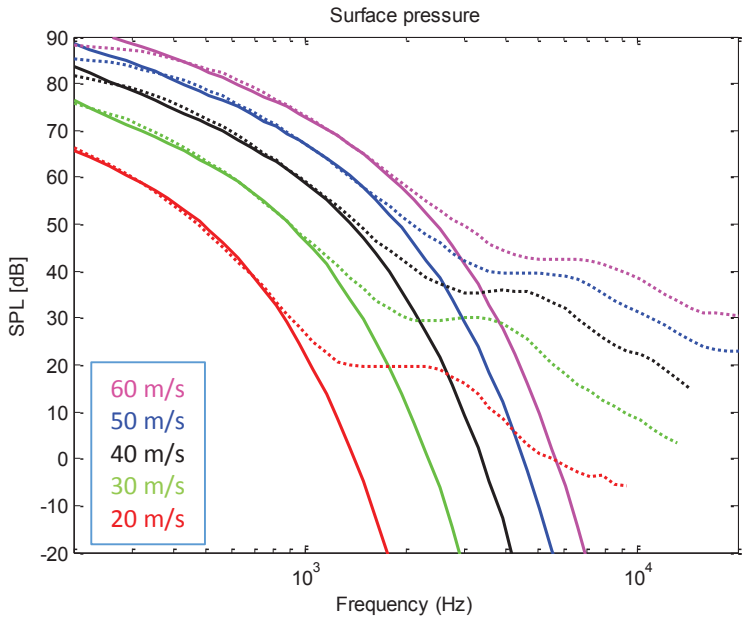

Figure 3.37. Comparison of theoretical (solid lines) and experimental (dotted lines) surface pressure spectra obtained for fabric 3 shrouding 3mm hemispheres

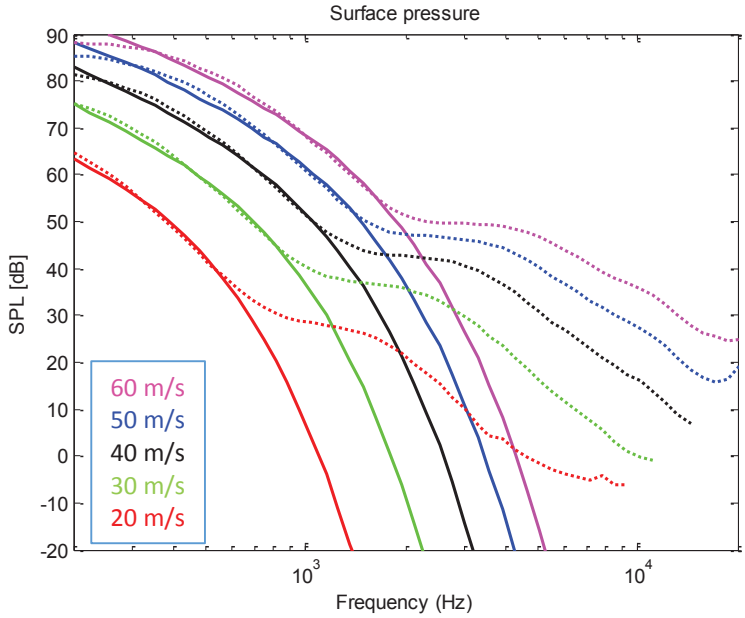

Figure 3.38. Comparison of theoretical (solid lines) and experimental (dotted lines) surface pressure spectra obtained for fabric 4 shrouding 3mm hemispheres

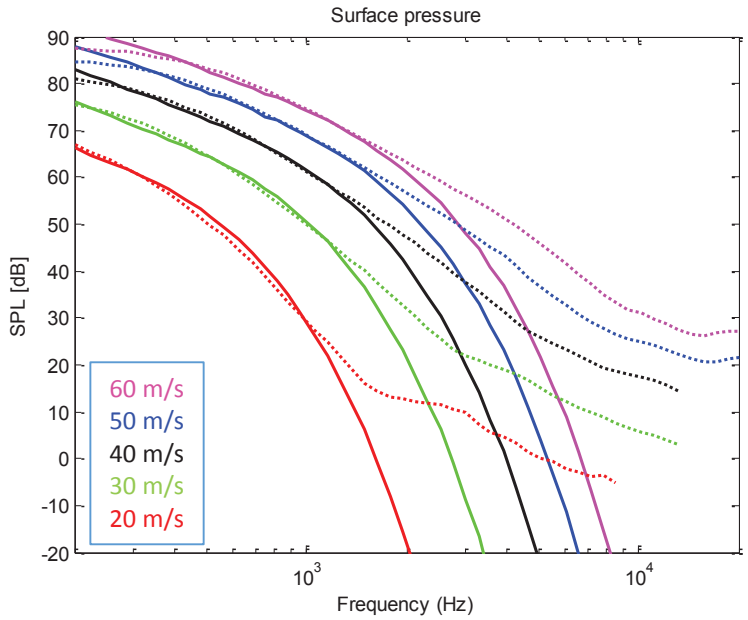

Figure 3.39. Comparison of theoretical (solid lines) and experimental (dotted lines) surface pressure spectra obtained for fabric 5 shrouding 3mm hemispheres

To begin, the theoretical attenuation curve is obtained by choosing values for A and h_c for each fabric to calculate the attenuation factor as a function of frequency. This factor is then multiplied by the surface pressure spectra obtained for the uncovered roughness case. The values A and h_c were chosen through trial and error to give the best subjective fit of the theoretical spectra to the low-frequency region of the experimental spectra. Table 5 shows the values of A and h_c used to generate the plots for each fabric. The theoretical spectra are first plotted for each fabric covering the 3mm roughness for flow speeds from 20 to 60 m/s. These plots can be seen in Figure 3.35 through Figure 3.39. As can be seen in the figures, the experimental spectra follow the predicted (theoretical) spectra with relatively small error for low frequencies, but break away somewhere in the mid-frequency range.

As mentioned above, the fact that eddies of a certain size and smaller can exist beneath the canopy may explain this break frequency, which is defined here as the frequency at which the theoretical and experimental spectra diverge by more than 2 dB. Indeed, by considering the assumed convection velocity ($0.55U_m$) of the eddies within the flow, along with the break frequencies observed for each set of spectra, the length scales of the associated eddies can be calculated using equation 1.4. Fabrics 1, 2, 3 and 5 all display similar break frequencies as seen in Table 6, and the associated length scales are calculated and found to be approximately 1-2 mm smaller than the canopy height. This difference may be explained by the effect of viscosity very close to the wall and canopy in the region between these two planes. Viscous interactions with the wall and canopy may break down eddies which have length scales equal to the canopy height, while smaller eddies may pass through the space between the canopy and wall without interacting with either plane.

Table 6. Velocities, break frequencies, and calculated length scales for fabrics 1, 2, 3, and 5 shrouding 3mm hemispheres

$U_{jet}\left(\frac{m}{s}\right)$	$U_m\left(\frac{m}{s}\right)$	$U_c\left(\frac{m}{s}\right)$	$f_{break}\,(Hz)$	$L\,(mm)$
20	6.7	3.69	800	2.31
30	10.11	5.56	1100	2.53
40	13.62	7.49	1400	2.67
50	17.31	9.52	1800	2.64
60	20.84	11.46	2000	2.87

Additional discussion regarding fabric 4 is necessary to understand the attenuation factor given for this case. In Table 5, the value for h_c is given as 0.007 m (7 mm) which is well outside of the experimental uncertainty of measured canopy height. However, as can be seen in Figure 3.38, this attenuation factor gives an excellent fit for the spectra at low frequencies. The discrepancy is supposed to be due to the assumption of a constant value for max velocity in the boundary layer across all fabrics (constant U). For fabrics 1, 2, 3, and 5, which feature light, thin fibers, this assumption does not lead to significant errors as the max speed in the boundary layer likely remains largely unaffected by their presence. However, fabric 4 is much heavier, and can be supposed to have a larger influence on the boundary layer velocity, particularly in the region below the canopy where the pressure fluctuations are sensed.

For a more quantitative analysis, it is first assumed that the actual experimental canopy height is equal to 0.005 m, which is roughly equal to the height of the fabric supports plus the thickness of the fibers. To obtain the same attenuation factor as that previously calculated to yield Figure 3.38, the velocity parameter in the attenuation factor must also be decreased. This yields a velocity that is about 71% of the assumed velocity for the other fabrics. Using this new velocity and the break frequencies observed in Figure 3.38, the length scales of the eddies can be once again calculated, and are found to be within 0.5 mm of the values found for the other fabrics, as seen in Table 7.

Table 7. Velocities, break frequencies, and calculated length scales for fabric 4 shrouding 3mm hemispheres

$U_{jet}\left(\frac{m}{s}\right)$	$U_m\left(\frac{m}{s}\right)$	$U_c\left(\frac{m}{s}\right)$	$f_{break}\,(Hz)$	$L\,(mm)$
20	4.79	2.63	600	2.19
30	7.22	3.97	800	2.48
40	9.73	5.35	1100	2.43
50	12.36	6.80	1400	2.42
60	14.89	8.19	1600	2.56

It should be noted that the above discussions do not supersede or contradict the earlier discussions regarding the behavior of the fabric canopy in Section 3.6. In this case, we are using best-fit exponential lines to observe a break frequency, while saying nothing of the absolute levels of attenuation seen at different frequency ranges, as was discussed in Section 3.6. The consistency

of length-scales matching the canopy height simply supports the conclusion that the canopy suppresses the effect of eddies larger than the canopy height.

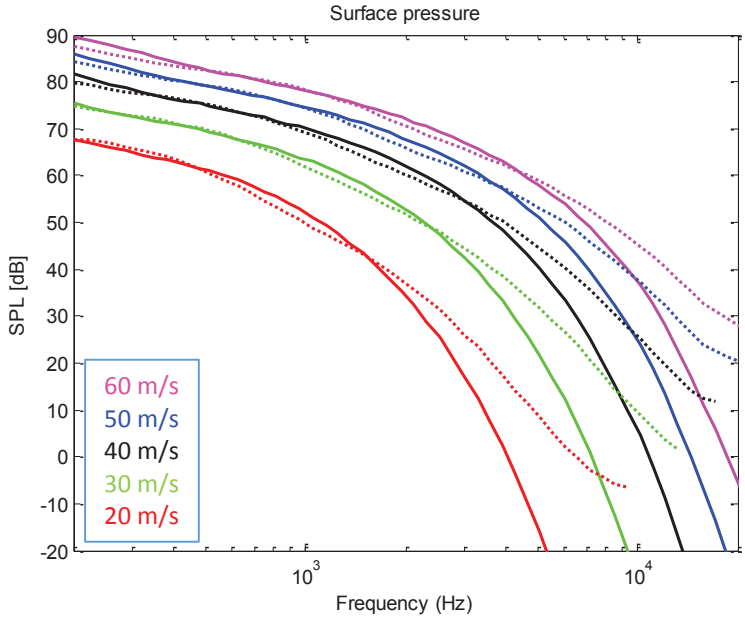

Figure 3.40. Comparison of theoretical (solid lines) and experimental (dotted lines) surface pressure spectra obtained for fabric 1 shrouding sandpaper

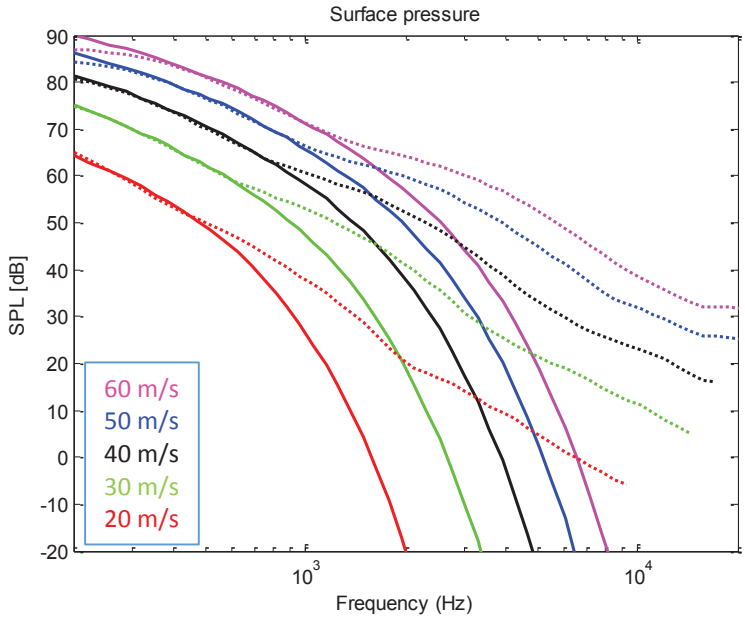

Figure 3.41. Comparison of theoretical (solid lines) and experimental (dotted lines) surface pressure spectra obtained for fabric 1 shrouding recessed needle bed

Considering the results obtained for other rough surfaces (sandpaper and recessed needle bed) by repeating the procedure described above, some final points remain to be made. Figure 3.40 and Figure 3.41 display the comparisons between the theoretical and experimental spectra for

fabric 1 covering the sandpaper and needle bed roughness. The figures show significant differences in the break frequencies, which are given numerically in Table 10 and Table 11 along with the calculated length scales. Recalling that the sandpaper roughness resulted in significant sag in the fabric canopies, the smaller length scales correspond to the smaller canopy height for this case. The recessed needle bed resulted in a canopy height of about 6 mm, and the larger length scales calculated here reflect this difference.

Table 8. Parameters used to generate exponential curve for each fabric covering sandpaper

$Fabric$	A	$h_c\ (m)$
1	2	0.001
2	2	0.002
3	2	0.0025
5	2	0.002

Table 9. Parameters used to generate exponential curve for each fabric covering the recessed needle bed

$Fabric$	A	$h_c\ (m)$
1	5	0.004
2	7	0.0055
3	20	0.008
5	8	0.005

Table 10. Velocities, break frequencies, and calculated length scales for fabric 1 shrouding sandpaper

$\boldsymbol{U_{jet}\left(\frac{m}{s}\right)}$	$\boldsymbol{U_m\ \left(\frac{m}{s}\right)}$	$\boldsymbol{U_c\left(\frac{m}{s}\right)}$	$\boldsymbol{f_{break}\ (Hz)}$	$\boldsymbol{L\ (mm)}$
20	6.7	3.69	1800	1.03
30	10.11	5.56	2300	1.21
40	13.62	7.49	3000	1.25
50	17.31	9.52	3600	1.32
60	20.84	11.46	4300	1.33

Table 11. Velocities, break frequencies, and calculated length scales for fabric 1 shrouding recessed needle bed

$\boldsymbol{U_{jet}\left(\frac{m}{s}\right)}$	$\boldsymbol{U_m\ \left(\frac{m}{s}\right)}$	$\boldsymbol{U_c\left(\frac{m}{s}\right)}$	$\boldsymbol{f_{break}\ (Hz)}$	$\boldsymbol{L\ (mm)}$
20	6.7	3.69	500	3.69
30	10.11	5.56	700	3.97
40	13.62	7.49	900	4.14
50	17.31	9.52	1100	4.33
60	20.84	11.46	1300	4.41

Collectively, these results point to two important general conclusions. First, canopy height does appear to be the correct scaling length for the exponential form of the attenuation, as the parameter h_c changes to reflect differences in canopy height for each of the rough surfaces, as seen in Table 5, Table 8, and Table 9. Second, turbulent eddies with smaller length scales than the canopy height can exist beneath the canopy, but their strength is reduced by the lack of larger eddies from which smaller eddies normally derive their energy (through the energy-cascade mechanism).

Table 12. Parameters used to generate exponential curve for each unidirectional canopy shrouding sandpaper

$Canopy$	A	$h_c\ (m)$
1	2	0.0016
2	1	0.001
3	1.3	0.0007

Finally, attention should be turned to the unidirectional canopies and their associated attenuation data. The characteristics of the attenuation are rather different from those seen in the fabric canopy experiment. Figure 3.42 shows the attenuation (theoretical and experimental) measured by microphone 2 under each unidirectional canopy, while Table 12 shows the values for A and h_c used for the theoretical attenuations for each canopy.

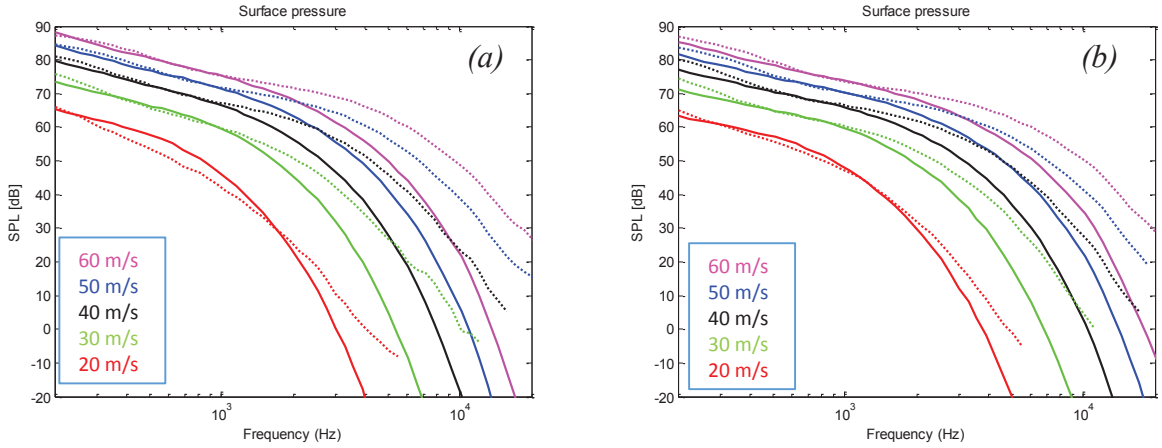

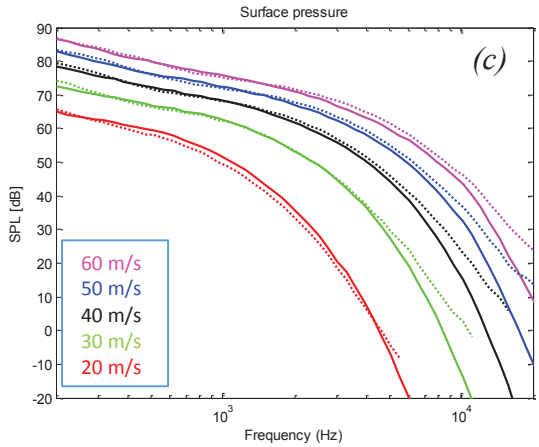

Figure 3.42. Comparison of theoretical (solid lines) and experimental (dotted lines) surface pressure spectra measured by microphone 2 under unidirectional canopy 1 (a), 2 (b), and 3 (c) shrouding sandpaper

The comparisons shown in Figure 3.42 demonstrate that the exponential form of the attenuation yields theoretical spectra which follow the experimental spectra to a certain degree dependent on the canopy being considered. The resulting spectra obtained for canopy 1 show a somewhat questionable fit, and matching the curve to the data from one speed (60 m/s in this case) seems to result in a poor fit for the other speeds. The quality of the fit increases for the other canopies, however, and it seems that the fit is universally good across all speeds and frequencies for canopy 3. However, when considering the values used to obtain these theoretical spectra, another problem is observed. The length scale (considered the canopy height for the fabric canopies) is extremely small for all cases, and actually decreases with increasing fiber diameter and length between fibers. Indeed, there were no length scales present in the experiment which decreased as the length scales used here. This leads to the conclusion that, in contrast to the fabric canopies, the theoretical spectra do not seem to be based on any easily observable physical dimensions or phenomena.

The above results point to an important difference between the fabric canopies and the unidirectional canopies, which is the presence and absence of cross-fibers, respectively. While the unidirectional canopy was designed to eliminate the cross-fibers and the corresponding high-frequency noise in the far-field, this also eliminated even more of the elements which contribute to the spectral short-cut mechanism at the heart of the surface pressure attenuation. Conceivably, the shear layer may be weakened significantly by the absence of cross-fibers. This limits the canopies' utility as a method for achieving significant surface pressure attenuations, especially at higher flow speeds, as seen here and in Section 3.10.

3.12 Surface Pressure Attenuation - Scaling

The next discussion of interest relates to scaling parameters which would result in a reasonable collapse of the surface pressure attenuation data. By investigating these parameters, additional insight can be gained relating to the specific mechanism by which the canopy suppresses pressure fluctuations at the surface.

As described in Section **Error! Reference source not found.** above, the break frequency associated with the comparison to an exponential decay of surface pressure fluctuations is directly related to canopy height. This demonstrates that the canopy height plays a direct role in the frequency dependence of the attenuation, and therefore is a good candidate for a scaling parameter

in the frequency domain. The influence of velocity is somewhat obvious, clearly shifting the spectra to higher frequencies for all cases. Therefore, the scaling to be investigated is the non-dimensional frequency scaling, defined here as fh_c/U_e, where f is frequency in Hz, h_c is the canopy height in meters, and U_e is the edge velocity in meters per second.

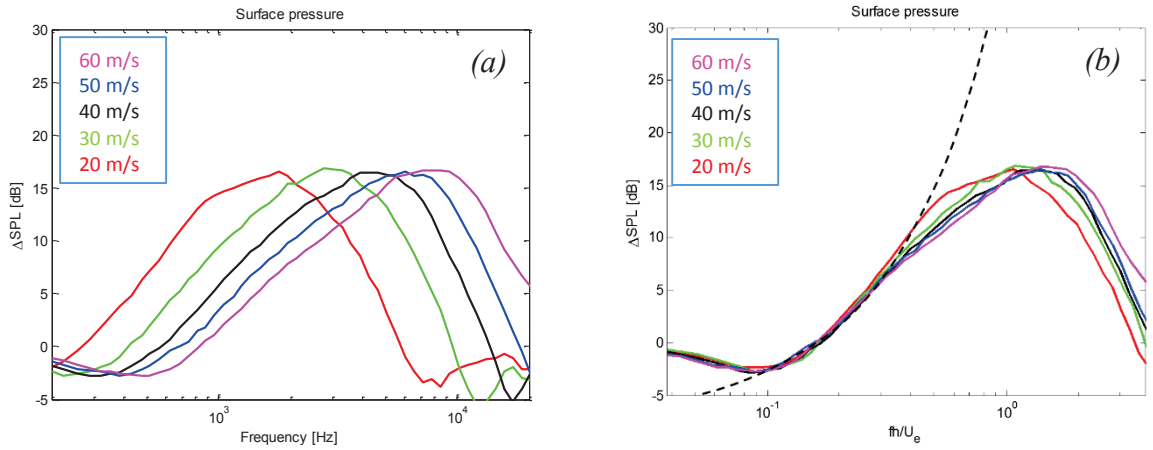

Figure 3.43. Unscaled (a) and scaled (b) surface pressure attenuations resulting from canopy 1 shrouding 3mm roughness

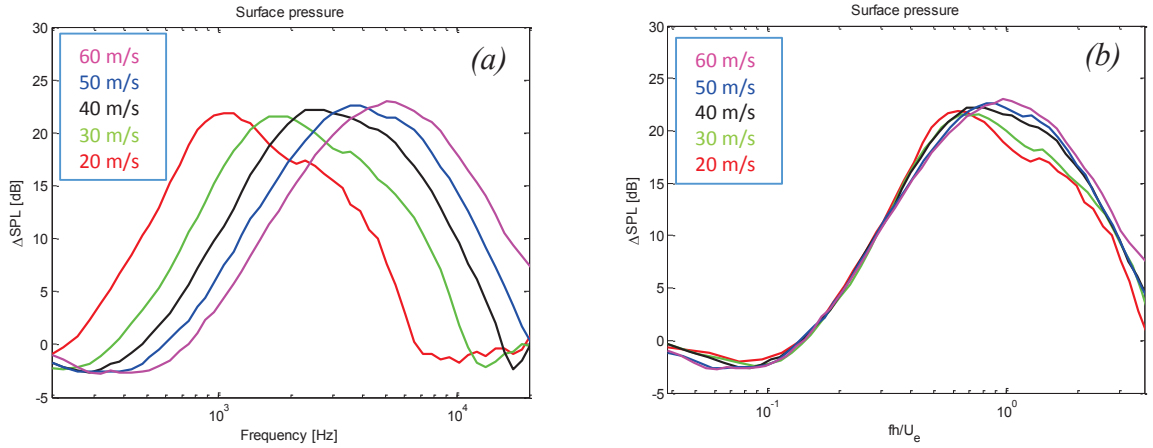

Figure 3.44. Unscaled (a) and scaled (b) surface pressure attenuations resulting from canopy 2 shrouding 3mm roughness

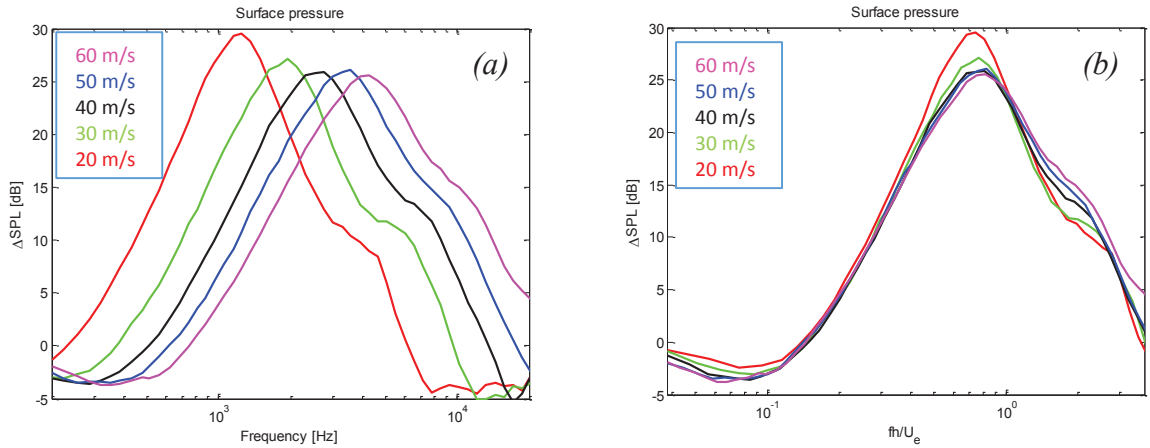

Figure 3.45. Unscaled (a) and scaled (b) surface pressure attenuations resulting from canopy 3 shrouding 3mm roughness

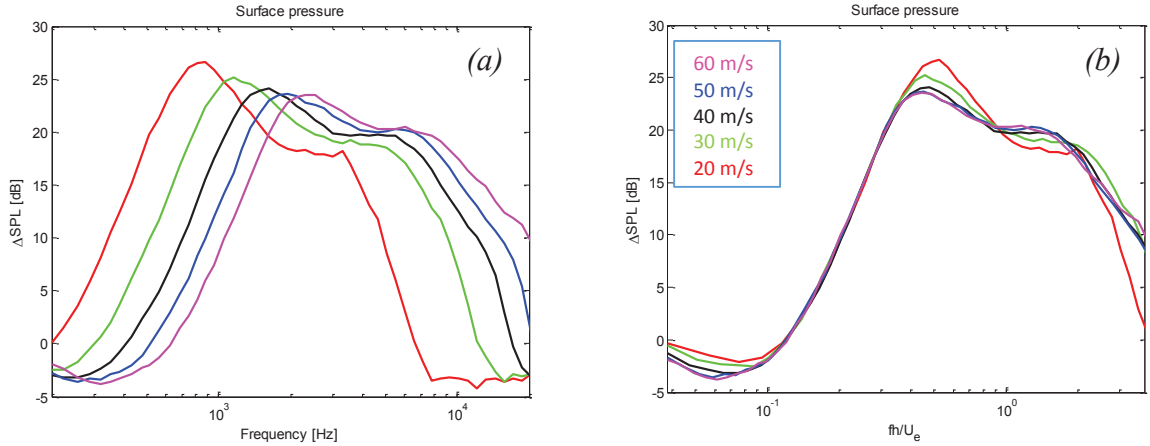

Figure 3.46. Unscaled (a) and scaled (b) surface pressure attenuations resulting from canopy 4 shrouding 3mm roughness

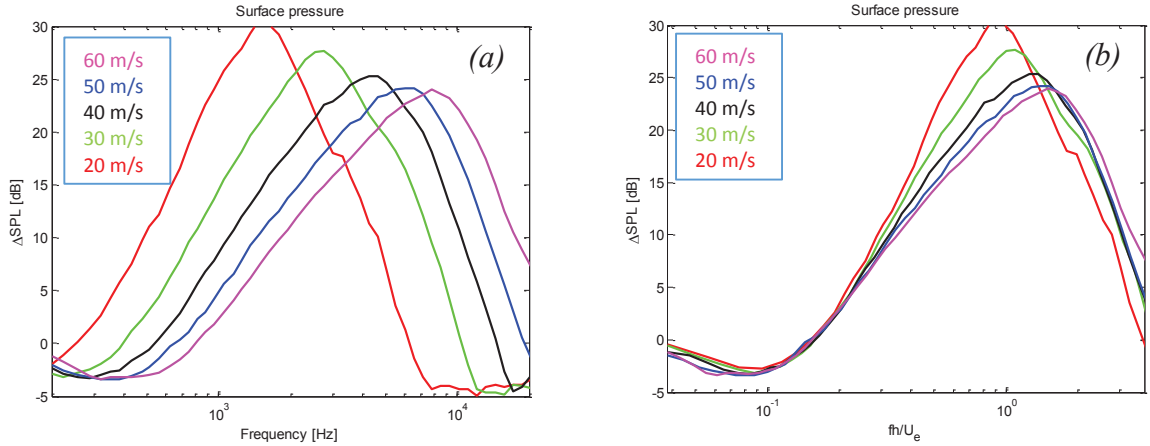

Figure 3.47. Unscaled (a) and scaled (b) surface pressure attenuations resulting from canopy 5 shrouding 3mm roughness

Figure 3.43 through Figure 3.47 show the unscaled attenuation (the difference in dB between the uncovered and covered spectra) of the surface pressure beneath each canopy shrouding 3mm roughness, along with the scaled attenuation using the frequency scaling discussed above. In this case, the parameter *h* was set to 0.004m. It may be noted that the discussion of the previous section may have some relevance here, as in some ways these scaled plots represent the attenuation factor used in that section. To illustrate this, Figure 3.43b features a dotted line which represents the exponential function used for the corresponding fabric and rough surface, and this line is seen to follow somewhat closely with the measured data, as one would expect given the previous discussion. However, the focus of this section lies more with the frequency scaling itself, which allows for a somewhat different perspective for analysis.

The proposed scaling results in a good collapse of the data across the entire frequency range for all fabrics, with the interesting exception of fabric 5, for which the collapse starts to break down in the upper half of the frequency spectrum. As seen in Figure 3.47b, as speed is increased, the attenuation at higher non-dimensional frequencies decreases. As described in Section 3.6, fabric 5 has very thin fibers which may not be effective at attenuating strong turbulent eddies in the flow. As speed increases, the turbulent eddies gain strength/energy. The result shown in Figure 3.47b may be the result of decreased effectiveness of the canopy as the turbulent eddies start to overpower the flimsy fibers comprising fabric 5 as speed is increased.

The results of scaling the attenuations due to fabrics shrouding the sandpaper are qualitatively the same as those discussed above and will not be shown here. However, the scaling of attenuations due to fabrics shrouding the recessed needle bed should be considered, as the trends seen for all fabrics bear resemblance to that shown by fabric 5 above 3mm hemispheres.

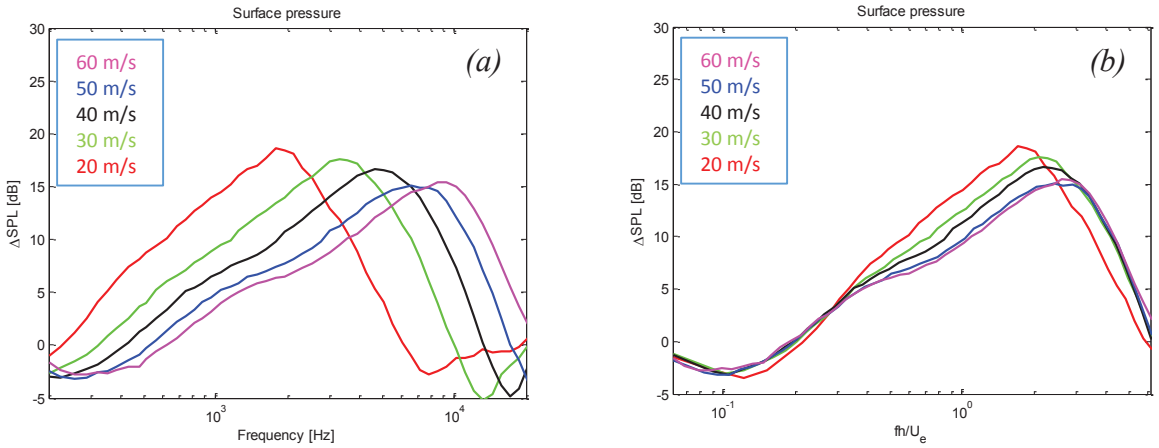

Figure 3.48. Unscaled (a) and scaled (b) surface pressure attenuations resulting from canopy 1 shrouding recessed needle bed

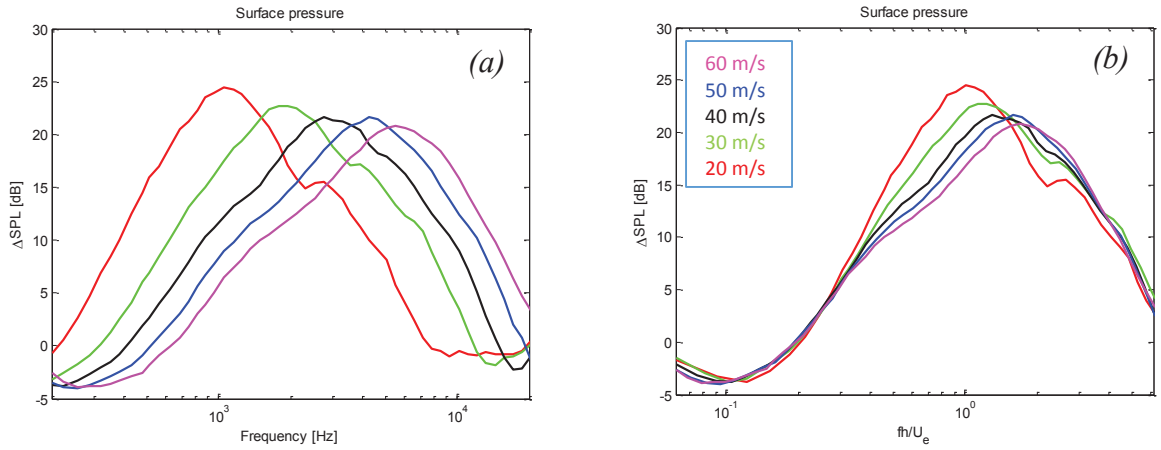

Figure 3.49. Unscaled (a) and scaled (b) surface pressure attenuations resulting from canopy 2 shrouding recessed needle bed

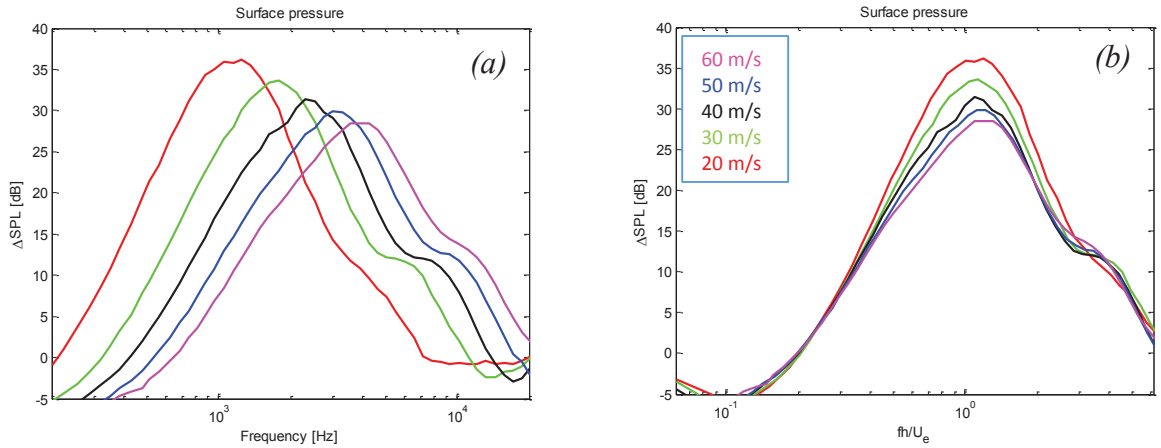

Figure 3.50. Unscaled (a) and scaled (b) surface pressure attenuations resulting from canopy 3 shrouding recessed needle bed

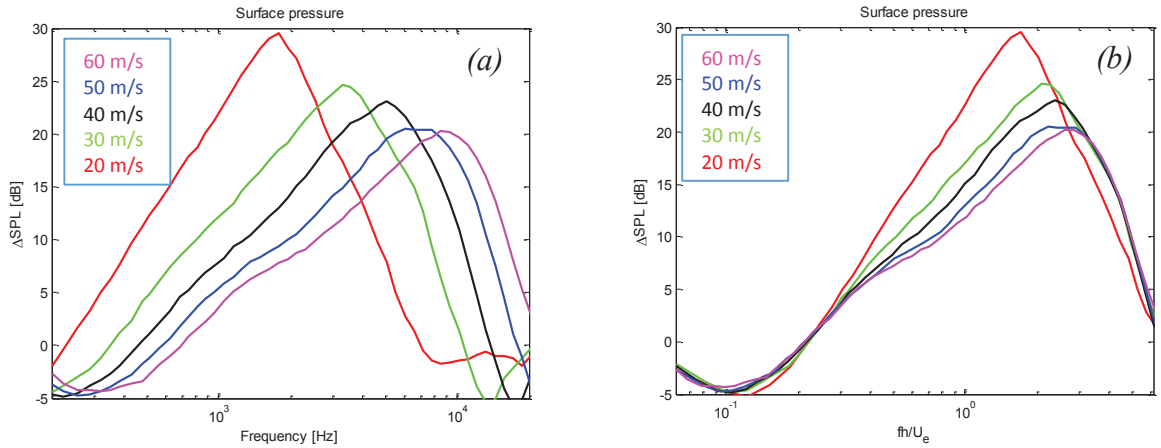

Figure 3.51. Unscaled (a) and scaled (b) surface pressure attenuations resulting from canopy 5 shrouding recessed needle bed

Figure 3.48 through Figure 3.51 show the unscaled attenuation in dB of the surface pressure beneath each canopy shrouding the recessed needle bed, along with the scaled attenuation using the frequency scaling discussed above. For this case, the value *h* was set to 0.0064m. These figures show that for all canopies, the performance begins to decay starting at the mid-frequency range, which is a similar phenomenon as that seen for fabric 5 above 3mm hemispheres. Indeed, the same explanation may be given here, as the increased canopy height places the canopy at a vertical location where the local speed is higher than for the other cases. This may result in the canopies' interaction with stronger vortices, leading to the overpowering of the canopy fibers.

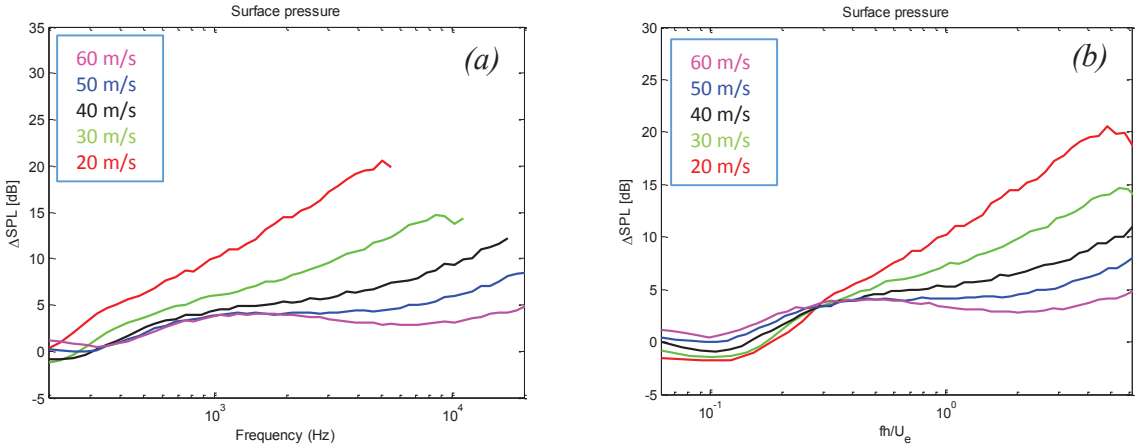

Figure 3.52. Unscaled (a) and scaled (b) surface pressure attenuation recorded by surface microphone 1 beneath unidirectional canopy 1.

The final dataset to be discussed here is the scaling of the surface pressure attenuation seen beneath the unidirectional canopies. An identical scaling scheme is used here as was used for the fabric canopies, and the differences in the results show a fundamental change in the mechanism by which the canopies lead to the attenuations. The attenuation seen by microphone 1 beneath canopy 1 is shown in Figure 3.52. The results show that the frequency scaling is ineffective in collapsing the curves, which is clearly caused by the differences in the levels of attenuation seen for all speeds. This result is representative of the other two canopies. Recalling that microphone 1 is the most upstream microphone beneath the canopy, it is feasible to assume that the flow is not fully developed at this streamwise location, particularly for higher speeds, so scaling will be difficult as the fundamental characteristics of the flow change as the speed is changed, which will lead to less attenuation for higher speeds. Interestingly, the spectra from the most downstream microphone seems to be less influenced by flow speed than the most upstream microphone.

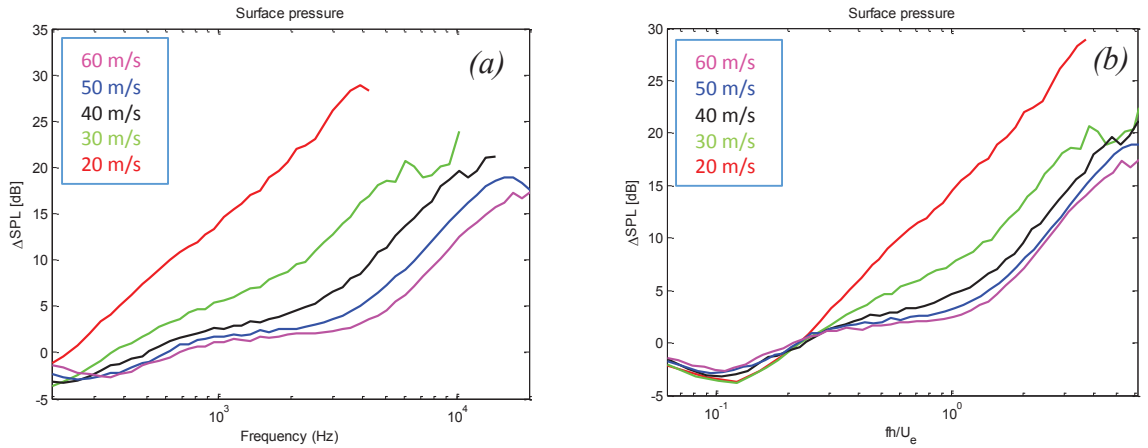

Figure 3.53. Unscaled (a) and scaled (b) surface pressure attenuation recorded by surface microphone 2 beneath unidirectional canopy 1.

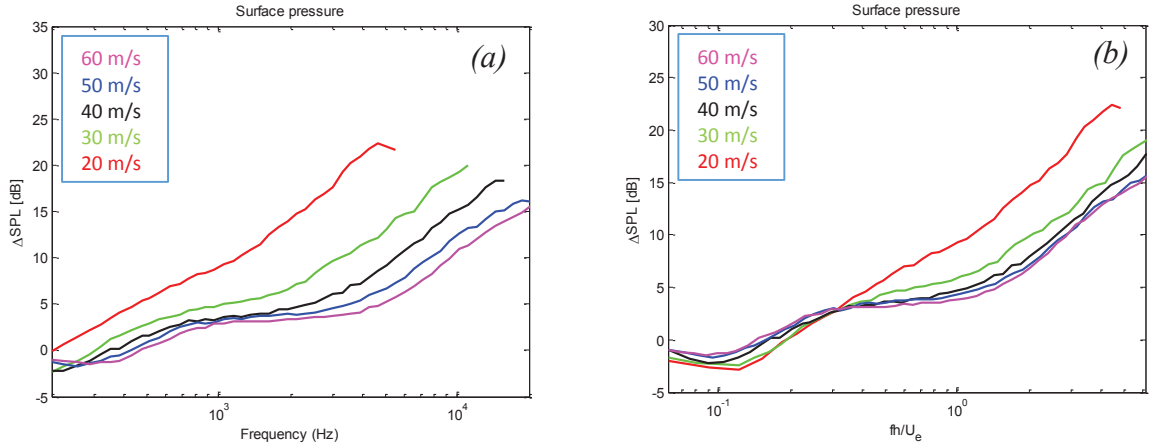

Figure 3.54. Unscaled (a) and scaled (b) surface pressure attenuation recorded by surface microphone 2 beneath unidirectional canopy 2.

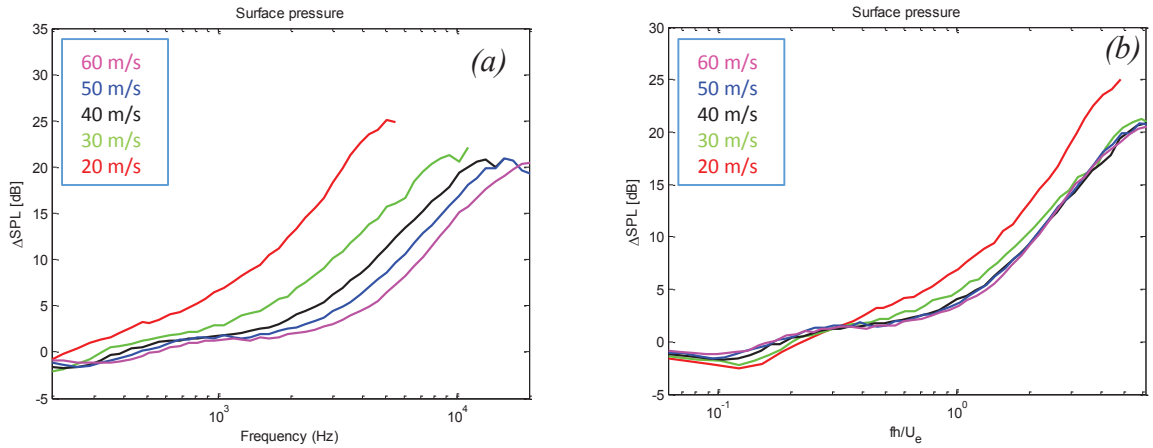

Figure 3.55. Unscaled (a) and scaled (b) surface pressure attenuation recorded by surface microphone 2 beneath unidirectional canopy 3.

Figure 3.53, Figure 3.54, and Figure 3.55 show the unscaled and scaled attenuations seen by microphone 2 beneath canopies 1, 2, and 3, respectively. Interestingly, the least collapse of the data is seen for canopy 1, while canopy 3 shows good collapse for most of the data. In all cases, the quality of the collapse improves for higher flow speeds, with the 20 m/s case being the most frequent outlier. It is possible that the wide spacing in the case of canopy 3 allows the flow to reach equilibrium more quickly than for the other canopies, which then results in roughly the same characteristics of the attenuation for all speeds. Figure 3.56, Figure 3.57, and Figure 3.58 show spectra obtained by microphone 3 beneath each canopy, and the same conclusions can be drawn from this data as well.

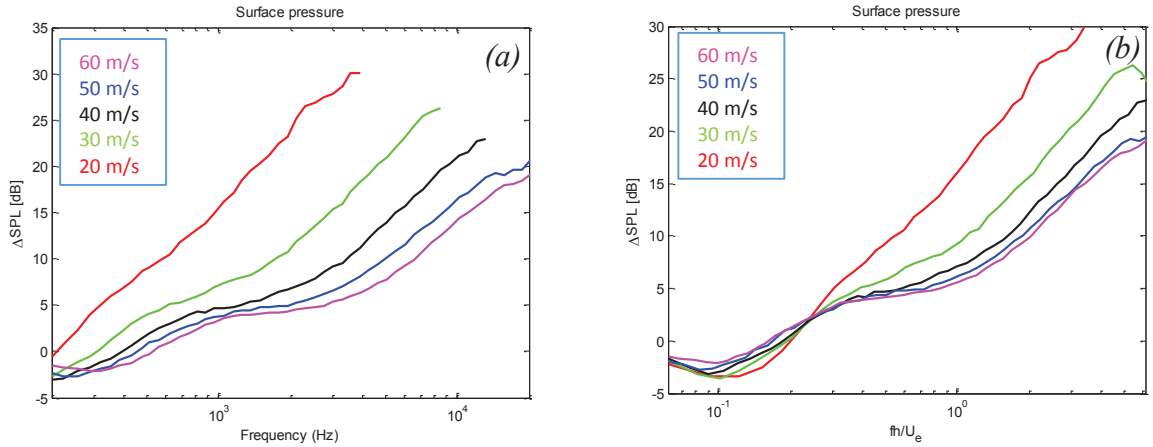

Figure 3.56. Unscaled (a) and scaled (b) surface pressure attenuation recorded by surface microphone 3 beneath unidirectional canopy 1.

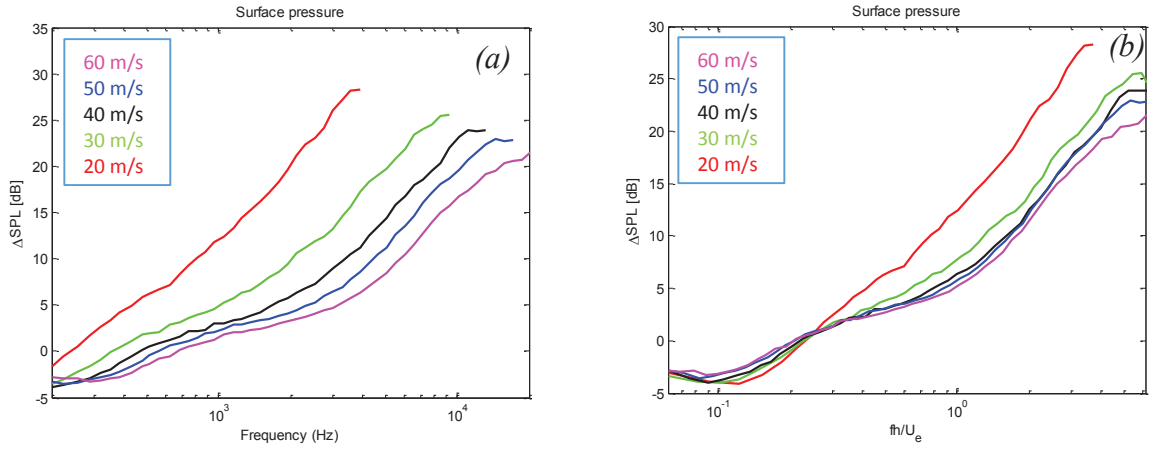

Figure 3.57. Unscaled (a) and scaled (b) surface pressure attenuation recorded by surface microphone 3 beneath unidirectional canopy 2.

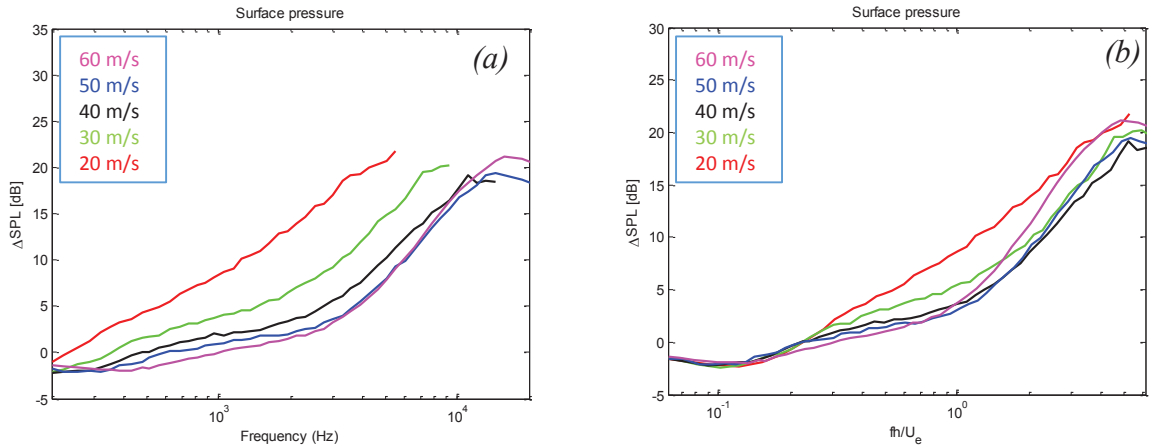

Figure 3.58. Unscaled (a) and scaled (b) surface pressure attenuation recorded by surface microphone 3 beneath unidirectional canopy 3.

Chapter 4 – Conclusions and Future Work

The wings of most species of owl have been shown to possess three unique physical attributes which allow them to hunt in effective silence: a comb of evenly-spaced bristles along the wing leading-edge; a compliant and porous fringe of feathers at the trailing-edge; and a velvety down material distributed over the upper wing surface. This investigation has focused on the last of the mechanisms. A microscopic study of several owl feathers revealed the structure of the velvety down to be very similar to that of a forest or a field of crops. The individual hairs which comprise the surface rise from the surface and then bend in the flow direction, forming a sort of canopy with an open area percentage of approximately 70%. Analogous surface treatments (suspended canopies) were chosen or designed which simulated the most essential geometric features of the velvety down material, and the effects of the experimental materials were examined with regard to the noise produced by flow over rough surfaces.

Experiments were performed in the Virginia Tech Anechoic Wall Jet Wind Tunnel to examine the aeroacoustic effects of large open area percentage canopies suspended above rough surfaces. Measurements of far-field sound radiated from the test surfaces and surface pressure fluctuations beneath the canopies were taken. The overall results are summarized here:

- All canopies were found to dramatically reduce pressure fluctuations on the underlying surface by up to 30 dB.
- Both fabric and unidirectional canopies were found to reduce noise due to flows over surface roughness through a range of frequencies.
- While fabric canopies can produce their own sound, particularly at high frequencies, the reduction in surface pressure fluctuations can reduce roughness noise at lower frequencies.
- The use of a canopy with fibers oriented only in the flow direction does not produce the high-frequency self-noise of the fabric canopies, but surface pressure fluctuations are still suppressed and roughness noise is reduced typically by 5-8 dB over a broad range of frequencies.

In addition to these overall results, detailed analysis comparing the specific form of the surface pressure attenuation with each geometric parameter of the fabric revealed a significant correlation between them. Fiber spacing will determine the high frequency component of the attenuation by controlling the size of turbulent eddies which can pass through the fabric unhindered. Fiber diameter will determine the mid-frequency component of attenuation by dampening some of the higher-energy turbulent structures.

Through comparison with forest canopy theory, an exponential attenuation factor was shown to predict, at some frequencies, the general form of the surface pressure spectra in the presence of a canopy. Canopy height was shown to play a role in determining the length scales of turbulent eddies which exist between the canopy and the underlying surface. Through scaling the surface pressure spectra on non-dimensional frequency, the fabric canopies were shown to act as a sort of spatial filter, which decreases the influence of turbulent eddies on the surface pressure fluctuations in a way that is based almost solely on the length scales of the eddies. A streamwise development of surface pressure attenuation beneath the unidirectional canopy was observed and was theorized to be caused by a sort of viscous mechanism acting as the flow moved downstream.

From the conclusions stated above, along with the more detailed analysis of Chapter 3, the usefulness of canopies shrouding surface roughness with regard to aeroacoustics becomes

apparent. The overall results of the current investigation open the door to a wide range of new research and development opportunities with regard to the optimization and customization of the types of surfaces seen here for application onto engineering structures. The various surfaces tested here, along with the analysis of the effects of those surfaces, should give the reader a basic understanding of the effects of different canopy parameters on the acoustic behavior of the system to which it is applied. However, despite the completion of the present work, many questions regarding the exact influence of the canopies on the surrounding flow remain unanswered. These questions include, but are not limited to, the following:

- How does the canopy influence the vertical velocity (boundary layer) profile below and above the canopy?
- How does the canopy effect turbulence levels in the region of interest?
- Does the canopy result in a decorrelation of the turbulent structures below the canopy?
- How does the canopy influence the convection velocity of the turbulent eddies within the flow?

In addition to these questions, the effect of canopy height is still largely unknown. The sag present in the fabric canopy experiment, while allowing for some data analysis, was not sufficiently quantified or controlled to provide strong support for any conclusions. In light of these questions, the author proposes the following experiments:

- Velocity profile measurements should be performed using (at a minimum) a hot-wire anemometer to obtain both velocity and turbulence level data in the region of the canopy. These measurements could be supplemented by oil flow visualizations to show overall flow features.
- A similar experiment to that described in this paper could be performed featuring more surface pressure microphones, spaced more closely together, to measure the convection velocity and potential decorrelation of turbulent structures.
- Further experimentation with canopy height, and other fabric parameters, would allow for a more accurate theory regarding the effect of fabric geometry.

These experiments would lead to much greater understanding of the various effects of canopy flows, and would simplify any customization or optimization that would expedite the application of this technology to engineering structures.

References

Alexander, W. N. (2011). Sound from Rough Wall Boundary Layers. ", Ph.D. dissertation, Virginia Polytechnic Institute and State University, 2001. avail: http://scholar.lib.vt.edu/theses/available/etd-10112011-085924/

Alexander, W. N., Devenport, W. J., & Glegg, S. A. L. (2012). Predictions of Sound from Rough Wall Boundary Layers. *AIAA Journal, 51*(2), 465-475. doi: 10.2514/1.j051840

Anderson, J., Stewart, D., Goody, M., & Zoccola, P. (2007). Sound from flow over a rough surface. *Proceedings of the ASME International Mechanical Engineering Congress and Exposition, 1*, 87-100.104.

Awasthi, M., Bryan, B., Devenport, W., & Glegg, S. (2013). Sound Radiation from Rounded Steps and Gaps. 19th AIAA/CEAS Aeroacoustics Conference, Berlin, 27-29 May. AIAA 2013-2048. doi: 10.2514/6.2013-2048

Blake, W. K. (1970). Turbulent boundary-layer wall-pressure fluctuations on smooth and rough walls. *Journal of Fluid Mechanics, 44*(4), 637-660.

Blake, W. K. (1986). Mechanics of Flow Induced Sound and Vibration, Academic Press, New York.

Chanaud, R. C. (1969). Experimental study of aerodynamic sound from a rotating disk. *The Journal of the Acoustical Society of America, 45*, 392-397.

Chase, D. M. (1987). The Character of the Turbulent Wall Pressure Specturm at Subconvective Wavenumbers and a Suggested Comprehensive Model. *Journal of Sound and Vibration, 112*, 125-147.

Clark, I., Devenport, W. J., Jaworski, J., Daly, C., Peake, N., & Glegg, S. A. (2014). The Noise Generating and Suppressing Characteristics of Bio-Inspired Rough Surfaces. 20th AIAA/CEAS Aeroacoustics Conference, Atlanta GA, June 16-20, 2014, AIAA-2014-2911.

Cole, L. D. (1980). Measurements of Sound Generated by Boundary Layer Turbulence over Smooth and Rough Surfaces: DTNSRDC.

Corcos, G. M. (1964). The Structure of the Turbulent Pressure Field in Boundary-Layer Flows, *Journal of Fluid Mechanics, 18*(3), 353-378.

Devenport, W., Wahl, E. A., Glegg, S. A. L., Nathan Alexander, W., & Grissom, D. L. (2010). Measuring surface pressure with far field acoustics. *Journal of Sound and Vibration, 329*(19), 3958-3971. doi: 10.1016/j.jsv.2010.03.012

Devenport, W. J., Grissom, D. L., Nathan Alexander, W., Smith, B. S., & Glegg, S. A. L. (2011). Measurements of roughness noise. *Journal of Sound and Vibration, 330*(17), 4250-4273. doi: 10.1016/j.jsv.2011.03.017

Farabee, T. M., & Geib, F. E. (1991). Measurements of Boundary Layer Pressure Fluctuations at Low Wavenumbers on Smooth and Rough Walls. *Flow Noise Modeling Measurements and Control, ASME NCA, 11*, 55-68.

Finnigan, J. (2000). Turbulence in Plant Canopies. *Annu. Rev. Fluid Mech., 32*, 519-571.

Glegg, S., & Devenport, W. (2009). The far-field sound from rough-wall boundary layers. *Proceedings of the Royal Society A: Mathematical, Physical and Engineering Sciences, 465*(2106), 1717-1734. doi: 10.1098/rspa.2008.0318

Glegg, S., Devenport, W., Grissom, D., & Smith, B. (2007). Rough Wall Boundary Layer Noise: Theoretical Predictions, 13th AIAA/CEAS Aeroacoustics Conference, Rome, Italy, May 21-23, 2007, AIAA-2007-3417. doi: 10.2514/6.2007-3417

Goldstein, M. (1976). Aeroacoustics. New York, NY: McGraw Hill.
Graham, R. R. (1934). The silent flight of owls. *The Journal of the Royal Aeronautical Society, 38*, 837-843.
Grissom, D., Smith, B., Devenport, W., & Glegg, S. (2007). Rough-Wall Boundary Layer Noise: An Experimental Investigation, 13th AIAA/CEAS Aeroacoustics Conference, Rome, Italy, May 21-23, 2007, AIAA-2007-3418. doi: 10.2514/6.2007-3418
Grissom, D., Smith, B. S., Devenport, W., & Glegg, S. (2006). Rough Wall Boundary Layer Noise, 12th AIAA/CEAS Aeroacoustics Conference, Cambridge, Massachusetts, May 8-10, 2006, AIAA-2006-2409.
Hersh, A. (1983). Experimental investigation of surface roughness generated flow noise. AIAA Paper, doi: 10.2514/6.1983-786
Howe, M. S. (1984). On the Generation of Sound by Turbulent Boundary Layer Flow Over a Rough Wall. *Proceedings of the Royal Society A: Mathematical, Physical and Engineering Sciences, 395*(1809), 247-263. doi: 10.1098/rspa.1984.0100
Howe, M. S. (1986). The Influence of Viscous Surface Stress on the Production of Sound by Turbulent Boundary Layer Flow over a Rough Wall. *Journal of Sound and Vibration, 104*, 29-39.
Howe, M. S. (1988). The Turbulent Boundary-Layer Rough-Wall Pressure Spectrum at Acoustic and Subconvective Wavenumbers. *Proceedings of the Royal Society A: Mathematical, Physical and Engineering Sciences, 415*(1848), 141-161.
Klän, S., Bachmann, T., Klaas, M., Wagner, H., & Schröder, W. (2009). Experimental analysis of the flow field over a novel owl based airfoil. *Experiments in Fluids, 46*(5), 975-989. doi: 10.1007/s00348-008-0600-7
Klän, S., Burgmann, S., Bachmann, T., Klaas, M., Wagner, H., & Schröder, W. (2012). Surface structure and dimensional effects on the aerodynamics of an owl-based wing model. *European Journal of Mechanics - B/Fluids, 33*, 58-73. doi: 10.1016/j.euromechflu.2011.12.006
Kroeger, R. A., Grushka, H. D., & Helvey, T. C. (1972). Low Speed Aerodynamics for Ultra-Quiet Flight, Tennessee University Space Institute Tullahoma.
Lilley, G. (1998). A study of the silent flight of the owl. AIAA Paper 2340 doi: 10.2514/6.1998-2340
Liu, Y., & Dowling, A. P. (2007). Assessment of the Contribution of Surface Roughness to Airframe Noise. *AIAA Journal, 45*(4), 855-869. doi: 10.2514/1.25217
Raupach, M. R., & Thom, A. S. (1981). Turbulence In and Above Plant Canopies. *Annu. Rev. Fluid Mech., 13*, 97-129.
Skudrzyk, E. J., & Haddle, G. P. (1960). Noise production in a turbulent boundary layer by smooth and rough surfaces. *Journal of the Acoustical Society of America, 32*, 19-34.
Smol'yakov, A. V. (2001). Noise of turbulent boundary layer flow over smooth and rough plates at low Mach number. *Acoustical Physics, 47*, 218-225.
Thorpe, W. H., & Griffin, D. R. (1962). The Lack of Ultrasonic Components in the Flight Noise of Owls Compared with Other Birds. *IBIS, 104*(2), 256-257.
Wygnanski, I., Katz, Y., & Horev, E. (1992). On the applicability of various scaling laws to the turbulent wall jet. *Journal of Fluid Mechanics, 234*, 660-690.